UNIVERSITY OF CALIFORNIA SAN DIEGO

Adaptations of the gastrointestinal tract to chronic viral infection

A dissertation submitted in partial satisfaction of the
requirements for the degree Doctor of Philosophy

in

Biology

by

Lara Labarta Bajo

Committee in charge:

Professor Elina Zuniga, Chair
Professor Janelle S Ayres
Professor John Chang
Professor Stephen M Hedrick
Professor Ye Zheng

2020

The Dissertation of Lara Labarta Bajo is approved, and it is acceptable in quality and form for publication on microfilm and electronically:

_____

_____

_____

_____

_____
Chair

University of California San Diego

2020

DEDICATION

Al Miguel, el meu company de viatge. Pel seu suport incondicional.

EPIGRAPH

Caminante, son tus huellas
el camino y nada más;
caminante, no hay camino,
se hace camino al andar.

Al andar se hace camino
y al volver la vista atrás
se ve la senda que nunca
se ha de volver a pisar.

Caminante no hay camino
sino estelas en la mar…

Hace algún tiempo en ese lugar
donde hoy los bosques se visten de espinos
se oyó la voz de un poeta gritar
"Caminante no hay camino,
Se hace camino al andar…"

Golpe a golpe, verso a verso…

-- Antonio Machado, "Cantares"

TABLE OF CONTENTS

LIST OF FIGURES

LIST OF SUPPLEMENTAL FILES

Chapter1_supplementary_Datasets.xls

Chapter2_supplementary_Datasets.xls

ACKNOWLEDGEMENTS

I would like to thank my mentor, Dr Elina Zúñiga, for sharing her unwavering excitement for science with me, for constantly supporting my professional growth throughout this journey as well as for her role as the chair of my committee. I would like to sincerely thank all of my committee members, whose feedback has been very impactful for my professional development.

I would also like to acknowledge the Zuniga lab members, both past and current, whose support has been instrumental for the completion of this dissertation. Lastly, I would also like to extend this acknowledgement to the immunology group at UCSD, whose members provided me with invaluable feedback on my projects and willingly shared many resources with me.

Chapter 1, in full, will be submitted for publication as it appears. Lara Labarta-Bajo was the primary investigator and author of this paper. I would like to thank co-authors Dr. Steven P. Nilsen, Dr. Gregory Humphrey, Dr. Tara Schwartz, Dr. Karenina Sanders, Dr. Austin Swafford, Dr. Rob Knight, Dr. Jerrold R. Turner and Dr. Elina I. Zúñiga for their contributions.

Chapter 2, in full, will be submitted for publication as it appears. Lara Labarta-Bajo was the primary investigator and author of this paper. I would like to thank co-authors Anna Gramalla-Schmitz, Dr. Romana R. Gerner, Katelynn R. Kazane, Dr. Gregory Humphrey, Dr. Tara Schwartz, Dr. Karenina Sanders, Dr. Austin Swafford, Dr. Rob Knight, Dr. Manuela Raffatellu and Dr. Elina I. Zúñiga for their contributions.

I would also like to acknowledge Dr. Pieter Dorrestein and his team, Dr. Clarisse A. Marotz, Dr. Pedro Belda-Ferre, Dr. Gail Ackermann as well as the personnel at the UCSD BSB and PCH Animal Facilities, IGM Genomics center sequencing core, Moore's Cancer Center Histopathology core and at the UCSD Microscopy core for enabling the creation of both manuscripts.

VITA

2012 Bachelor of Science in Biotechnology, Universitat de Barcelona, Spain

2013 Master in Biomedical Research, Universitat Pompeu Fabra, Barcelona, Spain

2020 Doctor of Philosophy, University of California San Diego

PUBLICATIONS

Labarta-Bajo L, Gramalla-Schmitz A, Gerner RR, Humphrey G, Schwartz T, Sanders K, Swafford A, Knight R, Raffatellu M, Zuniga, EI. "CD8 T cells drive anorexia, dysbiosis and blooms of a commensal with immunosuppressive potential after viral infection". In revision. (2020)

Labarta-Bajo L, Nilsen SP, Humphrey G, Schwartz T, Sanders K, Swafford A, Knight R, Turner JR, Zuniga EI. "IFN-I and CD8 T cells increase intestinal barrier permeability after chronic viral infection". In revision. (2020).

Dolina JS, Lee J, Griswold RQ, **Labarta-Bajo L**, Kannan S, Greenbaum JA, Bahia El Idrissi N, Pong MJ, Croft M, Schoenberger SP. "TLR9 Sensing of Self-DNA Controls Cell-Mediated Immunity to Listeria Infection via Rapid Conversion of Conventional CD4+ T Cells to Treg". Cell Reports (accepted) (2020).

Tsitsiklis A, Bangs DJ, Lutes LK, Chan S-W, Geiger K, Modzelewski AJ, **Labarta-Bajo L**, Zuniga EI, Robey EA. "An unusual MHC molecule generates protective CD8+ T cell responses to chronic infection". Frontiers in Immunology. https://doi.org/10.3389/fimmu.2020.01464 (2020).

Wang M, Jarmusch AK, Vargas F, Aksenov AK, Gauglitz JM, Weldon K, Petras D, da Silva R, Quinn R, Melnik AV, van der Hooft JJ, Rodriguez AMC, Nothias LF, Aceves CM, Panitchpakdi M, Brown E, Di Ottavio F, Sikora N, Elijah EO, **Labarta-Bajo L**, Gentry EC, Shalapour S, Kyle KE, Puckett SP, Watrous JD, Carpenter CS, Bouslimani A, Ernst M, Swafford AD, Zuniga EI, Balunas MJ, Klassen JL, Loomba R, Knight R, Bandeira N, Dorrestein PC. "Mass spectrometry searches using MASST". Nature Biotechnology 38, 23-26. 10.1038/s41587-019-0375-9 (2020)

Greene TT, **Labarta-Bajo L**, Zuniga EI. "Dangerously Fit: Extracellular ATP Aids Memory T Cell Metabolism". Volume 49, Issue 2, P208-210. Immunity. 10.1016/j.immuni.2018.08.009 (2018)

Lewis GM, Wehrens EJ, **Labarta-Bajo L**.& Zuniga EI. "TGF-beta Receptor Maintains CD4 T cell Identity during Chronic Viral Infections". Journal of Clinical Investigations. 126(10):3799-3813. https://doi.org/10.1172/JCI87041 (2016).

ABSTRACT OF THE DISSERTATION

Adaptations of the gastrointestinal tract to chronic viral infection

by

Lara Labarta Bajo

Doctor of Philosophy in Biology

University of California San Diego, 2020

Professor Elina Zuniga, Chair

Viral infections elicit host adaptations that can enable host-pathogen equilibrium. Here, we investigated adaptations of the gastrointestinal tract elicited by a persistent virus, their underlying mechanisms and their implications for the infected host. By using murine infection with lymphocytic choriomeningitis virus (LCMV) we demonstrated that infection with a persistent viral isolate led to long-term viral replication in hematopoietic and mesenchymal, but not epithelial cells (IEC) in the intestine. Viral persistence drove sustained intestinal epithelial barrier leakage, which was characterized by increased paracellular flux of small molecules and was associated with enhanced colitis susceptibility. IFN-I signaling caused tight junction dysregulation in IEC, promoted gut microbiome shifts and enhanced intestinal CD8 T cell responses. Notably, both IFN-I receptor blockade and CD8 T cell depletion prevented infection-induced barrier leakage. Our results demonstrated that infection with a virus that persistently replicated in intestinal mucosa

increased epithelial barrier permeability and revealed IFN-I and CD8 T cells as causative factors of intestinal leakage during chronic infections. We further discovered that mouse infection with the fast-spreading and persistent (but not the slow-spreading acute) isolate of LCMV induced large-scale microbiome shifts characterized by increased Verrucomicrobia and reduced Firmicute/Bacteroidetes ratio. Remarkably, the most profound microbiome changes occurred transiently after infection with the fast-spreading persistent isolate, were uncoupled from sustained viral loads and were instead largely caused by CD8 T cell responses and/or CD8-T-cell-induced anorexia. Among the taxa enriched by infection with the fast-spreading virus, *Akkermansia muciniphila*, broadly regarded as a beneficial commensal, bloomed upon starvation and in a CD8-T-cell-dependent manner. Strikingly, oral administration of *Akkermansia muciniphila* suppressed selected effector features of CD8 T cells in the context of both infections. Our findings define unique microbiome differences after chronic versus acute viral infections and identify CD8 T cell responses and downstream anorexia as driver mechanisms of microbial dysbiosis after infection with a fast-spreading virus. Our data also highlight potential context-dependent effects of probiotics and suggest a model in which changes in host behavior and downstream microbiome dysbiosis may constitute a previously unrecognized negative feedback loop that contributes to CD8 T cell adaptations after infections with fast-spreading and/or persistent pathogens.

Introduction

Pathogenic chronic infections constitute a global health burden

Human chronic viral infections are highly prevalent in the human population, with each one of us harboring an estimated average of 8-12 chronic viruses at a given time(1). It is indeed very hard to identify strict 'uninfected' individuals, as most chronic viral infections we are exposed to do not cause any perceptible symptoms. Such evidence has led to the proposition that these viruses, which includes Adeno-associated as well as several Herpesviruses among others, are actually part of our normal metagenome, and given that these rarely cause disease in immunocompetent individuals, we currently possess little knowledge about their biology. Instead, humanity has extensively focused research efforts on understanding the complex biology of viruses such as Hepatitis C virus (HCV), Hepatitis B virus (HBV) and Human Immunodeficiency Virus (HIV), among others, which cause remarkable health burden. In that regard, the World Health Organization (WHO) estimated that 257 million individuals were living with chronic HBV infection as of 2015(2), 71 million were afflicted with HCV as of 2016(3) and 37.9 million were living with HIV as of 2018(4).

The lymphocytic choriomeningitis virus experimental mouse model

Chronic infections, including those caused by viruses such as HCV and HIV, bacterial infection with *Mycobacterium tuberculosis* or with the protozoa *Plasmodium falciparum* are characterized by host adaptations that jointly facilitate long-term co-existence with the persistent pathogen. Such adaptations generally involve the suppression of the ensuing immune response (1, 5, 6). Given the cellular and anatomical complexity of an immune response, the establishment of small animal models of chronic infection is key to study immune-pathogen interactions *in vivo*. In

addition, given the specificity of viruses for their target species, it is ideal to study immune responses in natural and immunocompetent hosts.

Rodents have been identified as principal hosts of RNA viruses belonging to the *Arenaviridae* family, which includes an estimated total of 31 viral species(7) including Lassa, Junin or Machupo that can be transmitted to humans, where they cause severe (and often lethal) hemorrhagic fever. These viruses are endemic in western Africa as well as in several South American regions(7). Lymphocytic choriomeningitis virus (LCMV) is, however, the only arenavirus known to be distributed worldwide, which is attributed to its ability to infect the ubiquitous species *Mus musculus*, its natural host and reservoir, where it vertically transmits from generation to generation(8). LCMV is a non-cytolytic, enveloped virus that contains a negatively stranded RNA genome that is split into two 'L' and 'S' segments(9, 10). The polymerase and a small RING finger protein Z are encoded in the 'L' segment(10, 11), whereas the viral nucleoprotein (NP) and the glycoprotein (GP) are both encoded in the 'S' segment(9). Importantly, GP undergoes post-translational cleavage into mature virion proteins GP1 and GP2(12), which are both present on the viral envelope, and of which GP1 is the determinant for viral tropism(13). Two main isolates are routinely used in the laboratory, the parental strain LCMV Armstrong 53b (ARM) and its derived variant clone 13 (Cl13) isolate(14, 15). Infection of WT C57BL/6 adult mice with ARM induces an acute infection that is cleared within 7-10 days(16). In contrast, high-titer intravenous infection allows the Cl13 isolate to establish long-term persistence in the serum, spleen, lymph nodes, lung and liver (i.e. 60-90 days)(16, 17), in the brain (~200-300 days)(8) and life-long persistence in the kidneys(18) of infected mice. One big advantage of the LCMV model is that both ARM and Cl13 isolates trigger T cell responses to shared epitopes, which allows side-

by-side comparisons of T cell responses generated in the context of acute vs. chronic challenge(16).

Immune adaptations ensure host-pathogen equilibrium during chronic infections

Chronic infections, including those caused by human immunodeficiency virus (HIV), *Mycobacterium tuberculosis*, *Plasmodium* species and mouse infection with LCMV induce host adaptations that can facilitate long-term co-existence with the persistent pathogen(1, 5, 6). In this context, the best-studied host adaptations are the reprogramming of innate and adaptive immune cells that attenuate selected cellular functions while often remaining partially effective at maintaining some degree of pathogen control. Given that continuous pathogen replication or latency are often tolerated but an unrestrained immune response most often results in host death, organisms have evolved sophisticated and redundant mechanisms to avoid the latter even at risk of the former. Indeed, immune cell adaptations involve multiple layers of cell-intrinsic transcriptional, epigenetic, post-transcriptional and metabolic regulation(1, 6). These adaptations represent a response to cell-extrinsic changes, including continuous stimulation via antigen or pathogen recognition receptors, an inflammatory milieu, and altered nutrient and oxygen levels (1, 6). Notably, immune cell adaptations appear to be conserved during chronic infections with distinct pathogens, as well as in other settings of chronic immune stimulation such as cancer, in a range of host species(19). Lastly, a hypo-functional or exhausted state of Type I Interferon producing cells was also described in chronically-infected mice and in multiple other murine and human settings of chronic immune stimulation(6, 20), although its implications for host-pathogen equilibrium have not been elucidated yet.

CD8 T cell adaptations during chronic viral infection

One of the most extensively studied examples of immune adaptation to the presence of a chronic pathogen occurs in the CD8 T cell compartment. In this setting, CD8 T cells acquire a so-called exhausted state, which is characterized by the progressive loss of effector functions (i.e. the capacity to produce IL-2, TNFα, IFNγ)(16) and the reduced per-cell capacity to kill target cells(21) as a result of a high frequency of contacts between T cell receptor (TCR) and cognate antigen/major histocompatibility complexes I (MHC-I)(22). Clonal deletion of hyperreactive epitope-specificities(16), altered metabolism(23, 24), as well as the up-regulation of co-inhibitory receptors Programmed Cell Death Protein-1 (PD-1), Lymphocyte Activation Gene-3 (Lag3), T-cell immunoglobulin and mucin-domain containing-3 (Tim-3) among others(25, 26) are also cardinal features of exhausted CD8 T cells. Acquisition of an exhausted phenotype is crucial for host-pathogen equilibrium. A clear depiction of this can be found in several independent studies whereby reversion of the exhaustion state accelerated viral control at the expense of host survival(27-30). Besides inhibitory circuitry, exhausted CD8 T cells as a bulk were shown to possess unique transcriptional(31), epigenetic(32, 33), metabolic(23, 24) and developmental programs(34-39) that differed from those of effector or memory cells generated in the context of acute infections. More recently, the advent of single cell RNA sequencing technologies has allowed the discovery of previously unappreciated transcriptional heterogeneity of the exhausted CD8 T cell pool. In this regard, expression of T-cell factor-1 (TCF-1) has been shown to skew cells toward a progenitor-like phenotype(37-39) in a MYB-dependent fashion early after infection, which ensures Bcl-2 expression and survival(36). Importantly, TCF-1$^+$ precursor populations have been shown to originate as early as 4.5 days post-infection(40) and to give rise to both KLRG1$^+$ terminal effector cells early, as well as to exhausted subsets with different degree of functionality throughout chronic viral infection(36). For instance, a transitional subset stemming from TCF-1$^+$

precursors (defined by CX3CR1 and Tim3 co-expression) was recently shown to possess high cytotoxic potential and to be essential for viral control(34, 35). Functionally, TCF-1 endows cells with the capacity to self-renew and to give rise to downstream developmental fates that seed the exhausted CD8 T cell pool during chronic infections(37-39). In addition, this population contains the TCF-1^{+} $Tim3^{-}$ subset of cells, which is responsible for the CD8 T cell proliferative burst after PD-1/PD-L1 checkpoint blockade therapy(38). Interestingly, coordinated expression of transcription factors Eomesodermin (Eomes), T-box transcription factor 21 (T-bet), thymocyte selection associated high mobility group box (Tox) and TCF-1 developmentally link functionally and epigenetically distinct exhausted CD8 T cell subsets, which have been shown to possess distinct effector functions and differential responsiveness potential upon checkpoint blockade therapy(41). Overall, compounding evidence from the different studies mentioned hereby demonstrates that CD8 T cell exhaustion is a complex cellular state that involves functionally and developmentally heterogeneous fates. Given the implications of CD8 T cell exhaustion for human chronic infections as well as in cancers(19), the mechanisms driving the different exhausted fates as well as their implications for host resistance or tolerance during chronic infections and/or cancers are an important future avenue of research.

CD4 T cell adaptations during chronic viral infection

CD4 T cell responses can also dictate host-pathogen equilibrium during chronic infections. For example, CD4 T cells play essential roles in terminating lytic replication and in establishing viral latency in both human and murine hosts infected with herpes viruses, which subsequently prevents host morbidity(42). In this context, CD4 T cells directly mediate viral clearance beyond their role as helpers for B cell and CD8 T cell responses. In contrast, increased CD4 T cell antigen-

specific precursor pool frequencies and effector functions can drive immunopathology and subsequent host morbidity in the context of acute or persistent viral infections(43-46). Analogous to CD8 T cell exhaustion, CD4 T cells primed in the context of a persistent infection progressively lose their capability to produce IFNγ, TNFα and IL-2, they up-regulate surface expression of co-inhibitory receptors PD-1 and Lag3, among others, and they acquire a IFN-I transcriptional signature(47). However, whether CD4 T cells acquire a functionally exhausted state is debatable, as these cells can effectively provide help to CD8 T cells by producing IL-21 during chronic viral infection(48). In the same line, distinct patterns of transcription factor expression were shown for virus-specific CD4 T cells from persistently vs. acutely infected mice(47). For instance, antigen-specific CD4 T cells isolated from persistently infected mice had markedly reduced T-bet expression, consistent with the loss of effector functions(47), but increased Bcl6, Ikaros family zinc finger 2 (Helios) and Eomes(47), which are typically expressed by T-follicular helper (T_{FH})(49), T regulatory cells (T_{reg})(50) and by CD4 T cells with cytotoxic phenotypes(51-53), respectively. Moreover, developmental skewing toward a T_{FH}, rather than a T helper 1 (T_{H1}) phenotype, has been observed among virus specific CD4 T cells during persistent viral infection. Intriguingly, our laboratory found that this process was favored by CD4 T-cell intrinsic sensing of the gp130 cytokine IL-6, which was produced by follicular dendritic cells and was required for viral control(54). Importantly, T_{FH} responses were shown to be essential for the generation of neutralizing antibodies and for viral control of a persistent virus(55). Thus, adaptations of the CD4 T cell compartment in this context consist on the functional attenuation of canonical T_{H1} effector functions in parallel with the functional specialization toward a T_{FH} fate that sustains CD8 T cell and B-cell responses and promotes viral eradication after chronic viral infection.

Chapter 1: IFN-I and CD8 T cells increase intestinal barrier permeability after chronic viral infection

1.1 Summary and graphical abstract

Intestinal barrier leakage constitutes a potential therapeutic target for many inflammatory diseases and represents a disease progression marker during chronic viral infections. The causes of altered gut barrier remain, however, mostly unknown. By using murine infection with lymphocytic choriomeningitis virus we demonstrated that, in contrast to an acute viral strain, a persistent viral isolate led to long-term viral replication in hematopoietic and mesenchymal, but not epithelial (IEC), cells in the intestine. Viral persistence drove sustained intestinal epithelial barrier leakage, which was characterized by increased paracellular flux of small molecules and was associated with enhanced colitis susceptibility. IFN-I signaling caused tight junction dysregulation in IEC, promoted gut microbiome shifts and enhanced intestinal CD8 T cell responses. Notably, both IFN-I receptor blockade and CD8 T cell depletion prevented infection-induced barrier leakage. Our study demonstrated that infection with a virus that persistently replicated in intestinal mucosa increased epithelial barrier permeability and revealed IFN-I and CD8 T cells as causative factors of intestinal leakage during chronic infections.

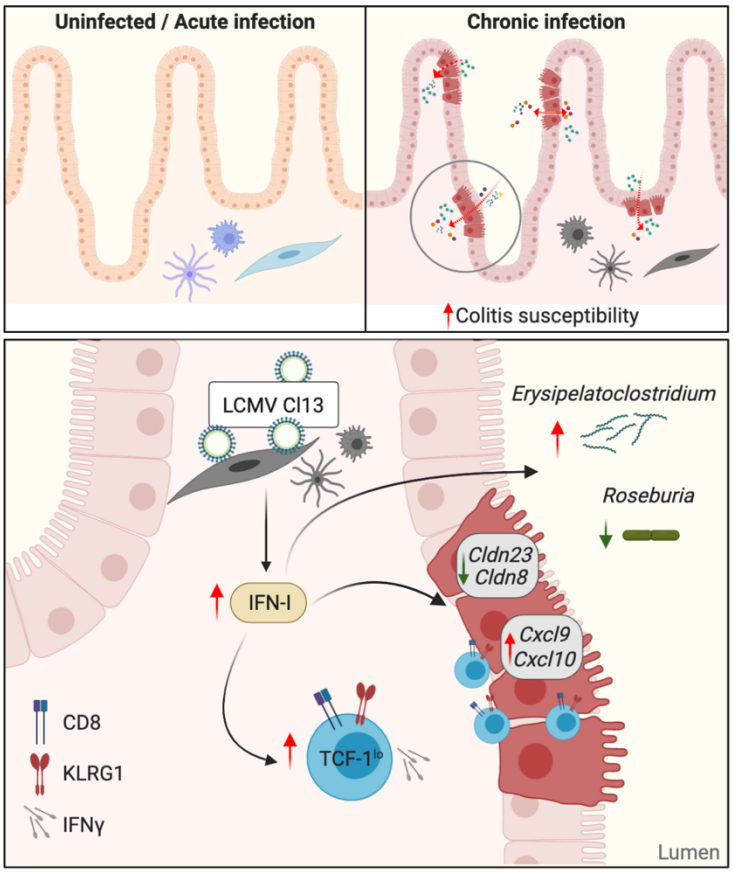

Figure 1-1. IFN-I and CD8 T cells increase intestinal barrier permeability after chronic viral infection

1.2 Introduction

The gastrointestinal (GI) tract harbors the gut microbiota and food components as well as their derived metabolites and a large number of immune cells, which cross-talk ensures intestinal homeostasis(56, 57). In order to prevent pathology, gut luminal contents need to be compartmentalized away from the host(58). This is achieved by the intestinal epithelium, which acts as a physical, immunological and selectively permeable barrier(59) that enables bi-directional flux of ions, water, nutrients and waste (60). There are three described routes of solute transport across the intestinal epithelium; the size and charge-restricted pore pathway, which allows paracellular ion and water exchange and is regulated by claudin proteins(58). The leak pathway, which permits paracellular passage of solutes up to 90 Å in diameter and requires activated myosin light chain kinase (MLCK) activity(61-63). Lastly, the unrestricted pathway allows passage of particles bigger than 100Å in diameter at sites of epithelial damage(64, 65).

Infections with chronic pathogens such as HIV or *Plasmodium* in humans and simian immunodeficiency virus (SIV) in rhesus macaques (RM) are associated with intestinal barrier dysfunction(66-68). For instance, peripheral immune activation, a strong predictor of disease progression in HIV-infected individuals, was proposed to stem from translocation of gut luminal components into the peripheral circulation as a result of an increasingly permeable intestinal epithelium(69). Epithelial barrier dysfunction was also described in SIV-infected RM, which develop immune activation and AIDS-related morbidity(69, 70). In spite of the prevalence of barrier dysfunction upon chronic viral infections, its underlying mechanisms remain largely undefined, in part due to the lack of small animal models in which interventional experiments can be performed.

In this study, we employed infection of mice with the acute (Armstrong, ARM) and persistent (Cl13) variants of LCMV to elucidate chronic infection-specific host adaptations in the GI tract. We found that chronic, but not acute LCMV, sustainably replicated in hematopoietic and mesenchymal, but not in epithelial cells within the small intestine. Chronic LCMV infection also resulted in long-term, size-selective increase in permeability of small molecular weight molecules, typically associated with the leak pathway of paracellular flux(64, 65). The transcriptional tight junction dysregulation associated with this barrier leakage required IFN-I signaling, which also influenced intestinal epithelial cell (IEC) proliferative capacity and glycolytic metabolism. In addition, IFN-I signaling increased IEC expression of the $CXCR3^{+}$-effector-T-cell chemoattractants *Cxcl9* and *Cxcl10*(71) and promoted CD8 T cell accumulation and effector functions within the small intestine. IFN-I signaling also promoted the overrepresentation of *Erysipelatoclostridium* and reduced the relative abundance of *Roseburia* in the intestinal microbiome of chronically infected mice, which associated with the induction of intestinal leakage. Importantly, both IFN-I receptor (IFNAR) blockade and CD8 T cell depletion fully abrogated the intestinal permeability increase after LCMV Cl13 infection. Lastly, we observed that viral persistence and increased barrier permeability associated with enhanced morbidity and mortality upon secondary chemical or microbial intestinal insults. Overall, our data established the existence of a previously unrecognized role for the IFN-I-CD8 T cell axis in the modulation of intestinal epithelial barrier function during chronic viral infection and raised the possibility that IFN-I may represent a cause, rather than a consequence, of microbial translocation during other chronic infections. Finally, our work put forward the usage of chronic LCMV infection in mice as a cost-effective model to study the biology of leaky gut at the whole organism level.

1.3 Results

1.3.1 LCMV Cl13 persists in mesenchymal and hematopoietic cells, but not in epithelial cells within intestinal tissues.

In order to investigate host adaptations to persistent LCMV infection in the GI tract, we first assessed the intestinal localization and replicating capacity of the persistent LCMV Cl13 isolate, in comparison to the acute LCMV ARM strain (14, 16). Immunofluorescence with anti-LCMV antibodies (Ab) revealed the presence of virus in the distal small intestines of Cl13- but not ARM-infected mice, on days 9 and 24 p.i. (Fig. 1-2A), consistent with a previous report (72). Importantly, plaque assays in ileum and colon homogenates indicated that the Cl13 (but not ARM) isolate productively replicated in this compartment at both day 9, 24 (Fig. 1-2B, left graph) and at day 300 p.i., after systemic viremia was cleared (Fig. 1-2B, right graph). We next investigated the cellular tropism of LCMV Cl13 in the intestine via immunofluorescence staining with anti-LCMV Ab in combination with Abs against CD45 or vimentin, which label hematopoietic and mesenchymal cells, respectively (73). We detected a significant overlap between LCMV signal and staining for both CD45 and vimentin at days 9 (Fig. 1-2C,E) and 24 (Fig. 1-2E and Fig. 1-3A) p.i. In contrast, co-staining of LCMV and EpCAM, a pan epithelial cell marker (74), did not overlap at any of the two time-points assessed (Fig. 1-2D-E and Fig. 1-3B). Overall, these results indicate that systemically inoculated LCMV Cl13 virus persistently replicated along the ileum and colon, even after systemic viremia was cleared, and that its cellular targets included hematopoietic and mesenchymal, but not epithelial, cells within the intestinal mucosa.

1.3.2 LCMV Cl13 infection persistently increases intestinal permeability to small-sized molecules

We next sought to identify functional adaptations to persistent LCMV Cl13 infection along the GI tract. Among these, increased intestinal permeability has been reported during chronic viral infections in humans and non-human primates (67, 68). To test whether LCMV Cl13 infection also caused gut leakage, we performed an *in vivo* intestinal permeability assay with small molecular weight FITC-labeled 4 kDa dextran (FD4) (75) on days 3, 8, 20, 30, 45 and 60 after ARM or Cl13 infection, and in uninfected mice. FD4 flux from the gut lumen to the serum was not affected by ARM infection but was significantly increased in Cl13-infected mice (Fig. 1-2F). The FD4 permeability increase was detected, and peaked, at day 8 after Cl13 infection and persisted until day 45 p.i. (Fig. 1-2F). In contrast, permeability of the bigger-sized FITC-labeled 40 kDa dextran (FD40) was not increased in Cl13- versus ARM-infected or uninfected mice (Fig. 1-4A). Consistent with this, histologic examination failed to identify epithelial damage within the small and large intestines from Cl13- or ARM-infected mice at days 9 or 24 p.i. (Fig. 1-4B&C). Together, the lack of apparent epithelial cell damage and/or ulceration and the unchanged FD40 permeability ruled out involvement of the unrestricted pathway of solute exchange (64, 65) at the time-points studied. Instead, our data indicated that infection with Cl13, but not ARM, caused a sustained increase in intestinal permeability of small molecular weight molecules typically associated with the leak pathway of paracellular flux (64, 65).

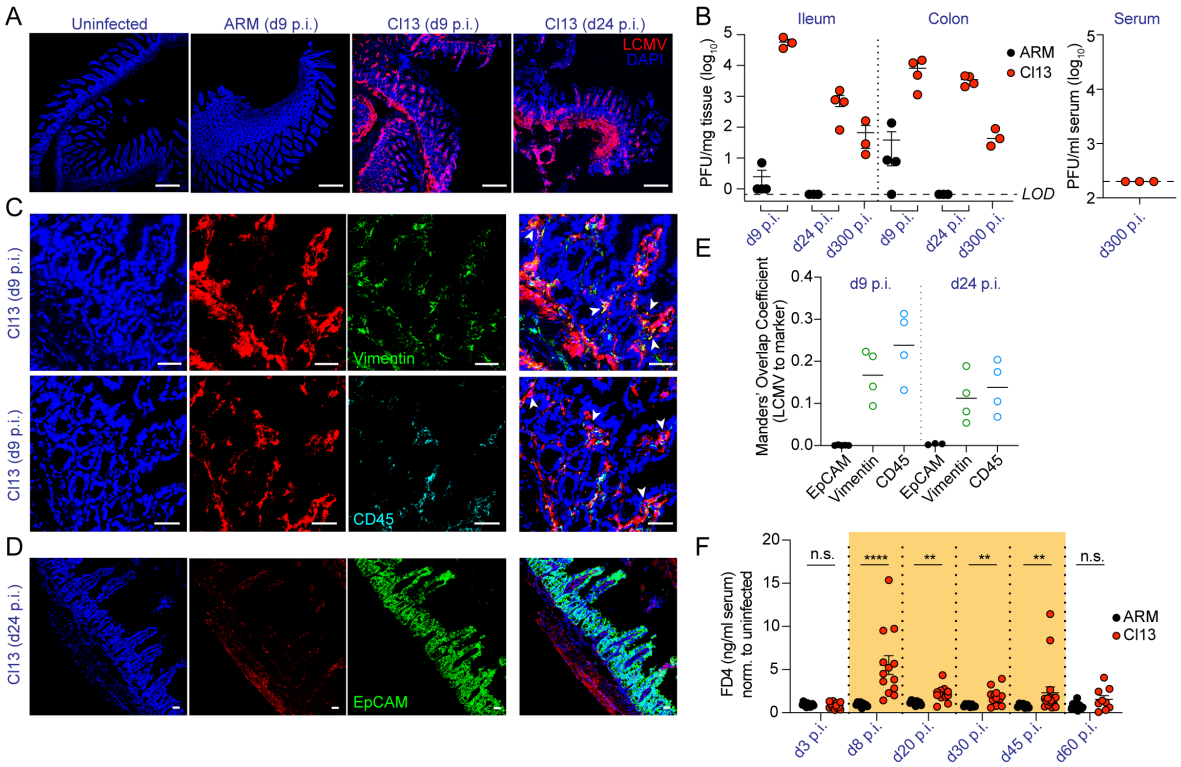

Figure 1-2. LCMV Cl13 persists in small intestinal mesenchymal and hematopoietic but not epithelial cells and increases intestinal permeability to small-sized molecules. C57BL/6 mice were infected with LCMV ARM, Cl13 or left uninfected and analyzed at indicated time points post-infection (p.i.). (A,C,D) Representative immunofluorescence staining of ileum sections with anti-LCMV antibodies (red) and DAPI (blue) as well as anti-Vimentin (green) or anti-CD45.2 (cyan) antibodies (C), or anti-EpCAM (green) antibody (D), are shown. Scale bars represent 230μm (A) or 36μm (C,D). (B) LCMV plaque forming units (PFU) in ileum and colon, limit of detection (LOD) is indicated by dotted lines. (E) Mander's overlap coefficient between LCMV and EpCAM, Vimentin or CD45 markers. (F) *In vivo* intestinal permeability to 4 kDa FITC-dextran was measured in ARM- and Cl13-infected mice and normalized to levels in uninfected mice. Averages (E) and averages±standard error of the mean (S.E.M.) (B,F) are shown. Data are representative of 2 (A-E) or pooled of 2 (F) independent experimental repeats with n=3-8 mice/group . Kolmogorov-Smirnov test (F); *p-val<0.05, **p-val<0.01, ***p-val<0.001, ****p-val<0.0001.

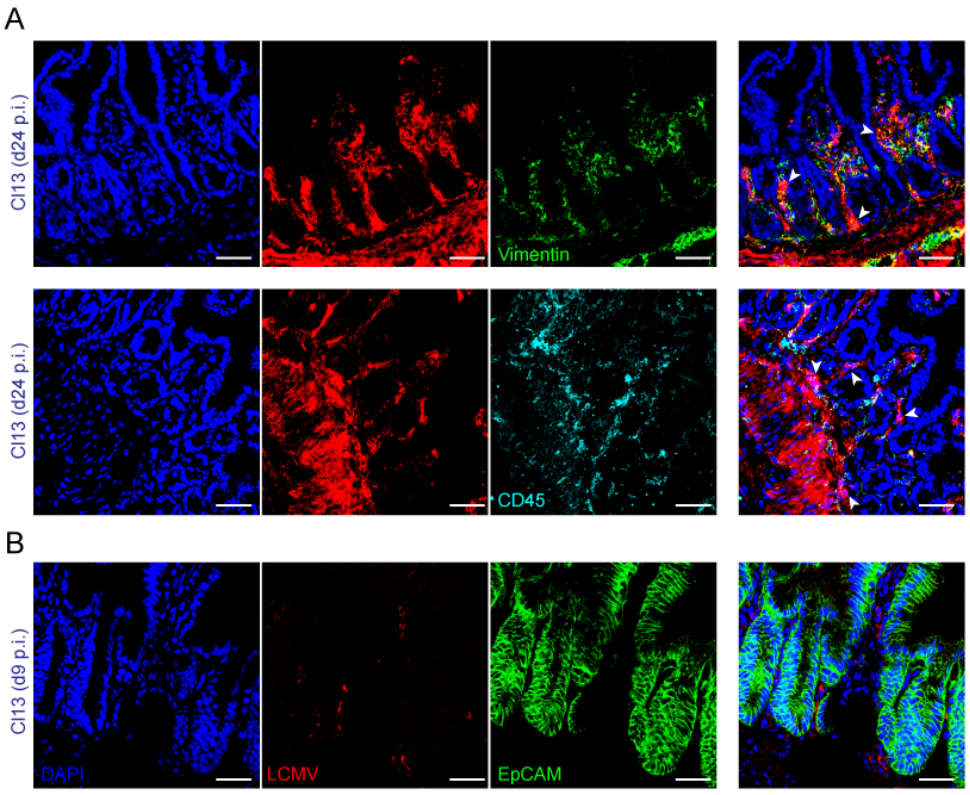

Figure 1-3. LCMV Cl13 infects intestinal mesenchymal and hematopoietic cells, but not epithelial cells. C57BL/6 mice were infected with LCMV ARM, Cl13 or left uninfected. Representative immunofluorescence staining of ileum sections with anti-LCMV antibodies (red) and DAPI (blue) as well as anti-Vimentin (green, A, top) or anti-CD45.2 (cyan A, bottom), or anti-EpCAM (green) (B) antibodies at indicated time points p.i. All scale bars correspond to 36μm. Data are representative of two independent experimental repeats with n=4 mice/group.

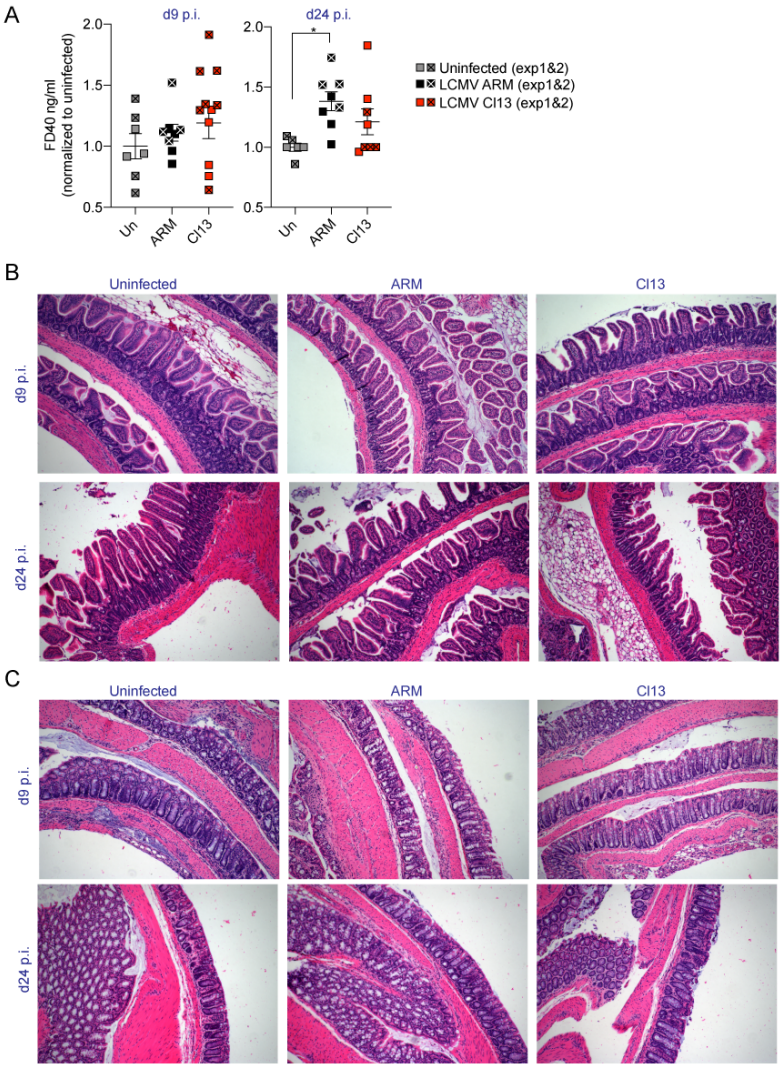

Figure 1-4. LCMV Cl13 infection neither increases intestinal permeability to 40 kDa FITC-dextran nor causes epithelial layer disruption. C57BL/6 mice were infected with LCMV ARM, Cl13 or left uninfected and analyzed at indicated time points p.i. (A) *In vivo* intestinal permeability to 40 kDa FITC-dextran was measured in ARM- and Cl13-infected mice and normalized to levels in uninfected mice. (B-C) Hematoxylin/Eosin staining of small (B) and large (C) intestinal sections. (A) Averages ± S.E.M. are shown. (A) Data are pooled from two experimental repeats where statistical significance was achieved in one out of two experiments or upon pooling. (B,C) Data are representative of two independent experimental repeats. Kruskal-Wallis with Dunn's multiple comparisons correction (A). *p-val<0.05.

1.3.3 LCMV Cl13 infection induces dysregulation in tight junction gene expression as well as an IFN-I signature in IEC.

To elucidate the mechanisms driving increased intestinal barrier permeability during LCMV Cl13 infection, we next performed transcriptomic analysis of FACS-purified IEC ($CD45^-$ $EpCAM^+$) from the small intestine of mice left uninfected or infected with ARM or Cl13 at day 9 p.i. IEC purity was assessed via FACS (average purity=96.4%±4.4). Notably, while both ARM and Cl13 infections induce a vigorous immune response at this time-point (16), Cl13 infection exerted much greater IEC-intrinsic transcriptional perturbations than ARM infection. Specifically, the number of differentially regulated genes (DEG) (with cut-offs at adjusted p-value<0.05 and minimal fold-change=2) was 41 in ARM-infected vs. uninfected, and 642 in Cl13-infected vs. uninfected mice (Fig. 1-5A and Dataset S1-1&1-2). In addition, Cl13-infected mice clustered more distantly from uninfected mice than ARM-infected mice by principal component 1 on a principal component analysis (PCA) plot (Fig. 1-5B). Given that size-selective increase in paracellular transport upon Cl13, but not ARM, infection were consistent with the engagement of the leak pathway that is caused by tight junction dysregulation (64, 65), we next assessed expression of several tight junction-related genes extracted from MSigDB or previous studies (76-78). We did not observe differences in any of the 29 genes analyzed in ARM-infected vs. uninfected mice (Dataset S1-3). In contrast, we detected significant downregulation in Cl13- vs. ARM-infected and uninfected mice of *Cldn23* and *Patj* (Fig. 1-5C), which encode for claudin-23 and Pals-associated tight junction protein, respectively. We also observed significant downregulation of *Cldn3* and *Cldn8*, in Cl13-infected vs. uninfected mice and observed the same tendency but without reaching significance when compared Cl13-infected to ARM-infected mice (Fig. 1-5C). Overall, these data indicated that LCMV Cl13 infection resulted in IEC- downmodulation of tight junction gene

expression, which was consistent with the aforementioned increase in intestinal barrier permeability.

To identify signals underlying tight junction dysregulation as well as increased paracellular transport between ARM- and Cl13-infected mice, we performed Gene Set Enrichment Analysis (GSEA) of the IEC transcriptomes with Hallmarks (76), KEGG (79) and Reactome (80) databases. This analysis identified positive enrichment for inflammatory pathways such as IFNγ and IFNα responses as well as IL-6 and IL-2 signaling, among others (Fig. 1-5D, Table S1-4). Cl13-infected mice also up-regulated pathways related to cell cycle (Myc and E2F targets and G2M checkpoint) and metabolism ('mTORC1 signaling' and 'pancreas beta cells') compared to ARM-infected mice (Fig. 1-5D). We further detected down-modulation of pathways related to xenobiotic, bile acid and heme metabolism, estrogen signaling (Fig. 1-5D) and 'Slc-mediated transmembrane transport' or 'Digestion and absorption' (Table S1-4). On the other hand, direct comparison of IEC transcriptomes from ARM- vs. Cl13-infected mice identified 394 DEG, 150 of which were down-regulated and 244 were up-regulated by Cl13 infection (Fig. 1-5E and Table S1-5). Consistent with pathway analysis, a notable fraction of down-regulated genes were related to nutrient transport, such as solute carrier family genes *Slc36a1, Slc2a2*, *Slc9a3*, *Slc46a1,* or *Slc15a1* (Fig. 1-5E and Table S1-5)*,* which encode for amino acid, glucose, ion, folate, and peptide transporters, respectively (81-85). Other down-regulated genes were related to immune defense, such as *Reg3a* and *Reg3b,* which encode for C-type lectins with bactericidal activity (86, 87) and *Il33*, which is involved in tissue repair responses (88) (Fig. 1-5E). In contrast the vast majority of genes and pathways up-regulated in IEC from Cl13- vs. ARM-infected mice were related to the antiviral immune response. Specifically, we observed increased expression of interferon-stimulated genes (ISG) *Mx1, Isg15, Mx2, Tap1, Cxcl9* and *Cxcl10*, among others (Fig. 1-5E and Table S1-5).

Overall, our data demonstrated that, chronic LCMV replication in intestinal tissues associated with worse bactericidal response, tissue repair and transcellular nutrient transport capacities of the intestinal epithelium, which could have implications for limiting close contact with the microbiota, for protection against secondary insults and/or whole-body nutrition. Viral persistence also promoted an anti-viral transcriptional program in IEC consistent with enhanced IFN-I signaling that associated with tight junction dysregulation and induction of a leaky gut phenotype.

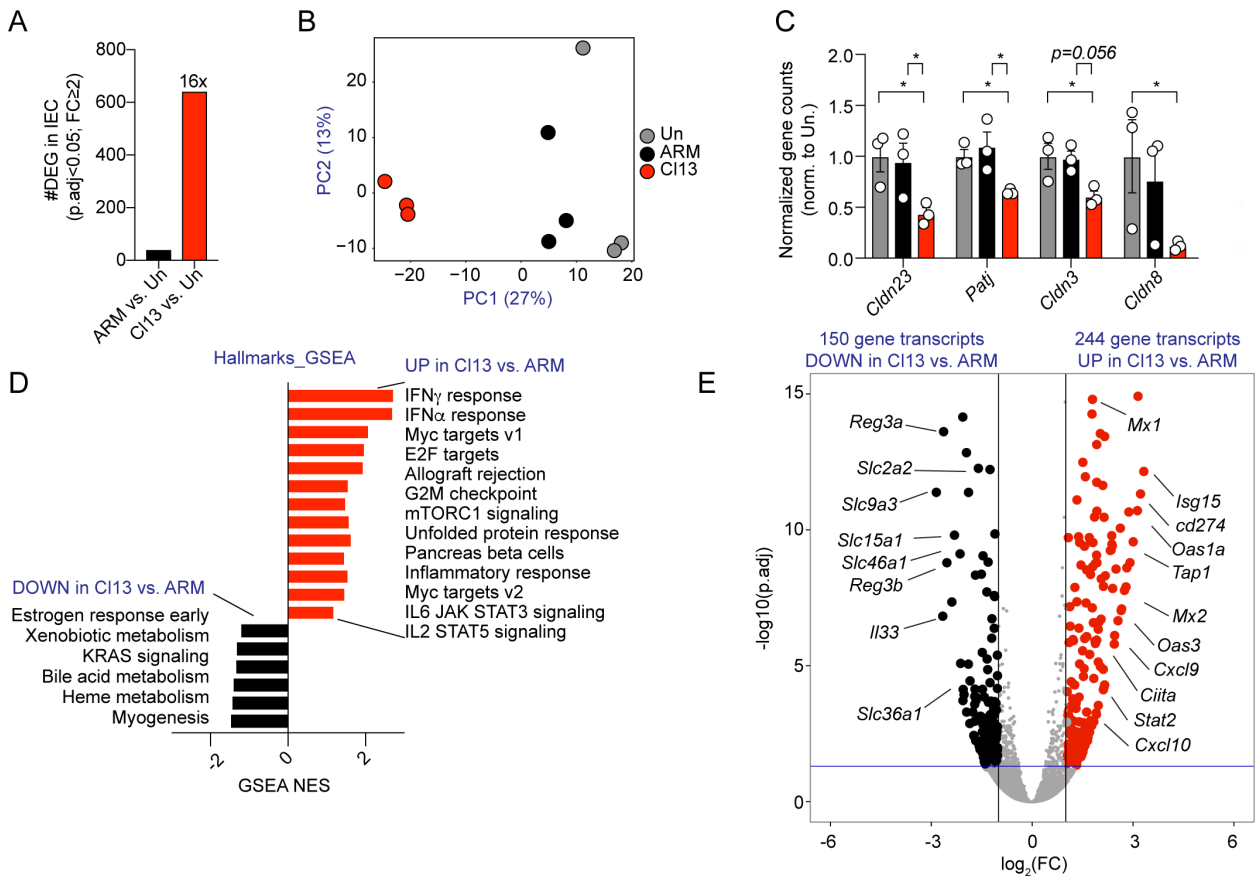

Figure 1-5. LCMV Cl13 infection induces dysregulation in tight junction gene expression as well as an IFN-I signature in intestinal epithelial cells. C57BL/6 mice were infected with LCMV ARM, Cl13 or left uninfected (Un) and RNA sequencing analysis was performed on FACS-purified IEC on day 9 p.i. (A) Number of differentially-expressed genes (DEG) with adjusted p-value (p.adj)<0.05 and fold change (FC)≥2 between IEC from ARM- or Cl13-infected vs. uninfected mice. (B) Principal Component Analysis (PCA) plot with IEC transcriptomes from uninfected, ARM- and Cl13-infected mice. (C) Gene counts by DESeq2 for indicated genes were normalized to average counts in the uninfected group. (D) Differentially-enriched pathways (p-val<0.05 and FDR<0.25) in ARM- vs. Cl13-infected mice by GSEA. (E) DEG in ARM- vs. Cl13-infected mice. RNAseq was performed in a total of 3 independent experiments, in which each sequenced sample consists of IEC pooled from 3 mice. Averages ± S.E.M. are shown (C). (A,E) DEG, (B) PCA and (C) FDR-adjusted p-values were computed by DESeq2. *p.adj<0.05.

1.3.4 IFN-I signaling increases intestinal permeability and immune cell recruitment genes while down-regulating tight junction-related genes in IEC from LCMV-Cl13-infected mice.

To investigate the potential causal role of IFN-I in the enhancement of intestinal barrier permeability during chronic viral infection, we blocked signaling through its receptor via intraperitoneal (i.p.) injection of anti-IFNAR-1 or isotype control Ab from day -1 and through day 9 p.i. with Cl13 (89, 90). While anti-IFNAR-1 Ab treatment did not alter FD4 translocation in uninfected mice (compared to isotype control mice), we observed a significant reduction in serum FD4 levels in anti-IFNAR-1- vs. isotype-treated Cl13-infected mice, with FD4 permeability returning to uninfected mouse levels in the Cl13-infected mice that received the IFNAR-1 Ab treatment (Fig. 1-6A). Thus, IFN-I signaling was essential to increase paracellular flux of small molecules through the intestinal epithelium during Cl13 infection.

To identify the mechanism employed by IFN-I to increase intestinal barrier leakage, we next performed RNA sequencing analysis of FACS-purified IEC from isotype- or anti-IFNAR-1-treated Cl13-infected mice on day 9 p.i. IEC purity was assessed via FACS (average purity=96.5%±3.2). This treatment had a significant impact on IEC transcriptomes, since IEC from isotype-treated mice clustered away from anti-IFNAR-1-treated Cl13-infected mice by PC1 (Fig. 1-6B). In addition, antibody treatment readily reduced IFN-I signaling in IEC, since the hallmark IFNα response pathway and expression of several ISG was significantly enriched in isotype- vs. anti-IFNAR-1-treated Cl13-infected mice (Fig. 1-7A&B and Dataset S1-6&S1-7). By analyzing overlap of all differential pathways and DEG from the aforementioned Cl13 vs. ARM comparison (Fig. 1-6D-E and Dataset S1-4&S1-5) with those altered in isotype- vs. anti-IFNAR-1-treated Cl13-infected mice, we found that IFN-I signaling explained 34% and 37% of altered pathways and DEG in Cl13 infected mice, respectively (Fig. 1-6C-D). At the pathway level, we found that

IFN-I down-modulated xenobiotic metabolism but promoted mTORC1 metabolism, glycolysis, cell cycle and several pro-inflammatory pathways (Fig. 1-6C and Dataset S1-8). Among transcripts significantly down-regulated by IFN-I signaling, we found those encoding for proteins related to cellular metabolism (*Acsm3* and *Sord* among others), solute transport (*Abcg8, Abcg5, Slc9a3*) immune defense (*Il33, Tcim*, *Socs1)* as well as several ISG (Fig. 1-6E and Dataset S1-9). Most importantly, we found that IFN-I signaling down-regulated expression of tight junction-encoding genes *Cldn8*, *Cldn15* and *Cldn23* (Fig. 1-6E and Table S1-7), two of which we found to be down-regulated in Cl13- vs. ARM-infected and/or uninfected mice (Fig. 1-5C). In contrast, the vast majority of genes up-regulated by IFN-I (Fig. 1-6E and Table S1-9) were related to immune processes and included genes such as *Cxcl10, Cxcl9, Icam1* or *Csf1*, whose products can contribute to T-cell recruitment (71) as well as adhesion (91) and maturation of innate immune cell types (92).

Overall, our data indicated that IFN-I signaling was responsible for the increased intestinal permeability and for the induction of metabolic, proliferative and pro-inflammatory transcriptional pathways in IEC after chronic LCMV infection. Remarkably, IFN-I signaling was responsible for tight junction transcriptional dysregulation and promoted expression of immune cell recruitment genes *Cxcl9* and *Cxcl10* in IEC from chronically infected mice.

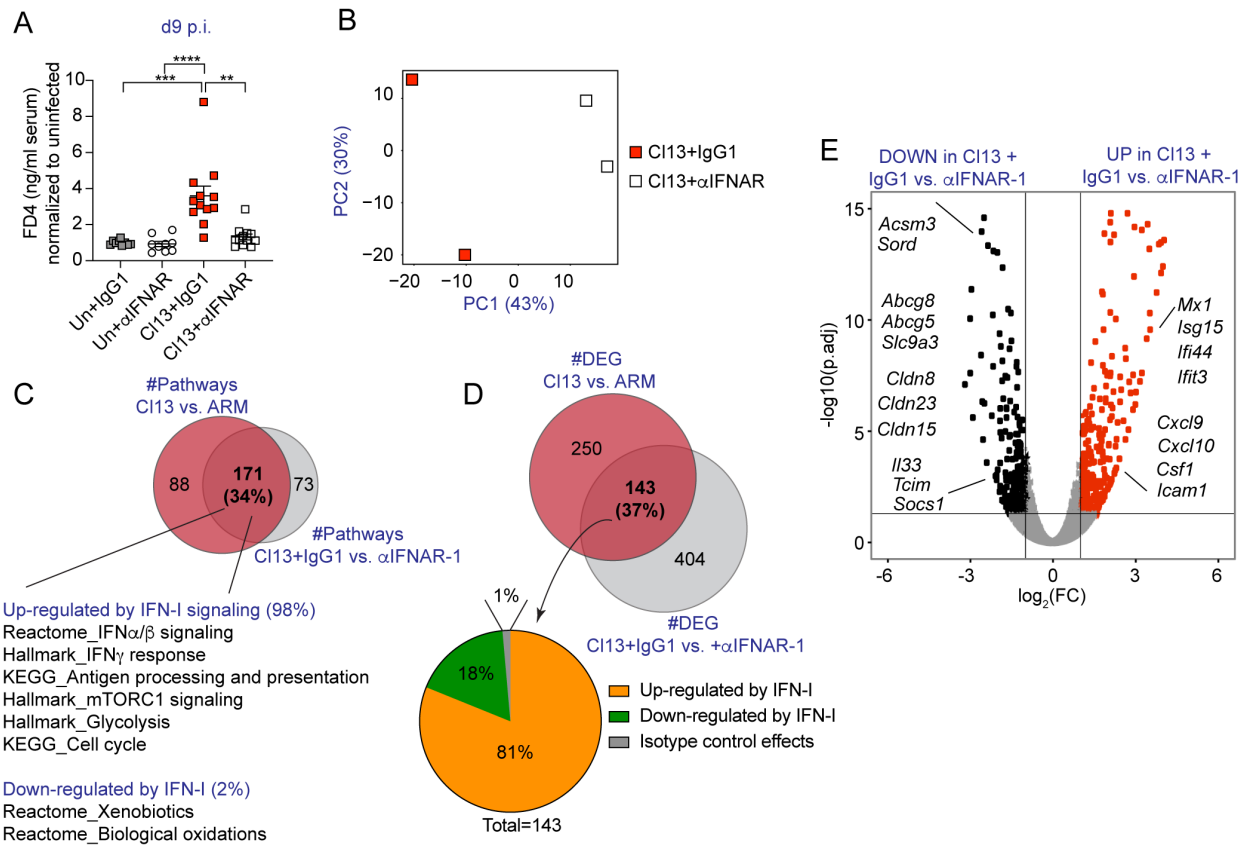

Figure 1-6. IFN-I signaling increases intestinal permeability and immune cell recruitment genes while down-regulating tight junction-related genes in IEC from LCMV-Cl13-infected mice. C57BL/6 mice were infected with LCMV Cl13 or left uninfected (Un) and injected with isotype (IgG1) or anti-IFNAR-1 Ab (αIFNAR) intraperitoneally (i.p.), and analyzed at day 9 p.i. (A) *In vivo* intestinal permeability to 4 kDa FITC-dextran. (B-E) RNA sequencing was performed in IEC. (B) Principal Component Analysis plots showing individual samples from IgG1- vs. αIFNAR-treated Cl13-infected mice. Venn diagram overlapping (C) pathways or (D) DEG from Cl13 vs. ARM (data from Figure 2) and Cl13-infected plus IgG1 vs. αIFNAR treatment comparisons. (E) DEG in IEC transcriptomes from IgG1- vs. αIFNAR-treated Cl13-infected mice. Averages ± S.E.M. are shown (A). (A) Data are pooled from three independent experimental repeats with n=3-4 mice/group. (B-E) RNAseq was performed in a total of 2 independent experiments, in which each sequenced sample consists of IEC pooled from 3 mice. (B) PCA and (C-E) DEG were calculated by DESeq2. (A) Kruskal-Wallis test with Dunn's correction for multiple comparisons. (C) Pathway enrichment was determined by GSEA (p-val<0.05 and FDR<0.25). *p-val<0.05, **p-val<0.01, ***p-val<0.001, ****p-val<0.0001.

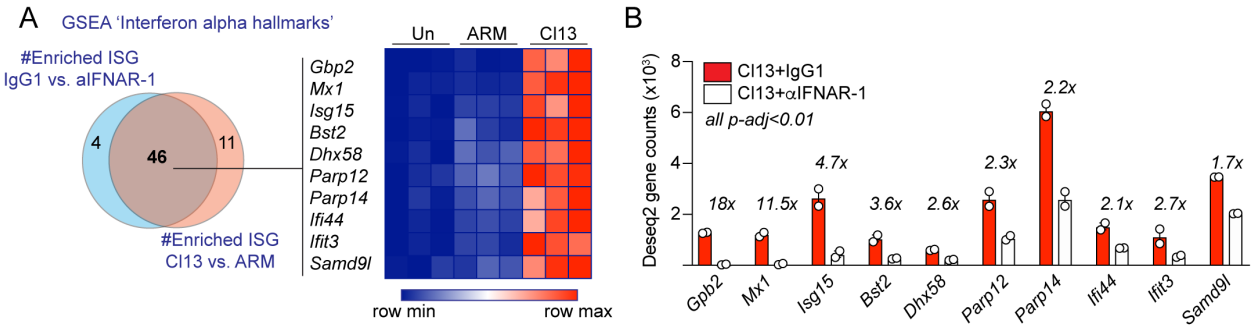

Figure 1-7. Antibody-mediated blockade of IFNAR-1 reduces interferon signaling in IEC after LCMV Cl13 infection. C57BL/6 mice were infected with LCMV ARM, Cl13 or left uninfected (Un) (A) or injected with isotype (IgG1) or anti-IFNAR-1 Ab (αIFNAR) intraperitoneally (i.p.) (A-B), and RNA sequencing analysis was performed on FACS-purified IEC at day 9 p.i. (A) Venn diagram (left) shows overlapping GSEA results from the 'Interferon alpha hallmarks' gene signature between IEC from Cl13- vs. ARM-infected mice and IEC from IgG1- vs. anti-IFNAR-1 treated Cl13-infected mice. 10 highly enriched, and overlapping, interferon-stimulated genes (ISG) (i.e. Highest rank metric scores, FDR<0.1) were selected for Heatmap (right) depicting Z-scores computed from DESeq2 normalized counts (Table S2, S5, S7). (B) Fold reduction in the expression of selected ISG in IEC from IgG1-treated vs. anti-IFNAR-1-treated Cl13-infected is shown. (B) Averages ± S.E.M. are shown. FDR-adjusted p-values (p-adj) were computed by DESeq2.

1.3.5 Intestinal CD8 T cell responses are enhanced by IFN-I and are essential for barrier leakage during chronic LCMV Cl13 infection.

IFN-I acts as a third signal to CD8 T cells during viral infections and promotes T cell accumulation and effector functions (93). In addition, IFN-I induces a cell-intrinsic antiviral state (93) and can modulate immune cell recruitment to mucosal tissues in response to infections (94-97). We found that IEC from Cl13-vs. ARM-infected mice expressed higher levels of *Cxcl9* and *Cxcl10* in a IFN-I-dependent manner (Fig. 1-5E and 1-6E). Since CXCL9 and CXCL10 can be responsible for the recruitment of CXCR3-expressing effector CD4 and CD8 T cells (71), we hypothesized that IFN-I could be mediating recruitment of T cell populations relevant for the induction of barrier dysfunction. To test this hypothesis, we first investigated CD4 T cell responses in the small intestine of Cl13-infected mice treated with isotype- or anti-IFNAR-1 Ab. Analysis of CD4 T cells specific for the immunodominant GP_{67-77} LCMV epitope ($I\text{-}A^bGP_{67-77}^+$) (98, 99)

revealed no differences in proportions, but increased numbers of I-A^{b}GP$_{67-77}^+$ CD4 T cells infiltrating the intraepithelial lymphocyte (IEL) and lamina propria compartments (LP) of the small intestine in anti-IFNAR-1- vs. isotype-treated Cl13-infected mice at day 9 p.i (Fig. S4A). Expression levels of the co-inhibitory receptor PD-1 on LCMV-specific CD4 T cells were increased upon anti-IFNAR-1 treatment (Fig. 1-9B). Furthermore, we observed reduced proportions of IFNγ-producing CD4 T cells upon *ex vivo* re-stimulation with Phorbol-Myristate-Acetate (PMA) and Ionomycin or with GP$_{67-77}$ peptide in the LP of anti-IFNAR-1- vs. isotype-treated Cl13-infected mice (Fig. 1-9C,E), although the total numbers of IFNγ-producing CD4 T cells (Fig. 1-9C,E) or their potential to co-produce TNFα (Fig. 1-9D) were unchanged by anti-IFNAR-1 treatment. Contrary to our hypothesis, these data showed that IFN-I restricted (rather than enhancing) I-A^{b}GP$_{67-77}^+$ CD4 T cell accumulation in the small intestine, uncoupling *Cxcl9* and *Cxcl10* expression by IEC to CD4-T cell recruitment to this tissue. Consistently, i.p. treatment of Cl13-infected mice with anti-CD4 or isotype Ab on days -2, -1, 0 and 5 p.i, did not counteract the increased barrier permeability observed at day 9 p.i. (Fig. 1-9F), even though this treatment was very efficient at reducing CD4 T cell accumulation in spleen and small intestine (Fig. 1-9G). These data indicated that increased barrier permeability after Cl13 infection occurred to the same extent in the absence of antiviral CD4 T cell responses.

We next profiled intestinal antiviral CD8 T cell responses in the same Cl13-infected mice treated with isotype- or anti-IFNAR-1 Ab. In contrast to the aforementioned observations in the CD4 T cell compartment, we detected reduced numbers of CD8 T cells specific for the LCMV immunodominant epitope GP$_{33-41}$ (D^{b}GP$_{33-41}^+$) (16) in both IEL and LPL from anti-IFNAR-1- vs. isotype-treated mice, although frequencies were only reduced in the IEL compartment (Fig. 1-8A). D^{b}GP$_{33-41}$tetramer$^+$ cells from anti-IFNAR-1- vs. isotype-treated mice expressed higher levels of

PD-1 (Fig. 1-8B), which might be related to a tendency (albeit not statistically significant) towards higher viral loads in the anti-IFNAR-1 treated group (Fig. 1-8C). In addition, lower frequencies of the D^bGP_{33-41}tetramer$^+$ cells were positive for inhibitory killer cell lectin-like receptor G1 (KLRG1), a cytolytic-associated molecule that marks CD8 T cells with an effector fate (100) (Fig. 1-8D). We detected higher proportion and number of stem-like TCF-1^{hi}Tim3^{lo} $D^bGP_{33-41}{}^+$ cells (37-39) in the IEL of anti-IFNAR-1 vs. isotype-treated mice (Fig. 1-8E), which was remarkable as this stem-like subset is typically absent from this tissue compartment (38). Conversely, frequencies and numbers of TCF-1^{lo} $D^bGP_{33-41}{}^+$, which includes cells with increased cytolytic potential (34, 35), were reduced in anti-IFNAR-1-treated Cl13-infected mice (Fig. 1-8E). At the functional level, we detected significantly lower frequencies and numbers of CD8 T cells with the capacity to co-produce IFNγ/TNFα upon *ex vivo* re-stimulation with PMA/Ionomycin and with cognate antigens in anti-IFNAR-1- vs isotype-treated Cl13-infected mice (Fig. 1-8F&H). Also, CD8 T cells from anti-IFNAR-1-treated mice produced lower levels of IFNγ on a per-cell basis after PMA/Ionomycin re-stimulation (Fig. 1-8G).

Since IFN-I-mediated increase in intestinal CD8 T cell accumulation and effector CD8 T cell phenotype associated with enhanced intestinal permeability in Cl13 infected mice, we next hypothesized that CD8 T cells may be contributing to intestinal leakage. To test this hypothesis, we treated Cl13-infected mice with CD8-depleting or isotype Ab on days -2, -1, 0 and 5 p.i. This treatment was highly efficient at reducing CD8 T cells from both the spleen and the small intestine (spleen: 3.2-fold±1.1, LP:6.6-fold±0.01, IEL: 4.7-fold±3.9), and it significantly reduced FD4 permeability, reaching uninfected levels in CD8-depleted Cl13-infected mice (Fig. 1-5I), in spite of increased intestinal viral loads and *Ifnb* levels (Fig. 1-8J&K).

Together, these data demonstrated that CD8 T cell responses, whose effector functions, accumulation and TCF-1^{lo} phenotype were reinforced by IFN-I, were essential causative factors of the increased intestinal permeability observed during chronic LCMV infection. Our results also uncoupled the induction of intestinal leakage from direct effects of viral loads and showed that increased *Ifnb* levels could not increase intestinal permeability in the absence of CD8 T cells during chronic LCMV infection.

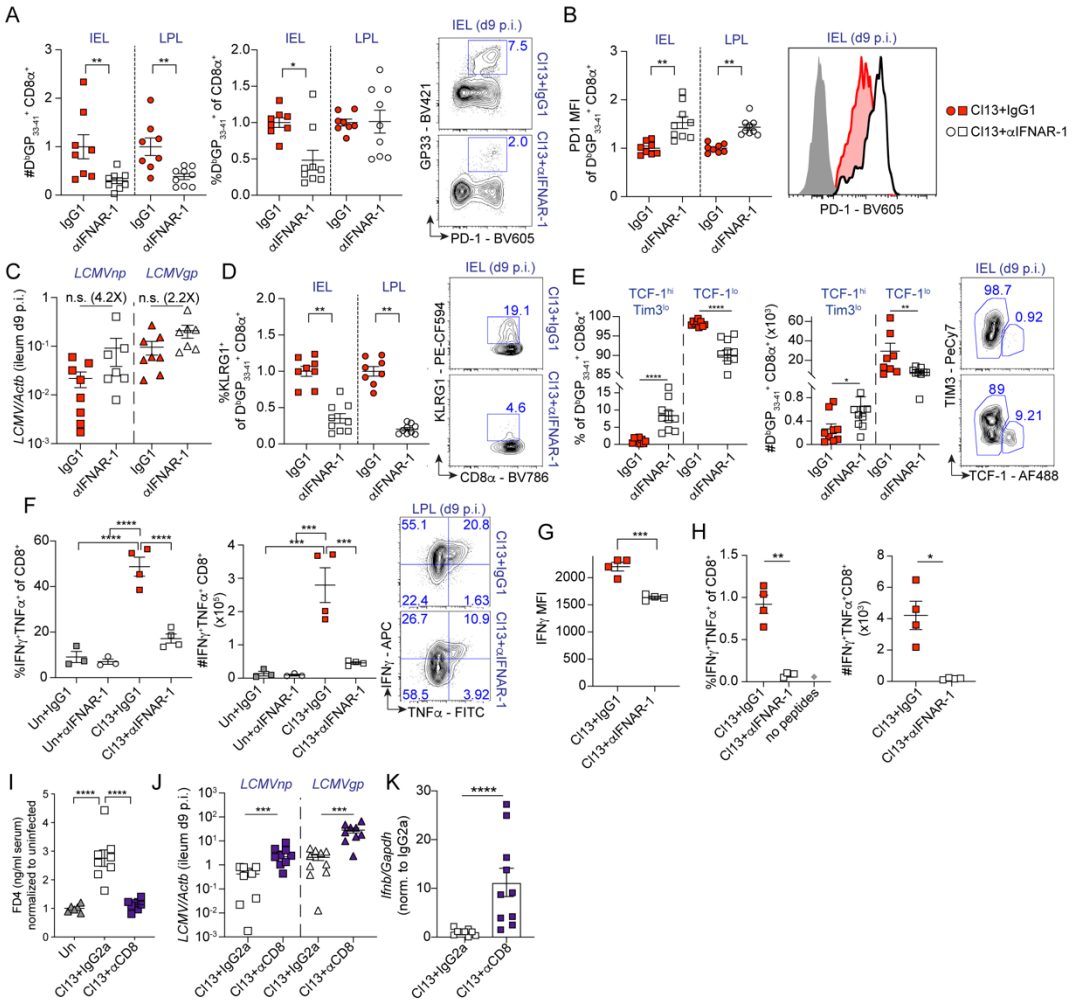

Figure 1-8. Intestinal CD8 T cell responses are enhanced by IFN-I and are essential for barrier leakage during chronic LCMV Cl13 infection. (A-H) C57BL/6 mice were infected with LCMV Cl13 or left uninfected (Un) and injected with isotype (IgG1, red) or anti-IFNAR-1 Ab (αIFNAR, white) intraperitoneally (i.p.). (A-B,D-H) FACS analysis of the small intestinal intraepithelial lymphocyte (IEL) or lamina propria lymphocyte (LPL) compartments was done on day 9 p.i. (A) Frequencies and numbers of $D^bGP_{33-41}^+$ CD8 T cells as well as (B) PD1 mean fluorescence intensity (MFI), (D) frequency of $KLRG1^+$ and (E) frequencies and numbers of $Tim3^{lo}TCF\text{-}1^{hi}$ or $TCF\text{-}1^{lo,}$ within $D^bGP_{33-41}^+$ CD8 T cells, and their corresponding representative FACS plots, are shown. (C) Viral RNA in ileum was quantified by q-PCR. (F-H) Frequencies, numbers (F-H) and representative FACS plots (F) as well as IFNγ MFI (G) of LPL CD8 T cells upon 5h of *ex vivo* PMA/Ionomycin stimulation (F-G) or with GP_{33-41}, $GP_{276-286}$, $NP_{396-404}$ peptides (H) are shown. (I-K) C57BL/6 mice were infected with LCMV Cl13 or left uninfected (Un) and injected with isotype ((IgG2a) or CD8 depleting antibodies (αCD8) i.p. *In vivo* intestinal permeability to 4 kDa FITC-dextran (I) as well as levels of viral RNA (J) and *Ifnb* (K) in the small intestine were determined on day 9 p.i. Averages ± S.E.M. are shown (A-K). Data are (A-E, J-K) pooled from two, (I) pooled from three or representative of three (F-G) or two (H) independent experimental repeats. (A-E,G-H,J-K) Mann-Whitney t-test, (F,I) Kruskal-Wallis with Dunn's multiple comparisons correction; *p-val<0.05, **p-val<0.01, ***p-val<0.001, ****p-val<0.0001.

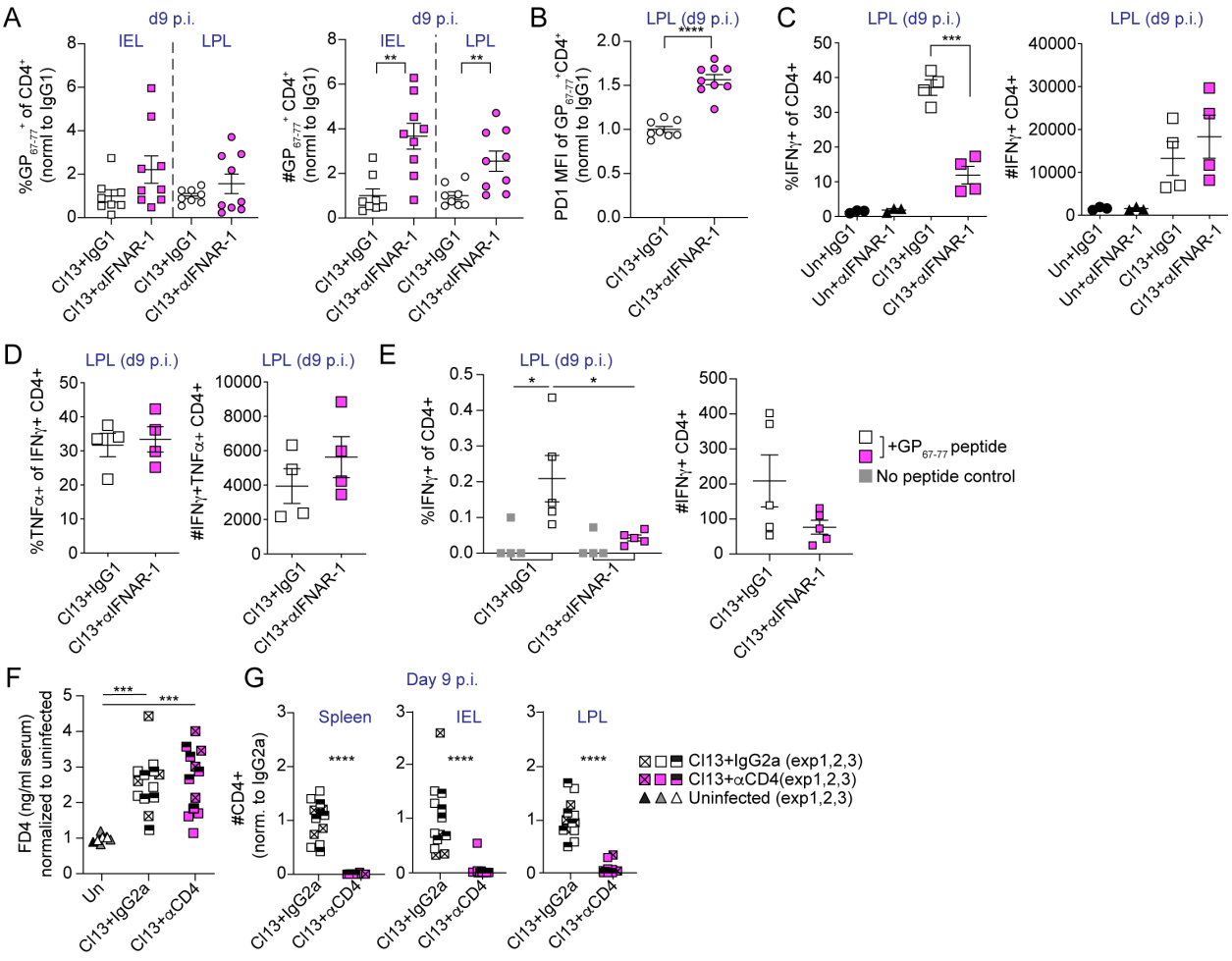

Figure 1-9. IFN-I signaling restricts small intestinal virus-specific CD4 T cell accumulation and CD4 T cells are dispensable for barrier dysfunction during LCMV Cl13 infection. C57BL/6 mice were infected with LCMV Cl13 and treated with isotype (IgG1) or anti-IFNAR-1 Ab (αIFNAR) (A-E) or with anti-CD4 (αCD4) or isotype Ab (IgG2a) i.p. on days -2, -1, 0 and 5 p.i. (F-G), and analyzed on day 9 p.i. (A-F) FACS analysis of the small intestinal intraepithelial lymphocyte (IEL) or lamina propria lymphocyte (LPL) compartments was done on day 9 p.i. (A-B) Frequencies and numbers (A), PD1 mean fluorescence intensity (MFI) (B) of I-A^{b}GP$_{67-77}^+$ CD4 T cells. (C-E) Cytokine production upon *ex vivo* PMA/Ionomycin (C-D) or GP$_{67-77}$ peptide (E) stimulation of LPL cells. (F) *In vivo* intestinal permeability to 4 kDa FITC-dextran. (G) Numbers of I-A^{b}GP$_{67-77}^+$ in indicated organs. (A-G) Averages ± S.E.M. are shown. Data are pooled of two (A,B), pooled of three (F,G) or representative (C-E) of two independent experimental repeats with n=3-5 mice/group. Although a tendency was consistently observed in all independent experiments, statistical significance was reached in 1 out of 2 experiments in A (right) and E (left, white v.s. pink squares). Statistical significance between Cl13+IgG2a and Cl13+αCD4 was only reached in 1 out of 3 experiments (F). Two-tailed t-test (A,B,C), Mann-Whitney test (G) and Kruskal-Wallis test with Dunn's multiple comparisons' correction (E-G). *p-val<0.05, **p-val<0.01, ***p-val<0.001, ****p-val<0.0001.

1.3.6 IFN-I signaling promotes overrepresentation of *Erysipelatoclostridium* and reduces *Roseburia* in the intestinal microbiome after LCMV Cl13 infection

Increased intestinal permeability has been associated with compositional shifts of the intestinal microbiome (101-103). To investigate whether the induction of intestinal leakage was coupled with microbiome shifts after Cl13 infection, we performed two independent experiments where we treated 10 mice per group with isotype or anti-IFNAR-1 Ab followed by 16S rRNA amplicon (Fig. 1-10) or shotgun metagenomic (Fig. 1-11) sequencing, of DNA obtained from colonic and caecal contents on day 9 p.i. Sampling of caecal and colonic contents was chosen over stool pellets, as it allows detection of taxa abundant inside the large intestine, which may not necessarily be eliminated in stools (104). As shown in Fig. 1-10A and Fig. 1-11A, we observed no significant differences in intra-individual alpha-diversity between isotype-treated and anti-IFNAR1-treated Cl13-infected mice, as determined by the Shannon diversity index, which combines richness and evenness (105). We next assessed intra-group taxonomic diversity via phylogenetic and non-phylogenetic beta-diversity computation followed by principal coordinates analysis (PCoA). Phylogenetic and non-phylogenetic analysis of the 16S data revealed differential separation between isotype-treated and anti-IFNAR-1-treated groups by the first principal coordinate and statistically significant differences between both groups by permutational ANOVA (PERMANOVA) (Fig. 1-10B). This difference was, however, not confirmed by a non-phylogenetic shotgun metagenomics analysis of an independent cohort of mice from the same vendor (Fig. 1-11B&C). Moreover, analysis of phylum abundances indicated that the ratios of Firmicutes over Bacteroidetes as well as Verrucomicrobia over Firmicutes and Bacteroidetes were not significantly different in isotype- vs. anti-IFNAR-1-treated Cl13-infected mice in both cohorts, despite the biological and technical differences in these analyses (Fig. 1-10C-E and Fig. 1-11D-

F). Taken together, these data demonstrated that IFN-I-dependent intestinal leakage did not associate with large-scale microbiome shifts early after Cl13 infection.

We next performed Songbird multinomial regression analysis (106) to identify specific taxa perturbed by IFNAR-1 blockade. Among the taxa with cut-off ranks at 0.5 and -0.5, which indicate a moderate to high degree of perturbation, we found that IFN-I signaling decreased the relative abundance of *Roseburia* (rank 1.14) (Fig. 1-10F and Dataset S1-10) and one of its species (i.e. *Roseburia hominis,* rank 0.54) (Fig. 1-11G and Dataset S1-10). Conversely, IFN-I signaling promoted the overrepresentation of *Erysipelatoclostridium* (rank -1.79) (Fig. 1-10F and Dataset S11) and one of its species (i.e. *Clostridium cocleatum*, rank -1.60) (Fig. 1-11G and Dataset S1-10).

Overall, these data demonstrated that IFN-I signaling drove overrepresentation of *Erysipelatoclostridium* commensals as well as reductions in *Roseburia* after chronic viral infection. Although these data do not demonstrate a causal relationship between intestinal barrier leakage and microbiome composition, they do increase our understanding of the role of IFN-I in modulating the composition of the intestinal microbiome after chronic viral infection and provide an association between the induction of intestinal leakage and specific taxa perturbations.

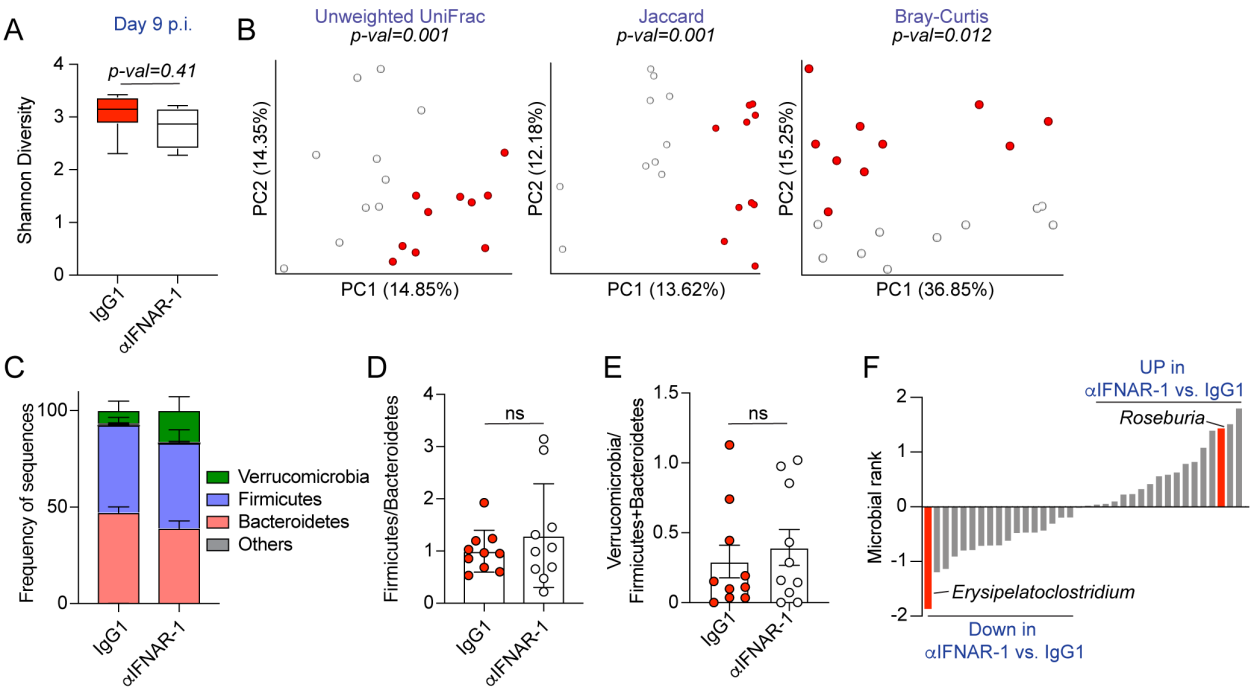

Figure 1-10. IFN-I signaling promotes overrepresentation of *Erysipelatoclostridium* and reduces *Roseburia* in the intestinal microbiome after LCMV Cl13 infection. C57BL/6 mice were infected with LCMV Cl13 and injected with isotype (IgG1) or anti-IFNAR-1 Ab (αIFNAR) intraperitoneally (i.p.) and sacrificed at day 9 p.i. 16S rRNA gene amplicon sequencing was performed on colonic and caecal contents. (A) Alpha diversity by the Shannon diversity index. (B) Beta-diversity PCoA with unweighted Unifrac, Jaccard and Bray-Curtis distances. (C) Frequency of sequences at the phylum level at indicated time-points. (D,E) Frequency of phylum Firmicutes divided by Bacteroidetes (D) or phylum Verrucomicrobia divided by Firmicutes and Bacteroidetes (E) for each individual mouse. (F) Songbird Multinomial Regression (MR) analysis of genera in IgG1-treated vs. αIFNAR-treated Cl13-infected mice. X-axes correspond to individual taxa. Taxa highlighted in red were consistently perturbed, in the same direction and with rank cut-offs of -0.5 and 0.5, after shotgun metagenomics analysis of an independent cohort of mice. (A-F). Data are representative of one independent repeat by 16S rRNA amplicon sequencing, with n=9-10 mice/group. (A,C-E) Averages ± min/max (A) or ± S.E.M. (C-E). (B) Significance was computed with PERMANOVA (999 permutations).

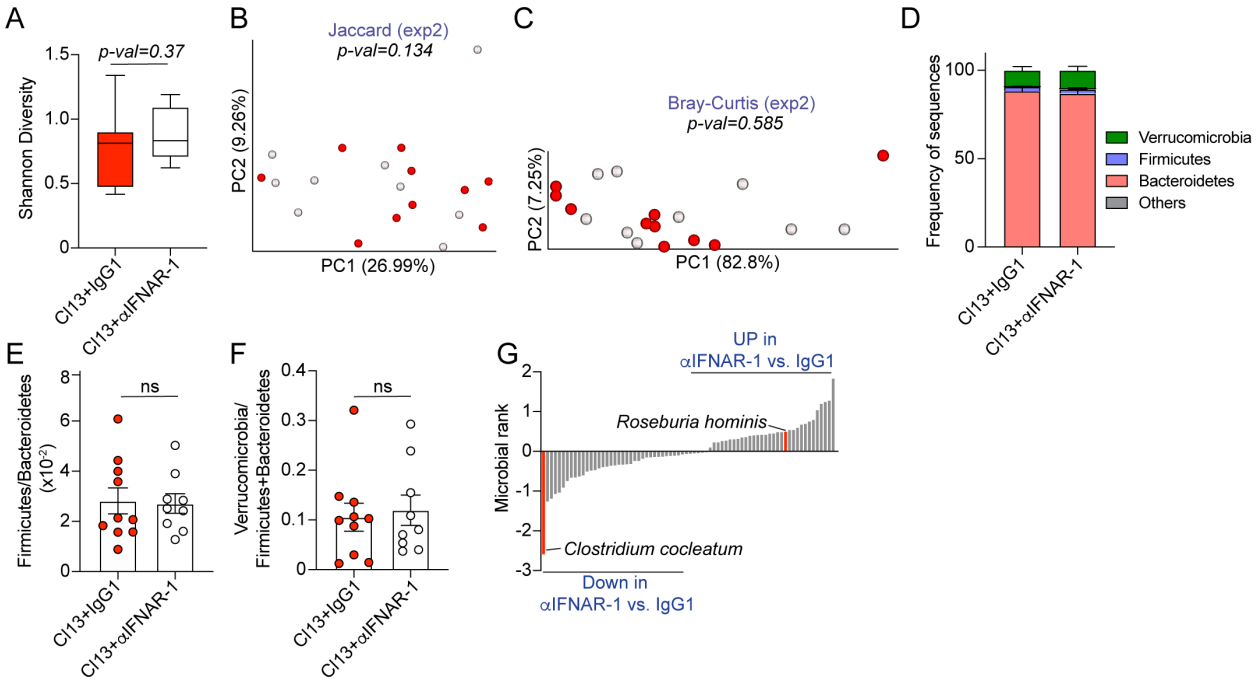

Figure 1-11. IFN-I signaling promotes overrepresentation of *Erysipelatoclostridium* and reduces *Roseburia* species in the intestinal microbiome after LCMV Cl13 infection. C57BL/6 mice were infected with LCMV Cl13 and injected with isotype (IgG1) or anti-IFNAR-1 Ab (αIFNAR) intraperitoneally (i.p.) and shotgun metagenomic sequencing was performed on colonic and caecal contents on day 9 p.i. (A) Alpha diversity by the Shannon diversity index. (B-C) Beta-diversity PCoA with Jaccard (B) and Bray Curtis (C) distances. (D) Frequency of sequences at the phylum level at indicated time-points. (E,F) Frequency of phylum Firmicutes divided by Bacteroidetes (E) or phylum Verrucomicrobia divided by Firmicutes and Bacteroidetes (F) for each individual mouse. (G) Songbird Multinomial Regression (MR) analysis of species in IgG1-treated vs. αIFNAR-treated Cl13-infected mice. X-axes correspond to individual taxa. The genera of the taxa highlighted in red were consistently perturbed, in the same direction and with rank cut-offs of -0.5 and 0.5, after 16S shotgun metagenomics analysis of an independent cohort of mice. Data are representative of one independent repeat by shotgun metagenomics with n=9-10 mice/group. (A,D-F) Averages ± min/max (A) or ± S.E.M. (D-F). (B-C) Significance was computed with PERMANOVA (999 permutations).

1.3.7 LCMV Cl13 infection enhances susceptibility to colitis induced by chemical or secondary pathogen insults

Barrier dysfunction precedes disease relapses in humans afflicted by Crohn's disease (107-109) and, in mouse models of immune-, chemically- and bacterially-induced colitis, increased solute flux consistent with the leak pathway promotes host morbidity (61, 110, 111). In addition, overrepresentation of *Erysipelatoclostridium* commensals and reductions in *Roseburia spp.* are associated with human IBD (112-114) and with the induction of intestinal leakage after Cl13 infection (Fig. 1-6).

To test the effects of chronic viral infection on host tolerance to chemically-induced colitis we performed a 10-day course of treatment with 2% dextran sulfate sodium (DSS) (115) between days 21 and 31 p.i. with Cl13, ARM and in uninfected mice. As expected with the low dose of DSS used (116), we did not observe any perceptible effects on the body weight of uninfected and ARM-infected treated mice compared to untreated controls (Fig. 1-12A). In contrast, Cl13-infected mice suffered reductions in body weight of 7% on average after 10 days of treatment, which was significantly lower from that of ARM-infected and uninfected treated mice (Fig. 1-12A), indicating that chronic viral infection with Cl13 conferred increased susceptibility to acute, chemically induced colitis.

We next evaluated the impact of Cl13 infection on host tolerance to bacterially-induced colitis with the rodent-borne enteropathogen *Citrobacter rodentium* (117). As expected, *C. rodentium* challenge caused mild weight loss and no effect in survival in the absence of LCMV co-infection (118) and similar effects were observed 10 days after *C. rodentium* was inoculated in mice previously infected with ARM (ARM+*C.rod*) (Fig. 1-12B). In contrast, we detected profound

body weight loss (up to 20% of initial weight) that preceded 100% mortality when *C. rodentium* was inoculated into Cl13-infected mice (Fig. 1-12B-C).

In summary, we found that viral persistence rendered Cl13-infected mice more susceptible to intestine-specific stressors, such as colitis induced by chemicals and bacteria, suggesting that chronic-infection-induced adaptations in the intestinal tract have implications for host tolerance to secondary enteric insults.

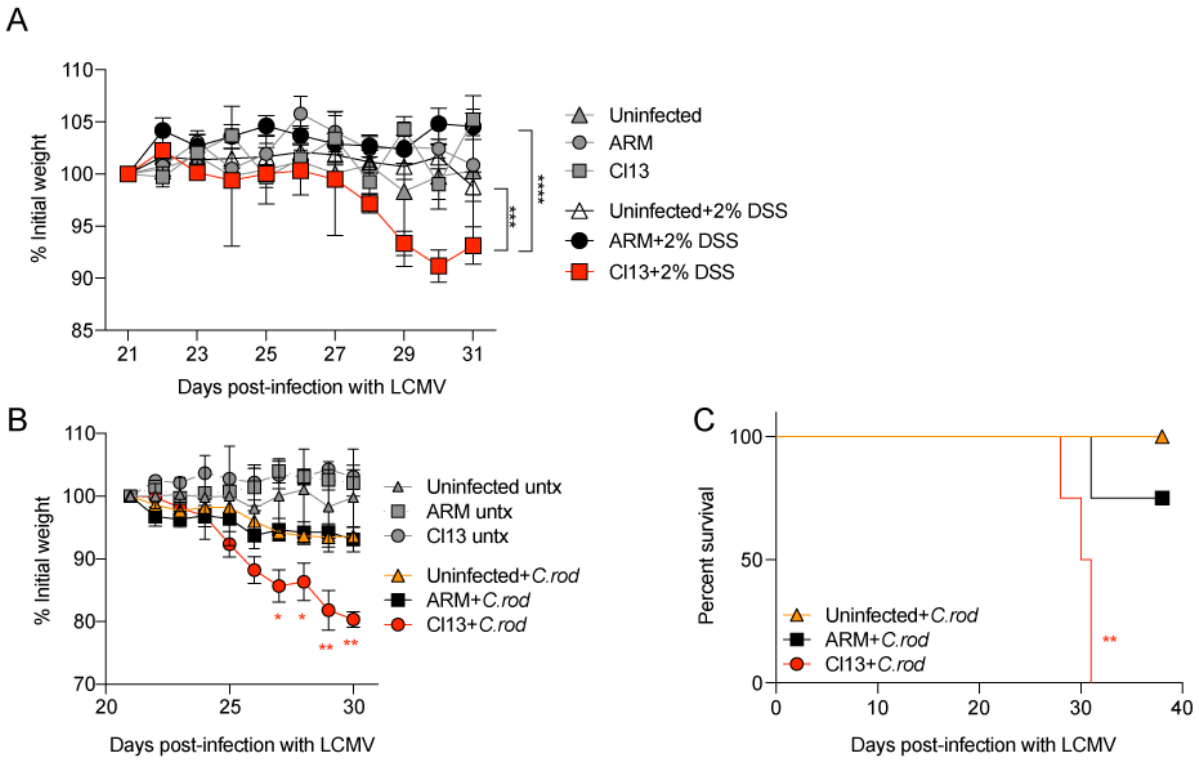

Figure 1-12. LCMV Cl13 infection enhances susceptibility to colitis induced by chemical or secondary pathogen insults. C57BL/6 mice were infected with LCMV Cl13, ARM or left uninfected. At days 21 or 30 p.i. mice were treated with 2% w/v DSS for 10 consecutive days (A) or intraorally infected with $3.5x10^9$ colony-forming units (c.f.u.) of *C. rodentium* (+*C.rod*), or left untreated (untx) (B-C). Percentage of initial body weight (A-B) and survival curves (C) are shown. Averages (C) or averages ± S.E.M. are shown (A,B). Data are (A) pooled from two and (B-C) representative of two independent experiment with n=3-5 mice/group. (A) One-way ANOVA with Tukey's multiple comparisons correction on day 31 p.i. (B) One-way ANOVA with Dunnett's multiple comparisons test with ARM+*C.rod* and Cl13+*C.rod* vs. Un+*C.rod* at every time-point p.i. (C) Log-rank Mantel-Cox survival test. *p-val<0.05, **p-val<0.01, ***p-val<0.001, ****p-val<0.0001.

1.4 Discussion

Intestinal barrier dysfunction constitutes a marker of disease progression during chronic viral infection, yet the mechanisms leading to an altered gut barrier in this context have not been causally defined. In this study, we found that, in contrast to its acute parental strain, the persistent LCMV variant Cl13 continuously replicated in hematopoietic and mesenchymal, but not epithelial, cells within the small intestine and caused long-term increase in intestinal paracellular permeability to small molecular weight molecules. Such intestinal barrier alteration associated

with IFN-I-mediated downregulation of genes encoding tight junction related proteins in IEC. IFN-I signaling also promoted cell cycle, glycolytic metabolism and inflammation-associated transcriptional pathways on IEC, including increased expression of $CXCR3^{+}$-effector-T-cell chemoattractants (i.e. *Cxcl9* and *Cxcl10*) in chronically infected mice. Importantly, IFN-I receptor blockade restricted CD8 T cell accumulation, effector functions and the abundance of $TCF\text{-}1^{lo}$ vs TCF^{hi} CD8 T cell subsets within the small intestine, and both IFN-I signaling blockade and CD8 T cell depletion prevented intestinal leakage after chronic infection. IFN-I also promoted *Erysipelatoclostridium* and *Roseburia* microbiome shifts. Finally, we found that long-term viral persistence and increased intestinal barrier permeability associated with enhanced susceptibility to chemical and bacterially induced colitis in the chronic infection setting.

Our study demonstrated that systemic inoculation with persistent, but not acute, LCMV isolates resulted in long-term viral replication in hematopoietic and mesenchymal, but not epithelial cells of the small intestine, that was sustained even after systemic viremia was resolved. Within the hematopoietic compartment, it is most likely that dendritic cells and macrophages, but not T cells or B cells, are targeted by LCMV in intestinal mucosa as these cells are productively infected by Arenaviruses in other tissues (119-122). On the other hand, the most likely targets among mesenchymal cells may include vimentin-expressing fibroblasts, myofibroblasts, pericytes and stromal stem cells (123, 124). Intriguingly, while LCMV and other Old World Arenaviruses productively infect human intestinal epithelial cell lines *in vitro* (125), we failed to detect viral proteins in IEC from LCMV Cl13-infected mice, despite high and persistent viral titers in intestinal mucosa. Thus, our study highlights important discrepancies between *in vitro* and *in vivo* LCMV infection and suggest that infection of intestinal epithelial cell lines may not necessarily reflect Arenavirus tropism *in vivo*.

As mentioned in the introduction, there are three described routes of solute transport across the intestinal epithelium; the pore, the leak and the unrestricted pathways (58). Given that the causative mechanisms and implications of each of these routes of solute transport can be different, it is important to identify the specific pathway that is altered in a given context. Claudin-2-mediated flux through the pore pathway, for instance, accelerated bacterial clearance (77), while flux via the MLCK-dependent leak pathway exacerbated disease (111) after *Citrobacter rodentium* infection. Our work revealed that chronic, but not acute, LCMV infection persistently enhanced intestinal barrier permeability, selectively increasing the flux of small molecular weight (~4 kDa) molecules, which is consistent with alteration of the leak pathway. We did not, however, detect increased leakage of bigger molecules (~40 kDa) or macroscopic epithelial layer disruption, indicating the absence of frank epithelial damage or ulceration and an intact unrestricted transport route in this setting. These results highlight chronic LCMV infection in mice as an additional model system to study the causative factors, implications and effects of potential drug therapies on the intestinal leak transport pathway in the context of persistent inflammation. It is important to note that, although the intestinal transport route that leads to increased microbial product translocation during other chronic infections has not yet been defined, previous studies documented the presence of enterobacterial DNA and bacterial lipopolysaccharide (LPS) in plasma from HIV-infected humans and SIV-infected rhesus macaques (69, 126). In addition, increased ratio of lactulose-to-mannitol in urine, which is indicative of enhanced paracellular solute transport (i.e. leak or pore pathway), were observed in humans infected with *Plasmodium falciparum* (66).

By performing transcriptomic analysis of IEC from acutely vs. chronically infected mice, we found that the aforementioned intestinal leakage associated with down-regulation of genes

encoding for tight junction related proteins. Among them, PATJ has been involved in the formation and polar distribution of tight junction complexes (127) while claudin-23 expression is significantly reduced in tumors vs. healthy intestines during colorectal cancer (128), whereby increased tight junction-dependent permeability associates with development of this disease (129). Claudin-3, on the other hand, is recruited to the tight junction (130) and its increased expression is associated with intestinal barrier maturation in neonate mice (131), while claudin-8 can limit Na^+ flux in kidney cell lines (132). Overall, down-regulation of genes encoding for PATJ, claudin-3 and claudin-23, which are involved in tight junction modulation (127-131), were consistent with alteration of the leak pathway after chronic LCMV infection. On the other hand, decreased claudin-8 transcript levels in IEC from chronically vs. acutely infected mice suggested that the pore pathway might also be altered after chronic LCMV infection.

Our study further identified an IFN-I transcriptional signature in IEC from chronically vs. acutely infected mice. Indeed, we found that signaling through IFNAR accounted for 34% of altered pathways and 37% of DEG in IEC from LCMV Cl13- vs. ARM-infected mice. IFN-I signaling not only down-regulated the aforementioned genes encoding for claudin-8 and claudin-23 but also inhibited a xenobiotic-related transcriptional signature. Interestingly, engagement of the xenobiotic receptor PXR prevented increase in intestinal permeability under homeostatic conditions (133). IFN-I signaling also promoted expression of cell cycle-related genes, consistent with enhanced IFN-I-mediated IEC proliferation previously reported during latent murine cytomegalovirus infection (134), and glycolysis-related metabolic signatures, which are characteristic of proliferating cells (135).

Importantly, we demonstrated that IFN-I signaling was essential for increasing intestinal permeability after chronic LCMV infection. In the same line, an association between IFN-I

signaling and barrier dysfunction has been previously established in chronic infections caused by HIV in humans and SIV in rhesus macaques (67, 68). In addition, SIV-infection of sooty mangabeys, a natural viral reservoir, does not induce a sustained IFN-I signature nor increases microbial product translocation into the systemic circulation (69, 70, 136, 137). These association studies led to the proposal that increased intestinal permeability allows translocation of microbial products, which in turn causes downstream IFN-I signaling and immune activation (69, 70). While our transcriptome data are consistent with the previously reported association between IFN-I and increased intestinal permeability during chronic viral infection, our IFN-I blocking experiments compellingly demonstrated that IFN-I can be a cause, and not necessarily a consequence, of intestinal leakage. On the other hand, IFN-I signaling was shown to preserve intestinal integrity during chemically-induced colitis (97, 138) and to accelerate wound healing via increasing IEC proliferation during latent viral infection (134). It is therefore conceivable that IFN-I may exert dual roles on the intestinal barrier, on the one hand promoting IEC proliferation to favor wound healing and opposing the unrestricted pathway, and, on the other hand, down-regulating tight junction-related proteins thereby increasing translocation of microbial products via the leak pathway. Importantly, our results do not demonstrate that IEC-intrinsic IFN-I signaling is required for the induction of intestinal leakage after chronic viral infection, and it is therefore possible that IFN-I may act indirectly, via other cell types, to increase intestinal permeability. Interestingly, a SNP predicted to be in the IFNAR1 gene was recently associated with humans afflicted by Crohn's disease (139), further supporting potential unappreciated roles for IFN-I in modulating intestinal barrier dysfunction.

We also demonstrated that IFN-I signaling promoted IEC expression of *Cxcl9* and *Cxcl10* whose products can contribute to the recruitment of CXCR3-expressing T cells to the intestine

(71). Consistently, IFN-I receptor blockade in chronically infected mice limited accumulation, effector features and the abundance of TCF-1^{low} populations of virus-specific CD8 T cells in the small intestines. This is in line with previous studies indicating that IFN-I signaling promotes clonal expansion and survival of CD8 T cells in secondary lymphoid organs, liver, brain and lung (140) as well as their IFNγ production (90, 141) and is consistent with its role in repressing the generation of TCF-1^{hi} virus-specific CD8 T cells (39) in the spleen. On the other hand, we observed that IFN-I limited (rather than promoting) accumulation of virus-specific-CD4 T cells in small intestines from chronically infected mice, which is consistent with the IFN-I inhibition of splenic CD4 T cell accumulation that was previously reported (89, 90).

Importantly, we also demonstrated that CD8 (but not CD4) T cell responses were essential to enhance intestinal leakiness after chronic LCMV infection. This is consistent with increased CD8 T cells observed in the intestinal mucosa of SIV-infected rhesus macaques (142, 143) and HIV-infected individuals (144, 145) as well as a positive correlation of perforin-expressing CD8 T cells with microbial translocation that was reported in acutely-HIV infected individuals (146). Causal evidence linking CD8 T cells and enhanced intestinal permeability, was, however, previously lacking. Instead, reduced numbers of intestinal Th17 CD4$^+$ T cells have been extensively proposed as the cause of barrier dysfunction in both SIV-infected RM and HIV-infected humans (67, 68). While our results do not contradict a potential role for reduced Th17 responses in causing microbial translocations during HIV or SIV infections, they raise the possibility that infiltrating CD8 T cells may also play an essential role. Our CD8-T-cell depletion experiments further demonstrated that increased viral loads or *Ifnb* levels are insufficient to increase intestinal permeability in the absence of CD8 T cells. This suggest that CD8 T cells act

downstream of IFN-I signaling and uncoupled to viral loads to induce intestinal leakage after chronic infection.

Furthermore, we uncovered a causal role for IFN-I in oppositely modulating the abundance of two intestinal Firmicute taxa (i.e. *Erysipelatoclostridium* and *Roseburia*) after chronic LCMV infection. Importantly, while the intestinal microbiome as a whole provides tonic IFN-I signals to innate immune cells and allows timely control of a chronic virus (147), a bi-directional relationship between IFN-I and microbiome composition had not been previously demonstrated in this context. Our rigorous analysis also provides a valuable resource that could guide future studies on the microbiome-immune system crosstalk during chronic viral infection.

Last but not least, our data indicated that chronic LCMV infection enhanced susceptibility to chemically- and *C. rodentium*-induced intestinal colitis, which associated with increased intestinal permeability via the leak pathway. It has previously been shown that increased solute flux consistent with the leak pathway promoted host morbidity in mouse models of immune-, chemically- and bacterially-induced colitis (61, 110, 111) and that barrier dysfunction preceded disease relapses in humans afflicted by Crohn's disease (107-109). Besides barrier dysfunction, factors such as diet, gut microbiome composition or pre-existing immune deficiencies can also confer susceptibility to experimental colitis (116, 148, 149). Along the same line, we found that the induction of intestinal leakage associated with increased abundance of *Erysipelatoclostridium* commensals and underrepresentation of *Roseburia spp.* in the intestinal microbiome, both of which are linked to IBD (112-114). Thus, while our data suggest a potential role for the enhanced intestinal leakage as a pro-morbidity factor in the context of colitis-inducing stressors in chronically infected mice, a role for other virus-induced intestinal adaptations in mediating this effect cannot be ruled out.

Overall, our findings propose a previously unrecognized causal role for IFN-I signaling in driving intestinal barrier leakage during chronic viral infection, which could be explained by tight junction dysregulation and enhanced intestinal CD8 T cell responses. Importantly, we also demonstrated an unappreciated essential role for CD8 T cells as causative factors of increased intestinal permeability and established an association between enhanced leak pathway, specific intestinal microbiome perturbations and susceptibility to colitis during chronic viral infection. These new mechanistic insights on intestinal barrier regulation might have implications for other chronic infections (66-68), inflammatory diseases (150) and/or certain cancers (151-153), where intestinal leakage has been reported.

1.5 Author contributions

L.L.-B. designed, performed, analyzed and interpreted all experiments, and wrote the manuscript. S.P.N. and J.R.T. provided feedback for interpreting data related to intestinal permeability and tight junction modulation after infection. G.H., T.S. and K.S. performed all pre-processing and 16S/shotgun metagenomic sequencing. A.S. assisted with experimental design of microbiome studies and provided guidance in -omics data analysis. R.K. supervised microbiome analysis and provided advice. E.I.Z. conceived and supervised the project, designed and interpreted experiments and wrote the manuscript. All listed authors revised the manuscript.

1.6 Acknowledgments

We thank members of the Zuniga laboratory for discussions and critical reading of the manuscript. We thank Dr Li-fan Lu, Dr. Chia-hao Lin for providing *Citrobacter rodentium* DBS100 and Dr. Manuela Raffatellu for protocol on how to prepare stocks. We thank Dr Gail Ackermann for data upload and metadata curation on Qiita. We thank personnel at the Animal Facility, IGM Genomics center sequencing core, Moore's Cancer Center Histopathology core and at the UCSD Microscopy core (NINDS NS047101).

Chapter 1, in full, will be submitted for publication as it appears. Lara Labarta-Bajo was the primary investigator and author of this paper. I would like to thank co-authors Dr. Steven P. Nilsen, Dr. Gregory Humphrey, Dr. Tara Schwartz, Dr. Karenina Sanders, Dr. Austin Swafford, Dr. Rob Knight, Dr. Jerrold R. Turner and Dr. Elina I Zúñiga for their contributions.

1.7 Materials and methods

Mice, infections and antibody treatments

Six to ten-week-old female C57BL/6 mice were purchased from The Jackson Laboratory and housed under specific-pathogen-free conditions. Mice were infected intravenously (i.v.) with $2x10^6$ plaque forming units (PFU) of LCMV ARM or Cl13. Viral stocks were grown, identified and quantified as reported previously (14). Viral loads were determined by standard plaque assay of serum or tissue homogenates (14). For CD8 and CD4 T cell depletion studies, mice were intraperitoneally (i.p.) injected with anti-CD8α (53-6.72, BioXcell), anti-CD4 (GK1.5, BioXcell) or IgG2a (2A3, BioXcell) antibodies on day -2, -1, and 5 p.i. (250 µg/mouse) as well as on the day of infection (200 µg/mouse). For IFNAR *in vivo* blockade, mice were i.p. injected with IFNAR neutralizing antibody (MAR1-5A3; BioXCell) or mouse IgG1 isotype control (MOPC-21; BioXcell) on days -1 and 0 p.i. (500 µg/mouse) as well as on days 2, 4 and 6 p.i. (250 µg/mouse) with Cl13 (89, 90). Uninfected control mice were treated alongside.

For secondary infection experiments, *Citrobacter rodentium* DBS100 obtained from Dr. Lifan Lu's laboratory (UCSD) was streaked out from a frozen stock on a Luria Broth (LB, Sigma) plate supplemented with nalidixic acid (Nal; 50µg/ml, Sigma) and incubated at 37^0C overnight (118). An individual colony was then inoculated into liquid LB+Nal media and grown overnight. Mice were infected with $4x10^9$ colony-forming units (CFU) intraorally (i.o.) (118).

For chemically induced colitis experiments, we supplemented mouse drinking water with 2% w/v dextran sulfate sodium (DSS, MP Biochemicals) and treated mice for 10 consecutive days.

Mice were maintained in a closed breeding facility at the Biomedical Sciences Building, UCSD, and housed in ventilated cages containing HEPA filters. Mouse handling conformed to the

requirements of the National Institutes of Health and the Institutional Animal Care and Use Guidelines of UCSD.

Histopathological analysis and immunofluorescence

For histopathological analysis, mice were sacrificed, tissues were harvested and placed in 10% formalin solution within 5min. Tissues remained in fixing solution for 24h, after which they were washed twice with deionized water and later placed in 70% ethanol. Tissue Technology Shared Resource at UCSD performed downstream paraffin embedding, sectioning, hematoxylin/eosin staining and histopathological evaluation of intestinal tissues.

For immunofluorescence analysis, mice were individually sacrificed and their intestines placed in optimal cutting temperature compound (OCT, Akura) within 5min. 10µm sections were cut, fixed in 4% paraformaldehyde for 10min, washed 3 times in 1x Phosphate Buffered Saline (PBS, Fischer), blocked for 1h in gelatin buffer (3% normal donkey serum, 40mg/ml BSA, 0.1% fishscale gelatin, 0.05% Tween20, 0.1% Triton-X-100 in PBS1x) plus Fc block and stained with primary Ab overnight in gelatin buffer. After 3 washes, sections were stained with DAPI. Sections were mounted and images were acquired with a Leica SP5 confocal microscope at the Microscopy Core at UCSD. Primary antibodies used: EpCAM-APC (clone G8.8, Thermo Fisher Scientific), CD45.2-FITC (clone 104, Biolegend), rabbit anti-Vimentin (clone D21H3, CST), guinea pig anti-LCMV polyclonal Ab (27). Secondary antibodies: goat anti-guinea pig-Rhodamine Red-X Fab (polyclonal AB_2632433, Jackson ImmunoResearch), AffiniPure F(ab')$_2$ fragment goat anti-rabbit-APC (polyclonal AB_2337987, Jackson ImmunoResearch).

In vivo intestinal permeability assay

Mice were water-deprived for 4h, followed by intraoral inoculation with Fluorescein isothiocyanate conjugated dextran 4 kDa (FD4, Sigma) or 40 kDa (FD40, Sigma) at 44mg/100g of body weight (75). 4h after, mice were bled, serum collected and stored at -80 ^{o}C for future quantification. Fluorescence at 488nm was determined with a plate reader (BMG Labtech). Background was subtracted using values from serum samples belonging to uninoculated mice. Absolute FD4 or FD40 amounts per ml of blood were determined via standard curve extrapolation.

Lymphocyte isolation from blood, spleen and small intestine

Spleens were harvested, digested for 20 min at 37 ^{o}C in 1mg/ml collagenase D (Roche) and mashed through a 100 μm filter. Cells were then centrifuged at 1500 rpm at 4^{0}C for 5 min. Red blood cells (RBC) were lysed by incubating pellets in 1ml of RBC-lysis buffer (150mM NH_4Cl, 10mM $KHCO_3$, 0.1mM Na_2EDTA in deionized water, at pH 7.4) for 4 min at room temperature (RT). After RBC lysis, 10ml of FACS buffer (PBS1x + 3%FBS) were added followed by centrifugation as stated above. Pellets were resuspended in 5ml of complete Roswell Park Memorial Institute (RPMI, Gibco), which consisted of RPMI supplemented with 10% heat-inactivated Fetal Bovine Serum (FBS, Atlanta Biologicals) , 2% Penicillin/Streptavidin (P/S, BioWhittaker), 1 mM Sodium Pyruvate (Na-pyr, Thermo Scientific), 1mM L-Glutamine (L-Gln, BioWhittaker), 20 mM HEPES (Thermo Scientific) and 55 mM beta-mercaptoethanol (Life Technologies). Absolute leukocyte numbers were determined via FSC/SSC gating in a Guava Easycyte automated cell counter (MilliporeSigma, MA).

Small intestines were harvested, cleaned from adipose tissue, flushed and macroscopically visible Peyer's Patches were excised. To isolate the epithelial layer, intestines were longitudinally and transversely cut into 1-2 cm pieces, placed in Pyrex conical flask containing a stirring magnet

and 30 mL of 'IEL buffer', and stirred on a stirring plate (Scilogex) set at 37 ºC for a total of 15 min. IEL buffer consisted of 1xPBS supplemented with 3% FBS, 2% P/S, 1mM Na-pyr, 20 mM HEPES and 10 mM Ethylenediaminetriacetic Acid (EDTA, Thermo Fisher Scientific). Soluble fraction was then collected, diluted in RPMI supplemented with 3% FBS and pelleted by centrifugation at 1500 rpm for 5min at 4^0C. Afterwards, to obtain lamina propria (LP), tissue pieces were minced and stirred at 37 ºC for 30min in 15 ml of 'LPL enzyme media' consisting of RPMI, supplemented with 3% FBS, 2% P/S, 1mM Na-pyr, 20mM HEPES, 0.4mg/ml Collagenase D (Roche) and DNAse I 10µg/ml (Roche). Suspension was then filtered through a 100 µm strainer and pelleted by brief centrifugation 1500 rpm for 5 min at 4^0C. Finally, epithelial or LP pellets were resuspended in 5 ml of '44% Percoll solution' and 2.5 ml of '67% Percoll solution' were added underneath with a Pasteur pipette. Tubes were then spun down at 2000 rpm (with no brake set) at RT for 20 min. Percoll solution was prepared by adding 1 part of 10X PBS (Gibco) to 9 parts of Percoll (GE Healthcare Biosciences) and further mixed with IEL buffer to obtain a 44% or 67% solution. The interphase layers containing IEL or LPL were collected after centrifugation, resuspended in 1ml of complete RPMI and leukocyte counts were determined with a Guava Easycyte (MilliporeSigma, MA) as indicated above.

Quantitative PCR

For quantification of transcripts in the small intestine: tissues were collected from sacrificed mice, snap frozen and stored at -80 °C. Later, tissues were thawed, bead-homogenized in RLT buffer (Qiagen) and centrifuged for 10 min at 10,000 rpm to pellet debris. Supernatants were used for total RNA extraction using RNeasy kits (Qiagen), digested with DNase I (RNase-free DNase set; Qiagen) and reverse-transcribed into cDNA using M-MLV RT (Promega). The

expression of various genes was quantified using Fast SYBR Green Master Mix (Thermo Fisher Scientific) or TaqMan Fast Universal PCR Master Mix with probe sets from the Universal Probe Library (Roche) in technical triplicates, followed by Real-Time PCR using a CFX96 Touch Detection System (Bio-Rad). Relative transcript levels were normalized against murine *Gapdh* or *Actb* as indicated. Graphs depicting qRT-PCR analysis of murine genes represent biological replicates of individual mice. SYBR Green Q-PCR primer sequences are the following: LCMV nucleoprotein F 5′-GCATTGTCTGGCTGTAGCTTA-3′, R 5′-CAATGACGTTGTACAAGCGC-3′; LCMV glycoprotein F 5'- CATTCACCTGGACTTTGTCAGACTC-3′ R 5′-GCAACTGCTGTGTTCCCGAAA-3′; *Actb* F 5'-AGGGAAATCGTGCGTGACAT-3', R 5'-GAACCGCTCGTTGCCAATAG-3'. Taqman Q-PCR primer sequences are the following: *Ifnb* F 5'-CTGGCTTCCATCATGAACAA-3', R 5'- AGAGGGGGTGGTGGAGAA-3'; Probe#18. *Gapdh* F 5'- TCCCACTCTTCCACCTTCGA, R 5'- AGTTGGGATAGGGCCTCTCTT-3', Probe#9.

Flow cytometry

Cells were stained at a maximal concentration of $2x10^8$ cells/ml in FACS buffer or as indicated below. For surface staining of splenocytes, IEL and LP cells were first stained with a fixable viability dye (Ghost dye, Tonbo) in 1xPBS for 10 min at 4 ^oC followed by staining with MHC-I tetramer H2-D^b/$GP_{33–41}$-BV421 provided by NIH Tetramer Core Facility (Atlanta, GA) in FACS buffer for 1h at RT followed by staining for 20min at 4^oC with remaining surface antibodies. Alternatively, cells already stained with the viability dye were stained with MHC-II tetramer I-A^b/GP_{67-77}-APC provided by NIH Tetramer Core Facility (Atlanta, GA) in FACS buffer for 2h at 37^0C followed by staining for 20min at 4^oC with antibodies against cell surface markers. For

intracellular staining after *ex vivo* peptide restimulation, cells were fixed in 1% paraformaldehyde (PFA) for 10min at RT and stained with antibodies in 1x perm/wash buffer (Thermo Scientific) for 30 min at 4 °C. Alternatively, for intranuclear staining, cells were fixed with the Foxp3 Transcription Factor Staining Buffer Set Kit (Thermo Scientific) per vendor's recommendation and stained with antibodies in 1x perm/wash buffer for 1h at RT. Antibodies used in this study were purchased from Thermo Fisher Scientific (Waltham, MA), BD Biosciences or Biolegend (San Diego, CA): CD8a BV786 or APC efluor 780 (53-6.7), CD4 BV650 or BV711 (RM4-5), PD-1 BV650 (29F.1A12), IFNγ APC (XMG1.2), TNFα FITC (MP6-XT22), IL-2 PE (JES6-5H4), KLRG1 PeCy7 or PE-TR (2F1), TIM3 PeCy7 (RMT3-23). Anti-TCF-1 (C63D9) conjugated with Alexa Fluor 647 or Alexa Fluor 488 was purchased from Cell Signaling Technologies (Danvers, MA). Cells were acquired using a Digital LSR II flow cytometer (Becton Dickinson, San Jose, CA) or a ZE5 Cell Analyzer (Bio-Rad, Hercules, CA). Flow cytometric data were analyzed with FlowJo software v9.9.6 and v10.

Ex vivo T cell stimulation

Small intestinal lamina propria lymphocytes were cultured at $2.5x10^6$ cells/ml in round-bottom 96-well plates for 5h in complete RPMI supplemented with Brefeldin A (1 □g/ml, Sigma), phorbol myristate acetate (PMA) (50 ng/ml, Sigma) combined with Ionomycin (1 μg/ml, Sigma), or with 1 μg/mL of the MHC class-I-restricted LCMV $NP_{396–404}$, $GP_{33–41}$, $GP_{276-286}$ and 10 μg/ml of the MHC class-II-restricted peptide GP_{67-77} (all >99% pure; Synpep). Cells were then stained with a fixable viability dye (Tonbo Ghost Dye) and surface staining with the anti-CD4 or anti-CD8 mAbs described above, fixed in 1% PFA, permeabilized and stained with the aforementioned antibodies against IFNγ, TNFα and IL-2 in 1x perm/wash buffer for 30 min at 4^0C. Unstimulated

controls in which cells were cultured without peptide or PMA/Ionomycin were performed in parallel and showed background levels of cytokine staining (data not shown).

IEC isolation, FACS purification and RNA extraction

We obtained the intestinal epithelial pellets by separating the epithelial layer in 'IEL buffer', as described above for lymphocyte isolation. Pellets were re-suspended and digested by stirring in 10ml of IEC enzyme media, which consisted of RPMI supplemented with 5% FBS, 1% P/S, 0.4 mg/ml Collagenase D (Roche), 0.3 U/ml Dispase (Roche) and 10 µg/ml DNaseI (Roche), for 20min at 37 ºC. Suspension was filtered through a 100µm strainer and spun down at 1500 rpm for 5 min at 4^0C. Three mice per group were pooled and stained with antibodies against EpCAM-APC (clone G8.8, Thermo Fisher Scientific) and CD45.2-FITC (clone 104, Biolegend) as well as Propidium Iodide (Sigma) before FACS-purification in FACSAria III (BD). 50,000 cells were sorted, washed with PBS1x, re-suspended in RLT (Qiagen) + beta-mercaptoethanol (10 □l/ml, Life Technologies) and stored at -80 ºC. The following day, RNA was extracted with RNAeasy Micro Kit (Qiagen) by following the manufacturer's protocol and re-suspended in molecular grade distilled H2O and stored at -80C until library preparation.

mRNA library preparation and RNA sequencing

Total RNA was extracted from 50,000 IEC and downstream processing was performed by the UCSD Institute for Genomic Medicine. mRNA stranded libraries were constructed by using TruSeq RNA Library Prep Kit v2 (Illumina) followed by single-end sequencing of 75 base-pair fragments with a HiSeq 4000 (Illumina). Raw sequencing files were processed with CASAVA 1.8.2 (Illumina) to generate .fastq files.

RNA sequencing processing and data analysis

Fastq files were uploaded onto the Galaxy project portal (https://usegalaxy.org/). We first obtained read quality reports by running the 'Fastqc' module (http://www.bioinformatics.babraham.ac.uk/projects/fastqc/), which gave us overall high-quality scores. Next, we used Spliced Transcripts Alignment to a Reference (STAR) (154) to align RNA-seq reads to the mouse genome with the following parameters: mm10, GRCm38, 75bp length of the genomic sequence around annotated junctions and STAR Galaxy version 2.7.2b default parameters for seed, alignment, limits and chimeric alignment. To assemble RNA-seq alignments into potential transcripts and to obtain gene abundance estimation files, we used StringTie (155) with mouse .gtf file (https://www.gencodegenes.org/mouse/) as reference to guide assembly. Default parameters were used with Minimum isoform fraction: 0.15, Minimum anchor length for junctions:10, Minimum junction coverage: 1, Minimum bundle reads per bp coverage to consider for assembly: 2, Gap between read mappings triggering a new bundle: 50, Fraction of bundle allowed to be covered by multi-hit reads: 0.95, trimming of predicted transcripts based on coverage: disabled, multi-mapping correction: disabled. Next, differentially expressed features were determined by DESeq2 (156). We defined differentially expressed genes (DEG) by false discovery rate (FDR)-adjusted p.value<0.05 and fold-change ≥2 throughout the manuscript. Gene Set Enrichment Analysis (GSEA) was performed through the software version 4.0.3 (76). We defined differentially enriched pathways with p.value<0.05 and FDR<0.25 cut-offs.

DNA extraction for 16S rRNA V4 amplicon sequencing and shotgun metagenomic sequencing

We followed the protocol described in (157). Briefly, to extract DNA from colonic and caecal contents, frozen samples were thawed and transferred into 96-well plates containing garnet beads. DNA was extracted using Qiagen PowerSoil DNA kit adapted for magnetic bead purification and eluted in 100 µL of Qiagen elution buffer. DNA quantification was performed via Quant-iT PicoGreen Assay (Invitrogen).

Library generation and sequencing

Sequencing was done following standard protocols from the Earth Microbiome Project (158, 159). Extracted DNA was amplified by using barcoded primers. Each sample was PCR-amplified in triplicate and V4 pair-end sequencing or whole-genome sequencing using a miniaturized version of the KAPA HyperPlus kit was performed using Illumina MiSeq or HiSeq (La Jolla, CA).

16S rRNA gene amplicon data analysis

All 16S rRNA gene amplicon data are publicly available on Qiita (https://qiita.ucsd.edu/) (160) under study ID 11043. Processing of our 16S rRNA raw data involved splitting of FASTQ libraries, demultiplexing, trimming of sequences to 150bp of length (161) followed by deblur 1.1.0 (162) with Qiita default parameters as follows: indel probability of 0.01, mean per nucleotide error rate of 0.005, minimum per-sample read threshold of 2, Greengenes_13.8 as reference phylogeny for SEPP and 1 thread per sample). Features with a minimum frequency of 10 were retained and reference hit table obtained was rarefied to 10,000 counts, which was in the plateau region of alpha-rarefaction curves (163). To assign taxonomy, we used the pre-fitted sklearn-based taxonomy classifier (‘classify_sklearn’) with the Green Genes classifier (gg-13-8-99-515-806-nb-

classifier) (164, 165). Beta-diversity was computed with the 'beta_phylogenetic' module using Unweighted UniFrac. This was followed by principal coordinate analysis ('pcoa' module) and significance was calculated for 'infection' with the 'beta_group_significance' module using PERMANOVA test with 999 permutations. Alpha diversity was computed using the 'alpha' module for Shannon Diversity Index. All the aforementioned analyses were done with Qiita platform version 052020 5f09f46.

To identify differentially abundant genera among groups, we collapsed our rarefied .biom tables to the genus level and used Songbird multinomial regression analysis (106) with default parameters (epochs of 10000, differential prior of 0.5) (https://github.com/biocore/songbird). We applied cut-off rank values of 0.5 and -0.5 to focus our analysis on moderately to highly perturbed genera. Validation of the model was performed for all analyses with tensor board.

Shotgun metagenomic data analysis

All shotgun metagenomic data are publicly available on Qiita (https://qiita.ucsd.edu/) (160) under study ID 11043. To pre-process these data we performed adapter trimming with Atropos v1.1.15 (166), followed by quality control filtering (QC_Filter) to bowtie2/Mus_musculus, followed by genome alignment of adapter-trimmed files with bowtie2 (with Rep94 database) (167) by running SHOGUN 0.1.5.(168) via Qiita (160). A table in .biom format with taxonomic predictions at the species level was then rarefied to a depth of 200,000 or 450,000 counts. Alpha-diversity was computed using the Shannon Diversity Index, as above, while beta-diversity was computed with the 'beta' module using Jaccard and Bray-Curtis metrics. PCoA representation and PERMANOVA were calculated as for the 16S rRNA gene amplicon data. To identify differentially abundant species between groups, we collapsed our rarefied .biom tables to the species level and

used Songbird multinomial regression analysis (106) with parameters described above for 16S rRNA gene amplicon data analysis.

Statistical analysis

Unpaired two-tailed t-Student test was used to compare two groups. If variances were not equal by F-test, data were tested using the non-parametric Mann Whitney-U test. Significant differences among more than two groups were determined based on one-way ANOVA with Tukey's multiple comparison correction or, in the case of unequal variances, non-parametric Kruskal-Wallis test with Dunn's multiple comparison correction. Statistical tests were performed using GraphPad Prism v8.

Chapter 2: CD8 T cells drive anorexia, dysbiosis and blooms of a commensal with immunosuppressive potential after viral infection

2.1 Summary

Infections elicit immune adaptations to enable pathogen resistance and/or tolerance and are associated with compositional shifts of the intestinal microbiome. However, a comprehensive understanding of how infections with pathogens that exhibit distinct capability to spread and/or persist differentially change the microbiome, the underlying mechanisms and the relative contribution of individual commensal species to immune cell adaptations is still lacking. Here, we discovered that mouse infection with a fast-spreading and persistent (but not a slow-spreading acute) isolate of lymphocytic choriomeningitis virus induced large-scale microbiome shifts characterized by increased Verrucomicrobia and reduced Firmicute/Bacteroidetes ratio. Remarkably, the most profound microbiome changes occurred transiently after infection with the fast-spreading persistent isolate, were uncoupled from sustained viral loads and were instead largely caused by CD8 T cell responses and/or CD8-T-cell-induced anorexia. Among the taxa enriched by infection with the fast-spreading virus, *Akkermansia muciniphila*, broadly regarded as a beneficial commensal, bloomed upon starvation and in a CD8-T-cell-dependent manner. Strikingly, oral administration of *Akkermansia muciniphila* suppressed selected effector features of CD8 T cells in the context of both infections. Our findings define unique microbiome differences after chronic versus acute viral infections and identify CD8 T cell responses and downstream anorexia as driver mechanisms of microbial dysbiosis after infection with a fast-spreading virus. Our data also highlight potential context-dependent effects of probiotics and suggest a model in which changes in host behavior and downstream microbiome dysbiosis may

constitute a previously unrecognized negative feedback loop that contributes to CD8 T cell adaptations after infections with fast-spreading and/or persistent pathogens.

2.2 Introduction

Adaptability, the capacity to adjust or adapt to improve fitness in the face of environmental changes is a trait shared among all forms of life (169). Such adaptations occur at the single cell, organismal and population levels and involve mechanisms with different time requirements to be implemented and exhibiting distinct degree of reversibility (169). Mammalian hosts and their immune systems often adapt to the presence of pathogens and engage different coping mechanisms depending on their virulence (170). In this regard, infections with fast-spreading and/or persistent pathogens elicit potent inflammatory responses that contribute to pathogen control, but can also undermine host survival, if unrestrained (1, 6, 170-172). Immune adaptations that attenuate the magnitude or amplitude of anti-pathogen responses are therefore necessary to allow pathogen clearance during acute infections, and/or partial pathogen control during chronic infections, while avoiding host death due to excessive immunopathology. Such adaptations encompass the innate and adaptive immune system, involve multiple layers of cell-intrinsic transcriptional, epigenetic, post-transcriptional and metabolic regulation, and are triggered in response to environmental changes (e.g. abundant pathogen associated molecular patterns and antigens, an inflammatory milieu, and altered nutrient and oxygen levels) (6, 19). Among the most studied adaptations that attenuate immune responses, CD8 T cell exhaustion, a unique cellular state characterized by diminished effector functions and expression of inhibitory receptors, is highly conserved not only among persistent infections in mice and humans, but also in tumor settings (19).

More recently, it has become evident that the character and strength of immune responses can be regulated by the microbiome (173). In particular for chronic pathogens, the intestinal microbiome has been shown to regulate host resistance to infections caused by persistent LCMV (147), *Plasmodium yoelii* (174) and *Mycobacterium tuberculosis* (175, 176). It has also been

shown that persistent pathogens such as HIV (177), Hepatitis C virus (HCV) (178) and Hepatitis B virus (HBV) (179) in humans as well as Simian Immunodeficiency Virus (SIV) (180) in macaques and *Plasmodium* species (181, 182) in mice induce significant changes in the intestinal microbiome composition or dysbiosis. On the other hand, acute infections caused by respiratory viruses (183-185) or enteropathogenic bacteria (186, 187) can also alter the composition of the gut microbiome. Notably, some of these studies have drawn a number of correlations between specific bacterial taxa and diverse disease parameters (177-179) that suggest important roles for the microbiome changes after infections. Studies addressing the mechanisms that dictate dysbiosis and/or the functional effects of specific taxa are, however, scarce.

In the present study, we use the well-established LCMV mouse model system to compare side-by-side microbiome changes induced at different times after infection with a fast-replicating persistent vs. a slow-replicating acute isolate. We found that the most profound microbiome alterations occurred after infection with the persistent, but not acute, LCMV isolate and were mostly transient (i.e. at day 8 but not at day 20 p.i) despite continuously high viral titers at the latter time-point. The microbiome changes unique to the infection with the fast-replicating persistent virus involved transiently increased Verrucomicrobia and reduced Firmicute/Bacteroidetes ratio at the phylum level as well as overrepresentation of *Akkermansia*, *Bacteroides* and *Sutterella* among other taxa. We also detected reductions in *Lactobacillus* and *Turicibacter*, the latter of which was maintained at day 20 p.i. Intriguingly, CD8 T-cells were responsible for modulating over half of the dysbiotic taxa after infection with the fast-replicating persistent LCMV isolate, thus revealing a novel key role for CD8 T cells in promoting intestinal dysbiosis. Coincidently, and only early after infection with the fast-replicating persistent isolate, CD8 T cells induced a profound anorexic behavior and a significant fraction of the taxa uniquely changed after this infection were commonly altered in

other fasting conditions. Among these fasting-associated taxa, we validated (at the species level) that the commensal *Akkermansia muciniphila* bloomed after infection with the fast-replicating persistent LCMV, and its abundance was remarkably increased by lack of food consumption in the absence of infection. We further observed a significant decrease in the levels of *A. muciniphila* in infected mice in which anorexia was reverted via CD8 T cell depletion. These observations supported the conclusion that anorexia induction was one of the means via which CD8 T cells caused intestinal dysbiosis after infection with persistent, fast-replicating, LCMV. On the other hand, experimental enrichment of *A. muciniphila* after LCMV infection suppressed Granzyme B (GrzB) and T-BET expression, and H3K27 trimethylation in distal virus-specific CD8 T cells. Together, these data contrast the specific microbiome changes that occur after infection with two closely-related viral isolates, uncoupling dysbiosis from sustained viral loads and instead relating it to both CD8 T cell responses and downstream anorexia occurring during the early phase of infection with a fast-replicating, persistent, virus. In addition, our data support a novel potential role for a CD8-T-cell-driven, fasting-associated commensal, *A. muciniphila,* in regulating CD8 T cells and attenuating selected aspects of their effector responses.

2.3 Results

2.3.1 Infection with a fast-spreading persistent LCMV isolate induced profound intestinal dysbiosis that was mostly transient and uncoupled from sustained viral loads

To investigate side-by-side alterations in intestinal microbiome composition after infection with a fast-replicating persistent vs. a slow-replicating acute virus, we performed 16S rRNA gene amplicon sequencing of caecal and colonic contents from mice infected with two closely-related LCMV isolates: Armstrong53b (ARM), which spreads more slowly and is cleared in a week, and clone13 (Cl13), which is fast-spreading and capable of persisting in C57BL/6 mice (15, 172). Two independent repeats with uninfected, ARM- and Cl13- infected mice (10 mice/group) were performed at days 8 and 20 p.i. Sampling of caecal and colonic contents was chosen over stool pellets, as it allows detection of taxa abundant inside the large intestine, which may not necessarily be eliminated in stools (104, 188). Alpha diversity determined by the Shannon diversity index, which combines richness and evenness (105), was selectively decreased upon Cl13 infection at day 8, but not at day 20 p.i. (Fig. 2-1A). We next identified specific differences in microbial composition by computing beta-diversity using the phylogenetic unweighted UniFrac metric or non-phylogenetic Jaccard and Bray-Curtis indexes followed by principal coordinates analysis (PCoA). Although ARM-infected and uninfected mice appeared to be significantly distant by permutational ANOVA (PERMANOVA) analysis with at least two of the aforementioned metrics on day 8 and 20 p.i. (Fig. 2-2A-C), there was no clear separation by any of the three main principal coordinates (PC) at the two time points studied (Fig. 2-1B and Fig.2-2D-F). On the other hand, the intestinal microbiome from day-8-Cl13-infected mice formed a prominent cluster by PC1 and/or 2 (Fig. 2-1B left & 2-2E&F left top) which was significantly distant from both uninfected and ARM-infected mice (Fig. 2-2A-C). No separation was observed along PC3 (Fig. 2-2D-F left

bottom). Remarkably, despite sustained viral loads in circulation and intestinal tissues (16, 72), at day 20 p.i. the microbiome of Cl13-infected mice segregated closer (Fig. 2-1B &2-2D-F right), albeit still significantly different (Fig. 2-2A-C), to the samples from uninfected or ARM-infected mice. Note that in all cases the PCoA clustering was consistent in different cages (Fig. 2-2G) and could not be explained by reproducible differences in dispersion (Fig. 2-2A-C, PERMDISP).

Importantly, when analyzing bacterial phylum composition at day 8 p.i., we detected profound reduction of the Firmicutes-to-Bacteroidetes ratio (Fig. 2-1C-D), concomitant with increases in the relative abundance of phylum Verrucomicrobia over Firmicutes and Bacteroidetes in Cl13-infected vs uninfected mice (Fig. 2-1C&E) that were specific for Cl13-infected mice. In contrast, alterations in the Firmicutes-to-Bacteroidetes ratio or phylum-level changes in Verrucomicrobia were not detected upon ARM infection (Fig. 2-1C-E) and were not maintained at day 20 after Cl13 infection (Fig. 2-1C-E). We next performed multinomial regression (MR) analysis with Songbird (106), with cut-offs at rank values of 1 and -1, to identify the most perturbed taxa at days 8 and 20 after the different infections. We restricted our analysis to taxa that were reproducibly perturbed in both independent experimental repeats. With these rigorous criteria, we defined biomarkers for each infection type and time point as taxa that were highly and reproducibly perturbed vs. uninfected controls processed in parallel. We identified 8 biomarkers at day 8 after Cl13 infection, and 2 different ones at the same time point after ARM infection (Fig. 2-1F and Dataset 2-1&2-2). Dysbiosis in day-8-Cl13-infected mice was characterized by reductions in the relative abundance of *Lactobacillus* and *Turicibacter* as well as enrichment of *Bacteroides*, *Sutterella, Akkermansia*, and *Erysipelatoclostridium* (i.e. *Clostridium* within the *Erysipelotrichaceae* family), among others (Fig. 2-1F and Dataset S2-1). In contrast, ARM infection promoted increases of unclassified genera within the *Peptostreptococcaceae* family,

while decreasing genera within the *Clostridiaceae* family (Fig. 2-1F and Dataset S2-2). By day 20 p.i., a total of 5 taxa were selectively perturbed by Cl13 infection while no genus was highly affected in ARM-infected mice (Fig. 2-1G and Dataset S2-3,2-4). This late dysbiosis in day-20-Cl13 infected mice included decreased relative abundance of *Turicibacter* and unclassified genera within the *Clostridiaceae* family concomitant with overrepresentation of unclassified genera within the *Erysipelotrichaceae* and *Ruminococcaceae* families, and *Clostridium* (*Clostridiaceae* family) (Fig. 2-1G and Dataset S2-3). Intriguingly, only *Turicibacter* was persistently altered in the same direction during both the early and the chronic phase of Cl13 infection (Fig. 2-1H). It should be noted that it is possible that the highly stringent criteria that we have chosen to identify the most reliable infection biomarkers have left out taxa that might still be biologically significant, such as *Roseburia,* which was reduced at day 8 and 20 p.i. in one experiment (rank day 8 p.i. -2.66; rank day 20 p.i. -1.53) (Dataset S2-1&2-3) but could not be validated in the second repeat, likely due to very low basal amounts of this taxon in uninfected controls from different cohorts (e.g. 0.29% ± 0.25 in cohort 1; 0.07% ± 0.12 in cohort 2).

Overall, these data are the first defining specific intestinal microbiome perturbations occurring after infection with two closely related viral isolates that exhibit contrasting capability to spread and persist, revealing that: i) infection with a fast-spreading persistent virus caused large-scale microbial dysbiosis that did not occur upon infection with a closely-related slow-spreading acute virus, ii) the most dramatic microbiome alterations after chronic infection were uncoupled from sustained pathogen loads and, instead, occurred transiently during the early phase of the infection, iii) transient microbiome alterations early after infection with the fast-spreading persistent virus were characterized by reduced Firmicutes-to-Bacteroidetes ratios (e.g. increased *Bacteroides* as well as reduced *Lactobacillus* and *Turicibacter*) and increased Verrucomicrobia

(i.e. *Akkermansia),* and iv) reductions in *Turicibacter* were sustained during the chronic phase of infection.

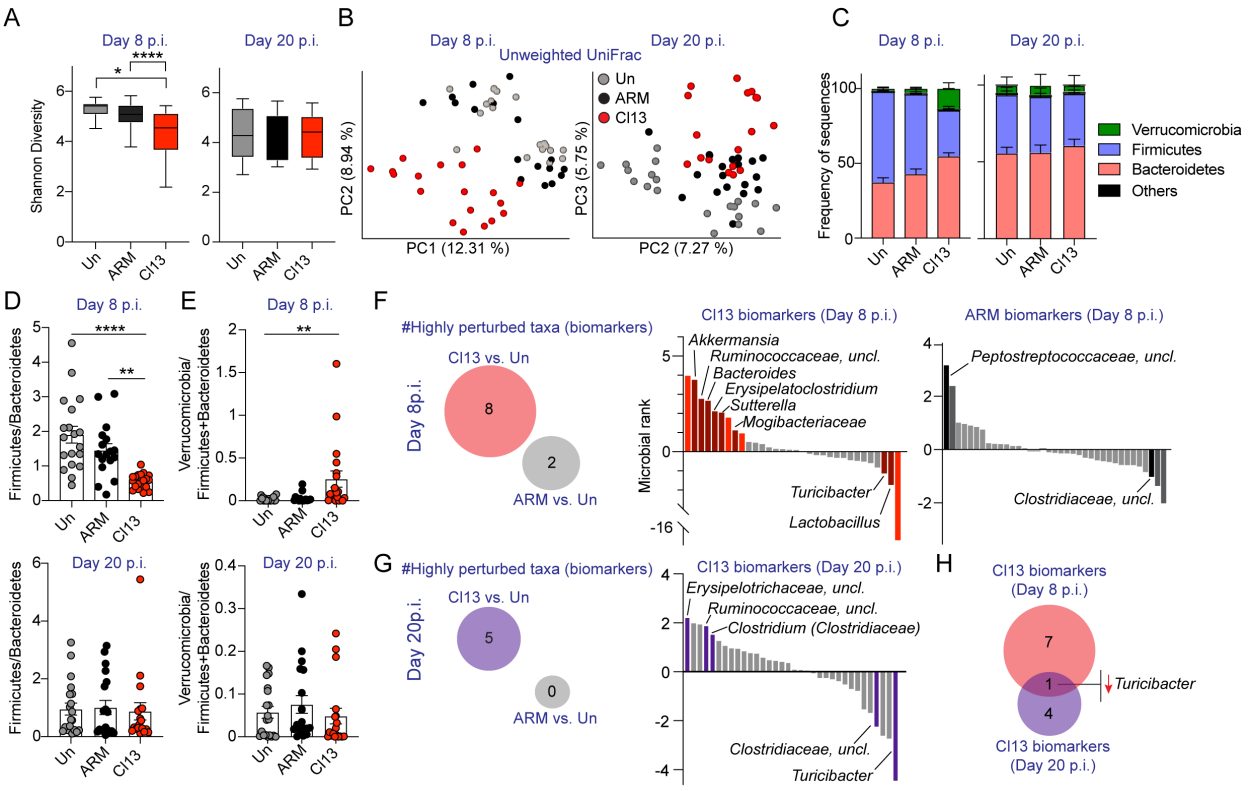

Figure 2-1. LCMV Cl13 infection induced intestinal dysbiosis that was mostly transient, uncoupled from viral loads and characterized by reduced Firmicutes-to-Bacteroidetes ratio and increased Verrucomicrobia. C57BL/6 mice were infected with LCMV ARM, Cl13 or left uninfected (Un) and 16S rRNA gene amplicon sequencing was performed on colonic and caecal contents from days 8 and 20 (p.i.). (A) Alpha-diversity by the Shannon diversity index at indicated time-points. (B) Beta-diversity PCoA with unweighted Unifrac distance at indicated time-points. PC1 was omitted for PCoA from the day 20 p.i. time point as it captured the basal differences of the cohorts used in the two experiments, rather than infection type. (C) Frequency of sequences at the phylum level at indicated time-points. (D,E) Frequency of phylum Firmicutes divided by Bacteroidetes (D) or Verrucomicrobia divided by Firmicutes and Bacteroidetes (E) for each individual mouse at indicated time-points. (F&G) Songbird multinomial regression (MR) analysis of genera in mice infected with ARM or Cl13 vs. Un on day 8 p.i. (F) or day 20 p.i. (G). Taxa with microbial ranks higher than 1 or lower than -1 in two independent repeats are considered highly perturbed (i.e. biomarkers). Left: Total number of genera highly perturbed by Cl13 or ARM infections. Right: X-axes correspond to individual taxa, taxa highly perturbed are indicated by text and colored in red (F) or violet (G) for Cl13 infection and black (F) for ARM infection. (H) Venn diagram overlapping biomarkers identified in F&G for day 8 (red) and day 20 (violet) after Cl13 infection. (A,C,D) Graphs show averages plus min and max (A) or ± standard error of the mean (S.E.M.) (C-E). (A-E) Data are represented by pooling n=8-10 mice/group from two independent experiments. (F-H) Data are representative of two independent experimental repeats. (A) Pairwise Kruskal-Wallis with false discovery rate (FDR) (Benjamini & Hochberg) correction. (D,E) Kruskal-Wallis with Dunn's correction; *p-val<0.05, **<0.01, ****<0.0001.

A

	PERMANOVA				PERMDISP			
	Day 8p.i.		Day 20p.i.		Day 8p.i.		Day 20p.i.	
Unweighted UniFrac	Exp1	Exp2	Exp1	Exp2	Exp1	Exp2	Exp1	Exp2
Un vs. ARM (q-val)	0.002	0.001	0.007	0.001	0.54	0.264	0.524	0.117
Un vs. Cl13 (q-val)	0.002	0.001	0.003	0.001	0.96	0.162	0.524	0.856
Cl13 vs. ARM (q-val)	0.002	0.001	0.003	0.001	0.54	0.162	0.524	0.119

	R-square values			
	Day 8p.i.		Day 20p.i.	
Factor	Exp1	Exp2	Exp1	Exp2
Infection status	0.2	0.219	0.195	0.234

B

	PERMANOVA				PERMDISP			
	Day 8p.i.		Day 20p.i.		Day 8p.i.		Day 20p.i.	
Bray-Curtis dissimilarity	Exp1	Exp2	Exp1	Exp2	Exp1	Exp2	Exp1	Exp2
Un vs. ARM (q-val)	0.085	0.029	0.023	0.002	0.559	0.321	0.876	0.603
Un vs. Cl13 (q-val)	0.002	0.002	0.015	0.002	0.559	0.033	0.876	0.426
Cl13 vs. ARM (q-val)	0.002	0.002	0.003	0.002	0.684	0.105	0.876	0.533

	R-square values			
	Day 8p.i.		Day 20p.i.	
Factor	Exp1	Exp2	Exp1	Exp2
Infection status	0.254	0.249	0.184	0.274

C

	PERMANOVA				PERMDISP			
	Day 8p.i.		Day 20p.i.		Day 8p.i.		Day 20p.i.	
Jaccard similarity index	Exp1	Exp2	Exp1	Exp2	Exp1	Exp2	Exp1	Exp2
Un vs. ARM (q-val)	0.001	0.001	0.001	0.001	0.715	0.825	0.612	0.006
Un vs. Cl13 (q-val)	0.001	0.001	0.001	0.001	0.715	0.185	0.612	0.9
Cl13 vs. ARM (q-val)	0.001	0.001	0.001	0.001	0.715	0.033	0.689	0.069

	R-square values			
	Day 8p.i.		Day 20p.i.	
Factor	Exp1	Exp2	Exp1	Exp2
Infection status	0.185	0.198	0.203	0.206

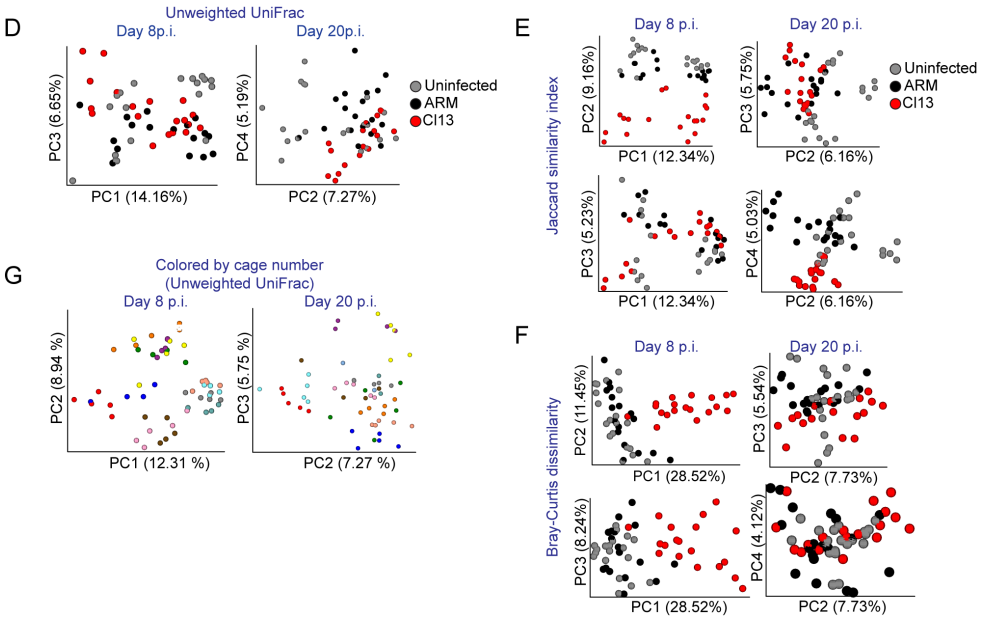

Figure 2-2. Intestinal microbiomes of ARM infected and Cl13-infected mice (but not mice housed in different cages) formed significantly distant clusters compared to uninfected mice. Related to Figure 1. C57BL/6 mice were infected with LCMV ARM, Cl13 or left uninfected (Un) and 16S rRNA gene amplicon sequencing was performed on colonic and caecal contents on day 8 and 20 p.i. (A-C) Beta-diversity with unweighted UniFrac distance (A), Bray-Curtis dissimilarity (B) or Jaccard similarity index (C) followed by beta group significance were calculated with PERMANOVA (999 permutations) for each experimental repeat (Exp1&Exp2). Differences in dispersion were calculated with PERMDISP (999 permutations). Q-values (q-val) were adjusted for multiple tests with the false discovery rate (Benjamini & Hochberg) correction. R-square values were computed with Adonis PERMANOVA (999 permutations). (D,G) PCoA plot generated with unweighted UniFrac distances and comparing PC1 vs PC3 (left) and PC2 vs PC4 (right) (D) or with each color representing individual cages (G). (E,F) PCoA plots comparing PC1,2 & 3 (left) or PC2, 3 and 4 (right) generated with Jaccard (E) or Bray-Curtis (F) metrics. Data represent individual experimental repeats (A-C) or are pooled from two experiments with n=8-10 mice/group (D-G).

2.3.2 CD8 T cells drove great part of the intestinal dysbiosis identified after infection with LCMV Cl13

Given that microbial dysbiosis coincided with peak CD8 T cell responses at day 8 p.i. (16), we next investigated the role of CD8 T cells in driving the microbiome changes uniquely identified after LCMV Cl13 infection. For that, we performed two independent experiments shown in Fig. 2-3 and 2-4, respectively, where we treated 10 Cl13-infected mice per group with anti-CD8 or isotype control antibodies, followed by shotgun metagenomics sequencing of caecal and colonic contents at day 8 p.i. As expected, treatment with anti-CD8 antibody significantly reduced the number of total and virus-specific CD8 T cells (Fig. 2-4A). Remarkably, Cl13-infected mice treated with anti-CD8 depleting antibodies formed a distinct cluster via beta-diversity PCoA when compared to their isotype-treated counterparts (Fig. 2-3A, Fig. 2-4B). This treatment also increased gut microbial alpha-diversity in one out of the two independent experiments (Fig. 2-3B, 2-4C), which, as described above (Fig. 2-1A), was selectively reduced at day 8 after Cl13 but not ARM infection. We also detected overrepresentation of Firmicutes upon CD8 T cell depletion (Fig. 2-3C, 2-4D), which explained an elevation of the Firmicutes-to-Bacteroidetes ratio (Fig. 2-3D, 2-4E) towards the value described above for uninfected and ARM-infected mice (Fig. 2-1D). As shown in Fig. 2-3E, 2-4F, blue bars, and Dataset S2-5, subsequent MR analysis with Songbird and with rank cut-offs of 0.5 and -0.5, to include moderately to highly perturbed taxa, indicated that treatment with anti-CD8 antibodies reverted the changes of commensal species belonging to 3 of the most increased (i.e. *Bacteroides, Akkermansia* and *Erysipelatoclostridium*) and 2 of the most decreased (i.e. *Lactobacillus* and *Turicibacter*) genera described above as biomarkers for day-8 Cl13 infected mice (Fig. 2-1F). Overall, CD8 T cells modulated (in a moderate and/or high degree) the abundance of 63% of the biomarkers selectively altered upon Cl13 infection (Fig. 2-

3F and 2-1F) including *Turicibacter*, which was underrepresented at both day 8 and 20 after Cl13 infection (Fig. 2-1H).

These data indicated that, despite their exhausted state (16, 25, 189), CD8 T cells are responsible for great part of the dysbiosis observed after infection with a fast-spreading persistent virus. Specifically, CD8 T cells were, at least partially, responsible for the transient reduction in Firmicutes-to-Bacteroidetes ratio (i.e. enriching *Bacteroides* and *Erysipelatoclostridium* while reducing *Lactobacillus* and *Turicibacter*), as well as for the overrepresentation of *Akkermansia*. These findings situate CD8 T cells as novel and key drivers of the microbial changes that take place early after infection with a virus capable of spreading quickly and/or establishing persistence.

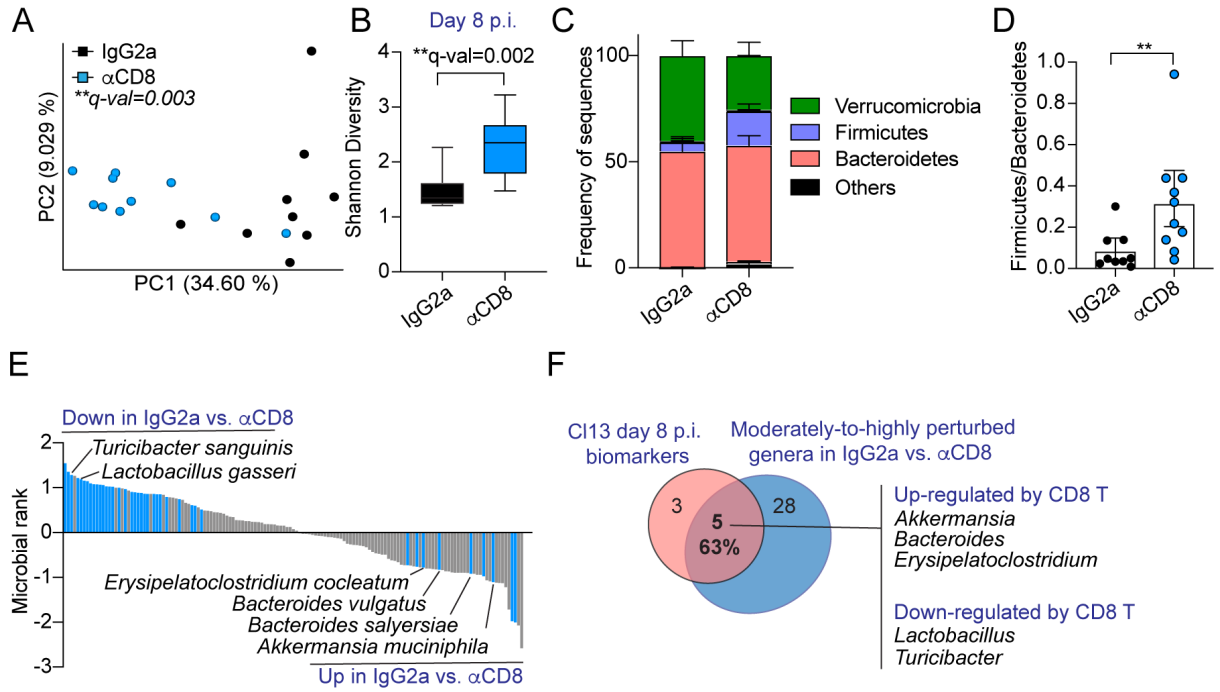

Figure 2-3. CD8 T cells drove great part of the intestinal dysbiosis identified after LCMV Cl13 infection. C57BL/6 mice were infected with LCMV Cl13, injected intraperitoneally (i.p.). with isotype control (IgG2a) or CD8-depleting antibodies (αCD8) followed by shotgun metagenomics sequencing of colonic and caecal contents on day 8 p.i. (A) Beta-diversity PCoA with Jaccard distance. (B) Alpha diversity by the Shannon diversity index. (C) Frequency of sequences at the phylum level. (D) Frequency of phylum Firmicutes over Bacteroidetes for each mouse. (E) Songbird MR analysis of species in IgG2a- vs. αCD8-treated Cl13-infected mice. Taxa with rank cut-off values of -0.5 and 0.5 that were perturbed in the same direction in two independent experimental repeats are highlighted in blue and indicated by name. (F) Overlap between Cl13-specific biomarkers at day 8 p.i. (as defined in Fig. 1F) and altered genera upon CD8-T-cell depletion as defined in E. (B-D) Averages and min or max (B) or ± S.E.M. (C, D). (A-F) Representative data from one independent experiment with n=9-10 mice/group. (A) PERMANOVA with 999 permutations, (B) Kruskal-Wallis test, (D) Mann-Whitney test; *p or q-val<0.05, **<0.01.

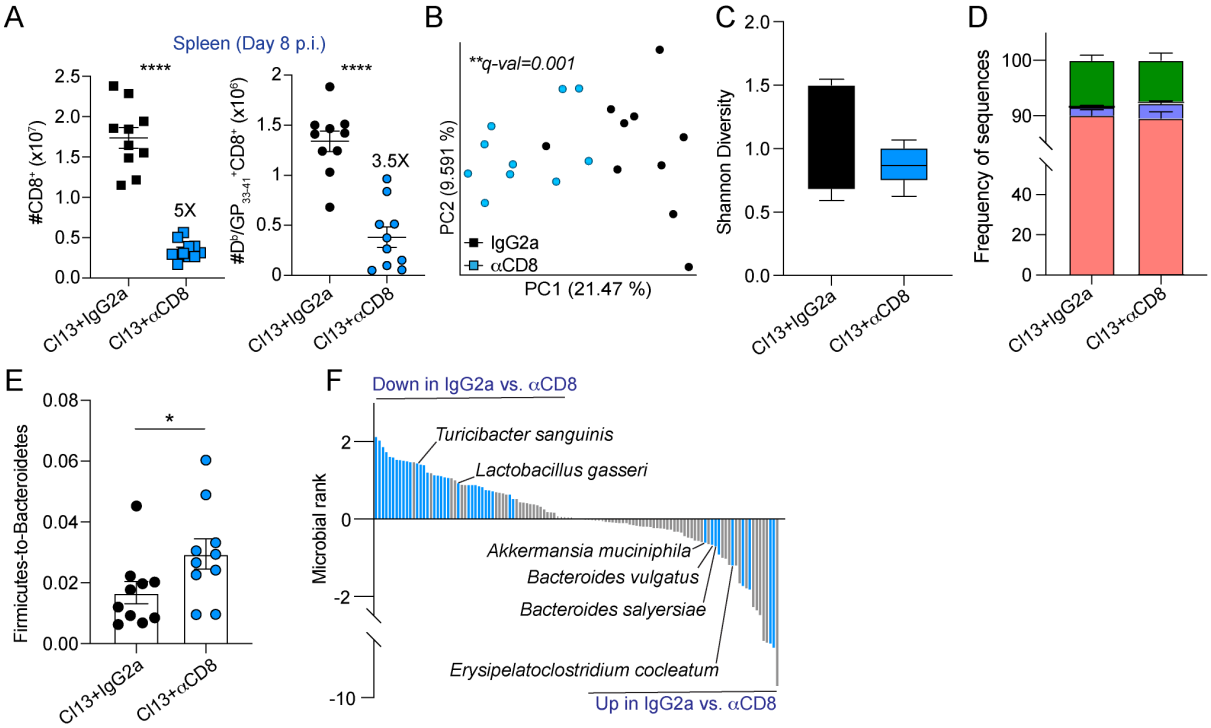

Figure 2-4. Anti-CD8 antibodies efficiently depleted CD8 T cells and shifted the composition of the intestinal microbiome after LCMV Cl13 infection. C57BL/6 mice were infected with LCMV Cl13, injected intraperitoneally (i.p.). with isotype control (IgG2a) or CD8-depleting antibodies (αCD8). (A) Numbers of splenic total $CD8^+$ and $D^b/GP_{33\text{-}41}{}^+CD8^+$ cells. Numbers indicate the fold-change between groups. (B-F) Shotgun metagenomics sequencing was performed on colonic and caecal contents on day 8 p.i. (B) Beta-diversity PCoA with Jaccard distance. (C) Alpha diversity by the Shannon diversity index. (D) Frequency of sequences at the phylum level. (E) Frequency of phylum Firmicutes over Bacteroidetes for each mouse. (F) Perturbed species in IgG2a- vs. αCD8-treated Cl13-infected mice via Songbird MR analysis. Taxa with rank cut-off values of -0.5 and 0.5 that were perturbed in the same direction in two independent experimental repeats are highlighted in blue and indicated by name. (A,C-E) Averages ± S.E.M. (A,D,E) or min or max (C). (A-F) Representative data from one independent experiment with n=9-10 mice/group. (A,E) Mann-Whitney test, (B) PERMANOVA with 999 permutations, (C) pairwise Kruskal-Wallis with FDR correction; *p or q-val<0.05, **<0.01, ***<0.001, ****<0.0001

2.3.3 CD8-driven anorexia is associated with a fasting-related microbiome early after LCMV Cl13 infection

We next sought to investigate the mechanisms via which CD8 T cells promoted transient (and profound) dysbiosis after infection with the fast-spreading persistent LCMV Cl13 isolate. We considered that, among the day-8-Cl13 taxa biomarkers altered in a CD8-T-cell-dependent manner, the phylum Verrucomicrobia (i.e. *Akkermansia* genus), has been previously reported to increase in anorexic human patients (190) as well as in calorie-restricted rodents, some fish and snakes (191). We, therefore, investigated potential changes in eating behavior by comparing food consumption in ARM vs. Cl13 infected mice. We observed that Cl13, but not ARM infection, induced profound anorexia spanning from day 6 through 9 p.i. (Fig. 2-5A), that was accompanied by 18% ± 3.5 weight loss at day 9 p.i. (Fig. 2-6A). Importantly, continuous CD8 T cell depletion completely restored food consumption (Fig. 2-5B) and attenuated weight loss (Fig. 2-6B), which provided the first causal evidence that CD8 T cells can drive anorexic behavior. Intriguingly, efficient CD4-T-cell depletion (Fig. 2-6C) or IFN-I receptor (IFNAR) blockade did not prevent the induction of anorexia, even though IFNAR blockade (but not CD4 T cell depletion) consistently ameliorated its magnitude (Fig. 2-6D&E) and attenuated weight loss (Fig. 2-6F&G).

To investigate whether such anorexic behavior may explain some of the transient changes in the intestinal microbiome of Cl13-infected mice, we next compared the Cl13-driven microbiome to recently proposed microbiome biomarkers of colon carcinoma-bearing mice, which suffer from anorexia (151, 192). We observed that 3 out of the 8 Cl13-infection-specific biomarkers at day 8 p.i., as defined in Fig. 2-1F, overlapped with those from colon carcinoma, including reductions in *Lactobacillus* as well as enrichment in *Bacteroides* and *Akkermansia* (Fig. 2-5C red vs. blue circles). Of note, perturbation of these three taxa was reverted when anorexia was corrected, via

CD8-T-cell-depletion, in Cl13-infected mice (Fig. 2-5B and 2-3E&F). To elucidate which of these taxa biomarkers were common to anorexia, independent of inflammation, we applied Songbird MR analysis using rank cut-off values of 1 and -1 on publicly-available 16S rRNA gene amplicon data from uninfected mice under a caloric restricted diet (193) and compared the identified fasting-biomarkers (Dataset S2-6) with the Cl13-infection-driven microbiome. We observed that 2, *Sutterella* and *Akkermansia,* of the 8 microbial alterations detected during the early phase of Cl13 infection were commonly perturbed, in the same direction, during calorie restriction (Fig. 2-5C, red vs. yellow circles) and *Akkermansia* was overrepresented in the three juxtaposed conditions (Fig. 2-5C).

These data indicated that infection with a fast-spreading, and potentially persistent, virus induces a profound, CD8-T cell dependent anorexic behavior. Our results also demonstrated that a significant fraction of the taxa uniquely altered during the anorexic phase, including overrepresentation of *Bacteroides* and *Akkermansia* as well as reductions in *Lactobacillus*, were commonly perturbed in non-infectious fasting conditions and were no longer altered when anorexia was reverted, via CD8-T-cell depletion during infection. Thus, these findings situated anorexia as one possible mechanism via which CD8-T cell responses may induce dysbiosis after viral infection.

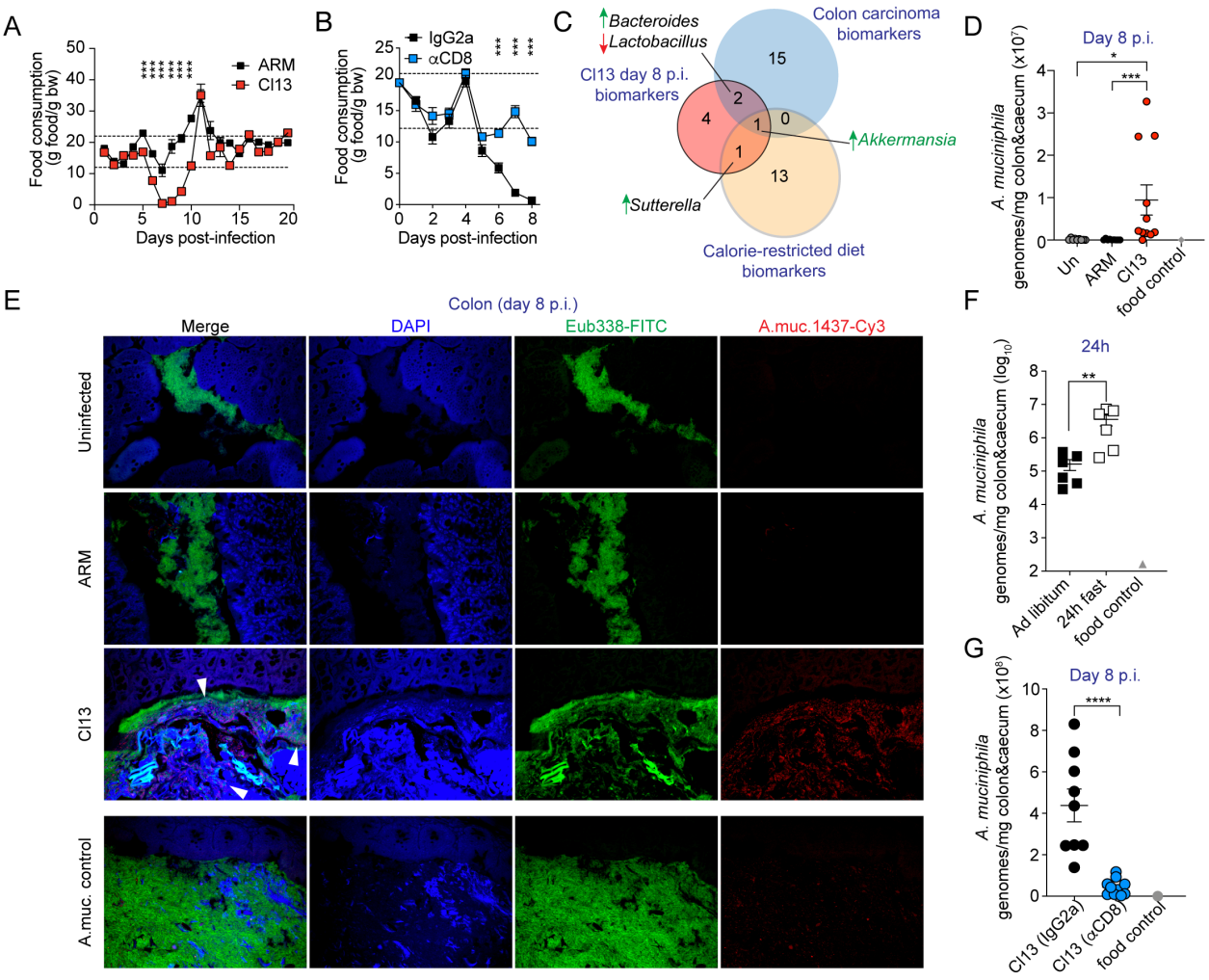

Figure 2-5. CD8-T-cell-driven anorexia is associated with a fasting-related microbiome, including natural blooming of *Akkermansia muciniphila*, early after LCMV Cl13 infection. C57BL/6 mice were infected with LCMV ARM, Cl13 or left uninfected (Un) (A,D,E) or infected with LCMV Cl13 and injected intraperitoneally (i.p.). with isotype control (IgG2a) or CD8-depleting antibodies (αCD8) (B,G). (A,B) Grams (g) of food consumed per g of body weight (bw) over-time in indicated groups. Dotted lines mark the healthy range of food consumption determined in uninfected mice as described in the methods section. (C) Taxa overlap of Cl13 day 8 p.i. biomarkers defined as in Fig. 1E (red), mouse colon carcinoma biomarkers defined by linear discriminant analysis effect size (194) of mice subcutaneously transplanted with colon cancer cells (blue), as reported in (192), and caloric restriction biomarkers defined after MR analysis with Songbird of the stools of mice after 3 weeks on a calorie-restricted diet, from a previous study (193) (yellow). (D, F, G) Absolute *A. muciniphila* genomes in colonic and caecal contents were quantified by qPCR in uninfected mice or mice infected with LCMV ARM or Cl13 at day 8 p.i. (D), in uninfected mice fed *ad libitum* or fasted for 24 hrs (F) and in Cl13-infected mice treated with CD8-depleting or isotype control antibodies (G). DNA from a food pellet was used as a negative control (food control). (E) Fluorescence *In Situ* Hybridization (FISH) images with *Eubacteria* (Eub338, green) or *A. muciniphila* (A.muc.1437, red)-specific probes on colon sections from Un, ARM- and Cl13-infected mice at day 8 p.i. One uninfected mouse was intraorally- (i.o.) inoculated with ~1.2x10^8 colony-forming units (cfu) of live *A. muciniphila* 24 hrs prior to necropsy and was used as positive control (A.muc. control). (A,B,D,F,G) Averages ± S.E.M. Data are representative of one out of three (A,B), two (E,G) or pooled from two (F) or three (D) independent experiments with n=3-10 mice/group. (A,B) Unpaired two-tailed t-Student's test per

time-point, (F,G) Mann-Whitney test, (D) one-way ANOVA with Tukey's correction; *p-val<0.05, **<0.01, ***<0.001, ****<0.0001.

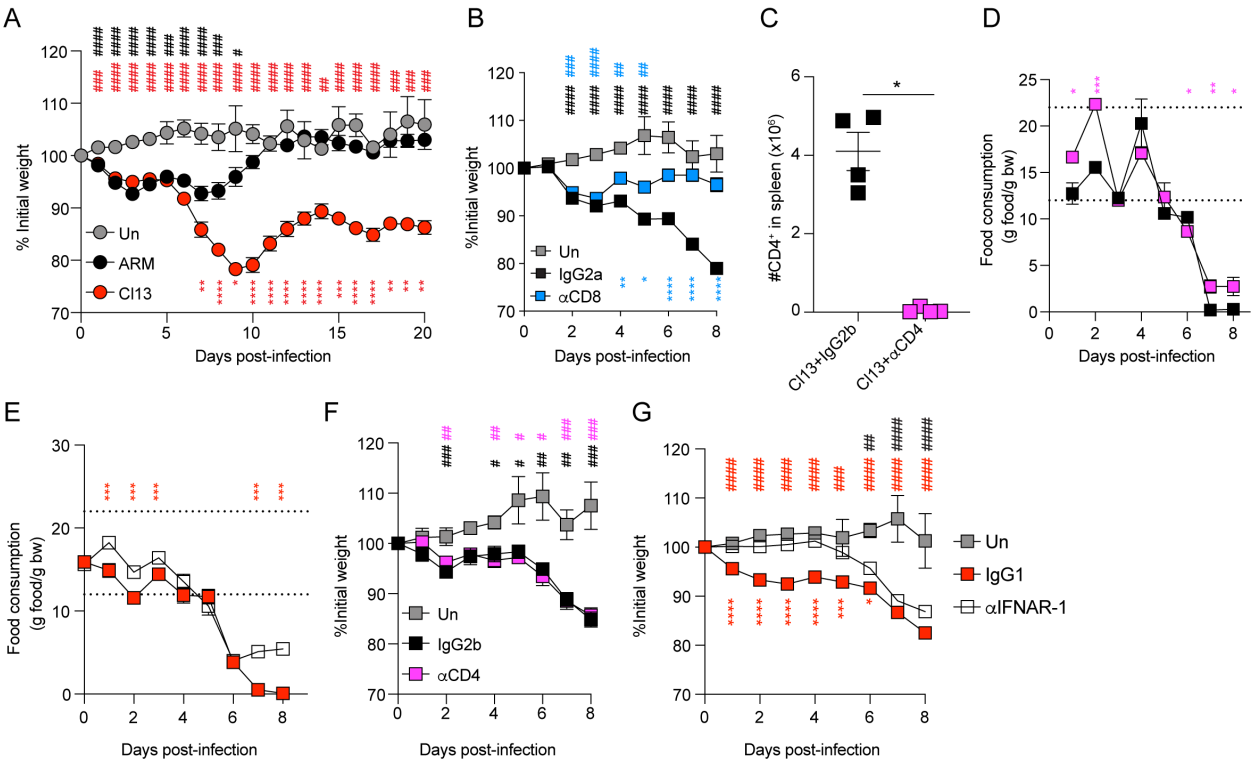

Figure 2-6. Weight loss after LCMV Cl13-infection was profoundly reverted by anti-CD8 antibody treatment while weight loss and anorexia were partially or not attenuated by anti-IFNAR or anti-CD4 antibodies, respectively. C57BL/6 mice were left uninfected (Un), infected with LCMV ARM (A) or Cl13 (A-G) and treated with isotype control IgG2a or CD8-depleting antibodies (αCD8, B), with isotype control IgG2b or CD4-depleting antibodies (αCD4, C,D,F) or with isotype control IgG1 or anti-IFNAR1 antibodies (αIFNAR-1, E,G) i.p. (A,B,F,G) Percentage of initial weight over-time. (C) Numbers of splenic $CD4^+$ cells at day 8 p.i. (D,F) Grams (g) of food consumed per g of body weight (bw) over-time in indicated groups. Dotted lines mark the healthy range of food consumption determined in uninfected mice as described in the methods section. (A-G) Average ± S.E.M. (A-G) Data are representative of three (B), two (C) or pooled from two (A, D-G) independent experiments with n=4-10 mice per group. (A,B,F,G) One-way ANOVA with Tukey's multiple comparisons correction for each timepoint with Cl13 vs. ARM (red *), Cl13 vs. Un (red #) and ARM vs. Un (black #) (A); αCD8 vs. IgG2a (blue *), αCD8 vs. Un (blue #) and IgG2a vs. Un (black #) (B); αCD4 vs. Un (pink #) and IgG2b vs. Un (black #) (F); αIFNAR-1 vs. IgG1 (red *), αIFNAR-1 vs. Un (black #) and IgG1 vs. Un (red #) (G). (C) Mann-Whitney test, (D,E) unpaired two-tailed Student's t-test. (D) Increased food consumption by the αCD4 group was significantly increased in one out of two experiments and after pooling. * or # p-val<0.05, ** or ## p-val<0.01, ***or ### p-val<0.001, **** or #### p-val <0.0001.

2.3.4 *Akkermansia muciniphila* blooms in a CD8-T-cell-dependent manner after LCMV Cl13 infection and is enriched upon lack of food consumption

Because the *Akkermansia* genus emerged as a common fasting biomarker in the inflammatory and non-inflammatory conditions that we compared in our analysis (Fig. 2-5C) we selected it for further validation and follow-up studies. Notably, within the genus *Akkermansia*, the commensal *Akkermansia muciniphila* (*A. muciniphila*) is the only species that colonizes the human gut (195). We therefore evaluated whether *A. muciniphila* was uniquely increased in Cl13 vs. ARM-infected mice. Quantification of *A. muciniphila* genomes by qPCR in colon and caecal contents from Cl13-infected vs. both uninfected and ARM-infected mice demonstrated its selective enrichment upon Cl13 infection (Fig. 2-5D). We next evaluated the localization of *A. muciniphila* by performing Fluorescence *In Situ* Hybridization (FISH) with an *A. muciniphila*-specific probe. This analysis further supported overrepresentations of *A. muciniphila* in Cl13-infected vs. ARM-infected and uninfected mice and mapped *A. muciniphila* to colon and caecal compartments (Fig. 2-5E and Fig. 2-7).

Finally, we sought to investigate a causal link between the blooming of *A. muciniphila* and the CD8-T-cell-induced anorexia after Cl13 infection. For that, we first quantified *A. muciniphila* genomes in colon and caecal contents from uninfected mice fed *ad libitum* or starved for 24 hrs. We observed that such a short interruption in food consumption alone, without viral infection, significantly increased the amount of *A. muciniphila* genomes by ~20 fold (Fig. 2-5F). Moreover, reversion of the anorexic behavior via CD8 T cell depletion in Cl13-infected mice (Fig. 2-5B) was accompanied with a significant reduction in intestinal *A. muciniphila* genomes (Fig. 2-5G).

Together, these results demonstrated that an absolute increase of *A. muciniphila* is part of the profound dysbiosis that occurred downstream of CD8 T cell responses during the early phase

of infection with a fast-spreading and persistent virus, and causally linked the lack of food consumption with *A. muciniphila* blooming in the intestinal compartment. Importantly, these findings further support a role for anorexia as one mechanism via which CD8 T cells may promote microbial dysbiosis, including enrichment of the *Akkermansia* genus, after viral infection.

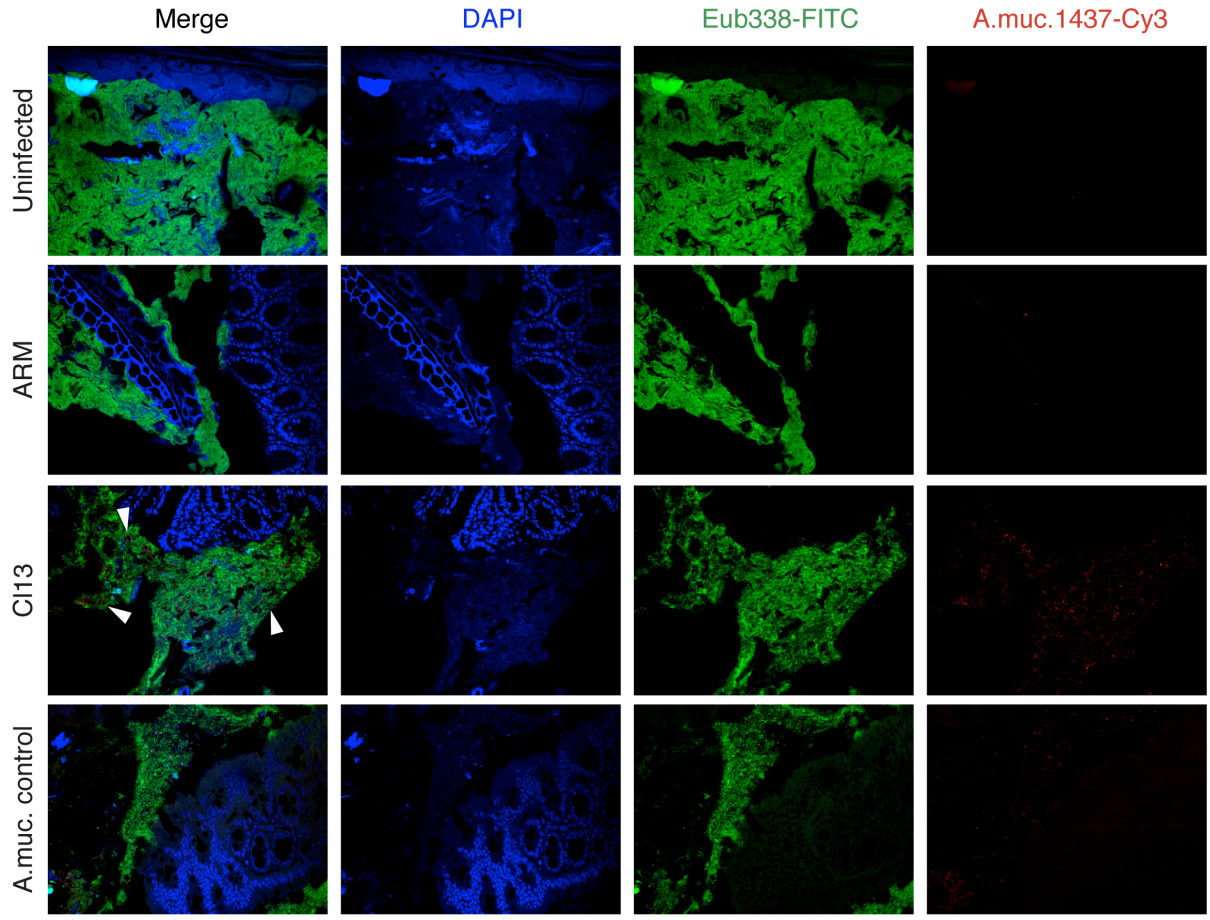

Figure 2-7. Increased *A. muciniphila* detection by FISH in caecums from Cl13-infected vs. ARM-infected and uninfected mice on day 8 p.i. Related to Figure 3. C57BL/6 mice were infected with LCMV ARM, Cl13 or left uninfected. Representative fluorescence In Situ Hybridization (FISH) images using specific probes for *Eubacteria* (Eub338, green) and *A. muciniphila* (A.muc.1437, red) along with nuclear DAPI staining, from caecums of respective mice on day 8 p.i. One uninfected mouse was intra-orally inoculated with ~1.2x10^8 cfu of live *A. muciniphila* 24 hrs prior to necropsy and served as positive control (A.muc. control). Images are representative of 2 experiments with n=3 mice per group.

2.3.5 Oral administration of *Akkermansia muciniphila* attenuated anti-viral CD8 T cell responses after LCMV infection

To investigate the potential bi-directional modulation of *A. muciniphila* and CD8 T cells, we experimentally induced *A. muciniphila* enrichment in ARM-infected mice, which neither become anorexic nor exhibit intestinal blooms of this commensal (Fig. 2-5A&D-E). We chose to inoculate ARM-infected mice with live *A. muciniphila* or vehicle control from days 3.5 to 7.5 p.i. to maintain comparable innate immune responses and CD8 T cell priming between the two groups. We next evaluated the impact on CD8 T cell responses within the small intestinal intraepithelial lymphocyte (IEL) compartment, which is in closest proximity to the intragastrically administered bacteria, and spleen, as a representative distal lymphoid organ. Analysis of LCMV-specific CD8 T cell responses from IEL demonstrated similar percentages and numbers (Fig. 2-8A) as well as equivalent expression of the cytotoxic molecule GrzB (Fig. 2-8B) and frequencies of killer cell lectin like receptor G1 (KLRG1) positive or $CD103^+$ cells (Fig. 2-8C), which mark cells with effector and tissue-resident phenotypes, respectively (196-198). We also observed equivalent accumulation of splenic LCMV-specific CD8 T cell populations (Fig. 2-9A) as well as their cytokine production (Fig. 2-9B) and proportions of short-lived, memory precursor and early effector cells (SLEC, MPEC, and EEC) (198-200), in both groups (Fig. 2-9C). Strikingly, however, we observed a significant reduction in GrzB levels among splenic CD8 T cells specific for the immunodominant LCMV epitope GP_{33-41} ($D^b/GP_{33-41}{}^+$), and to lesser extent among CD8 T cells specific for $NP_{396-404}$, in ARM-infected mice inoculated with *A. muciniphila* vs. control mice (Fig. 2-10A). We also found reduced levels of the transcription factor (TF) T-BET among $D^b/GP_{33-41}{}^+$ CD8 T cells (Fig. 2-10B), which is known to promote GrzB expression and CD8 T cell effector fate (198, 201). Given that trimethylation of Lysine 27 residue on histone 3 (H3K27me3) has been

shown to reinforce effector CD8 T cell differentiation (202, 203) we next evaluated the potential effect of *A. muciniphila* on CD8 T cell H3K27me3 marks. As shown in Fig. 2-10C, *A. muciniphila*-inoculated mice exhibited reduced H3K27me3 in virus-specific-CD8 T cells compared to control mice. Importantly, *A. muciniphila* inoculation did not increase splenic Treg accumulation (Fig. 2-9D). Of note, reduced GrzB and T-BET were also observed in splenic CD8 T cells after Cl13 infected mice were inoculated with *A. muciniphila* (Fig 2-10D, E), indicating that the effects of this commensal on CD8 T cell responses were conserved in the context of functional (acute infection) or exhausted (chronic infection) CD8 T cells. Finally, although *A. muciniphila* inoculation into ARM or Cl13 infected mice did not alter weight loss (Fig 2-11A&B), eating behavior (Fig. 2-11C&D), or the amount of infectious virus in liver, lung and/or blood (Fig 2-11E-I), it did cause a significant delay in the clearance of LCMV ARM genomes from the livers (Fig. 2-10F).

Together, these data indicated that *A. muciniphila* inoculation attenuated splenic, but not small intestinal, CD8 T cell responses, specifically diminishing expression of GrzB and T-BET as well as reducing H3K27me3 marks. Such CD8 T cell suppression seemed to be accompanied with a delayed clearance of the acute infection in mice receiving *A. muciniphila*. Interpretation of these results should take into consideration that, consistent with a previous report that used a similar dose of this bacterium (204), qPCR in caecal and colonic compartments did not detect significant enrichment of *A. muciniphila* after its oral administration (Fig. S2-12). Such low levels of *A. muciniphila* in the experimentally treated mice raises the possibility that the phenotypes we observed after inoculation of this commensal into infected mice may represent an underestimation of the effects caused by the profound *A. muciniphila* blooming that naturally arises after Cl13 infection.

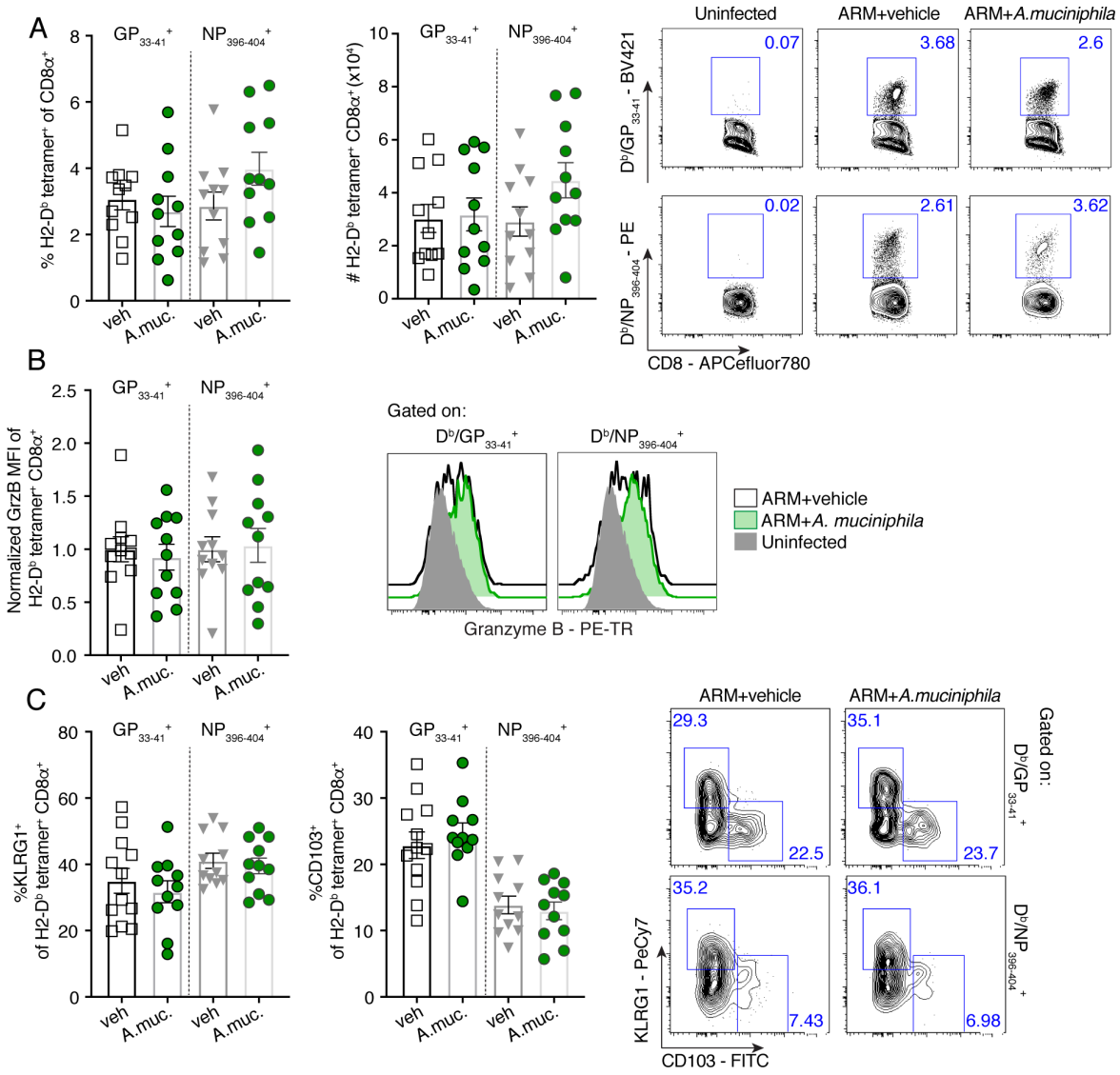

Figure 2-8. *A. muciniphila* inoculation into LCMV ARM-infected mice did not alter accumulation, effector features or differentiation of small intestinal IEL CD8 T cells. C57BL/6 mice were infected with LCMV ARM and intraorally inoculated with vehicle (veh) or ~1.2x10^8 cfu of live *A. muciniphila* (A.muc.) once daily on days 3.5 through 7.5 p.i. Small intestine IEL FACS analysis was done on day 8 p.i. (A) Frequencies, numbers and representative FACS plots of D^b/GP_{33-41}^+ and $D^b/NP_{396-404}^+$ CD8 T cells. (B) Granzyme B (GrzB) MFI normalized to the average of the vehicle control and representative FACS plots within gates for D^b/GP_{33-41}^+ and $D^b/NP_{396-404}^+$ CD8 T cells. (C) Frequencies of $KLRG1^+$ (left) or $CD103^+$ (right) of D^b/GP_{33-41}^+ and $D^b/NP_{396-404}^+$ CD8 T cells and representative FACS plots within gates for D^b/GP_{33-41}^+ and $D^b/NP_{396-404}^+$ CD8 T cells. (A-C) Average ± S.E.M. (A-C) Data are pooled from three independent experimental repeats with 3-5 mice/group. (A-C) Unpaired two-tailed Student's t-test.

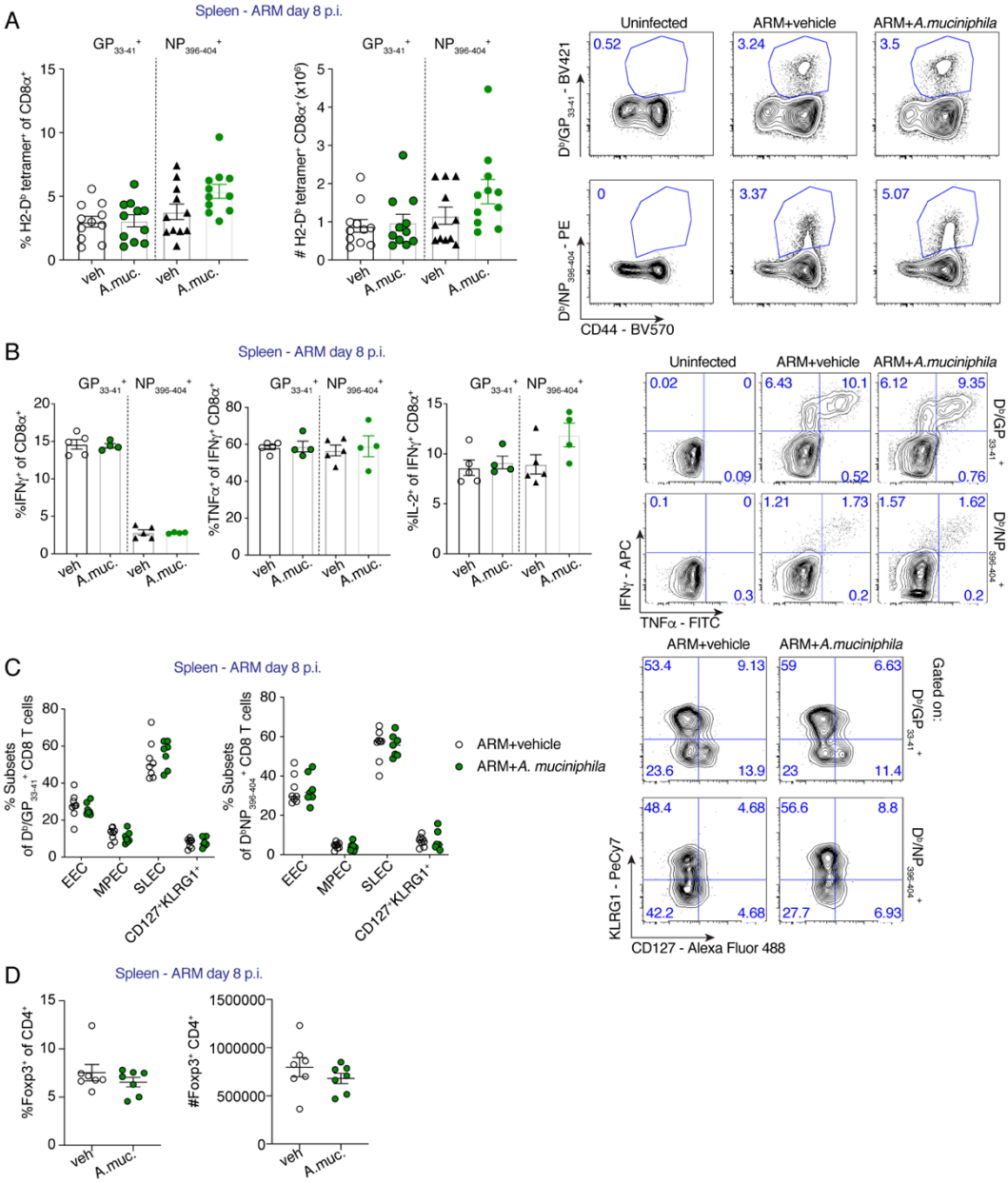

Figure 2-9. *A. muciniphila* inoculation into ARM-infected mice did not alter accumulation, cytokine-production or differentiation of spleen CD8 T cells nor accumulation of CD4$^+$Foxp3$^+$ T cells. Related to Figure 4. C57BL/6 mice were infected with LCMV ARM and administered vehicle (veh) or ~1.2x10^8 cfu of live *A. muciniphila* (A.muc.) i.o. once daily on days 3.5 through 7.5 p.i. Spleen FACS analysis was done on day 8 p.i. (A) Frequencies, numbers and representative FACS plots of D^b/GP$_{33\text{-}41}^+$ and D^b/NP$_{396\text{-}404}^+$ CD8 T cells. (B) Frequencies of IFN□-producing, IFNγ and TNFα- or IFNγ and IL-2- co-producing CD8 T cells upon *ex vivo* restimulation with indicated peptides; and representative FACS plots for IFNγ and TNFα staining. (C) Frequencies of EEC, MPEC, SLEC or CD127$^+$KLRG1$^+$ subsets defined by KLRG1 and CD127 expression among D^b/GP$_{33\text{-}41}^+$ and D^b/NP$_{396\text{-}404}^+$ CD8 T cells; and representative FACS plots. (D) Percentages and numbers of CD4$^+$ Foxp3$^+$ Treg. (A-D) Average ± S.E.M. (A-D) Data are pooled from two (D), three (A, C) independent experimental repeats with 3-5 mice/group or

are representative of one out of three independent experiments that showed equivalent results (B). (A-D) Unpaired two-tailed Student's t-test.

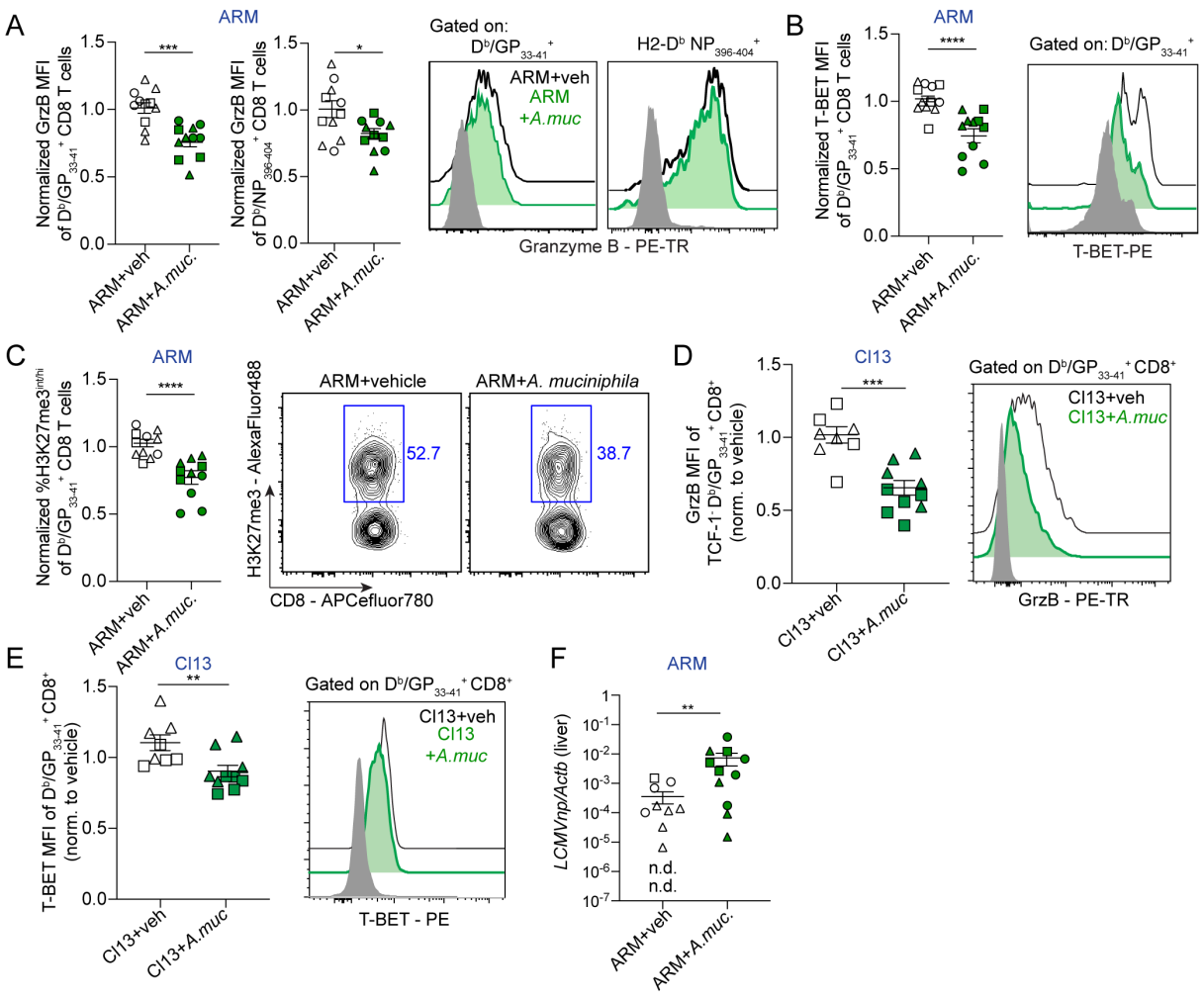

Figure 2-10. Oral administration of *Akkermansia muciniphila* into LCMV ARM or Cl13-infected mice attenuated selected CD8 T cell effector features. See also Figures S5-8. C57BL/6 mice were infected with LCMV ARM (A-C,F) or LCMV Cl13 (D,E) and inoculated i.o. with vehicle (veh) or ~1.2x10^8 cfu of live *A. muciniphila* (A.muc.) daily from day 3.5-7.5 p.i. All analyses were done at day 8 p.i. (A,B,D,E) Mean fluorescence intensity (MFI) for Granzyme B (GrzB) (A,D) and T-BET (B,E) among gated LCMV tetramer $D^b/GP_{33-41}{}^+$ $CD8^+$ cells from the spleen. (C) Frequency of $H3K27me3^{int/hi}$ cells among D^b/GP_{33-41} or $D^b/NP_{396-404}$ tetramer$^+$ $CD8^+$ in the spleen, as indicated. (A-E) Values are normalized to the average of the vehicle control group. (A-E) Representative FACS histograms are shown for the indicated groups; grey histogram was gated on $CD8^+$ from Un mice. (F) Liver levels of *LCMVnp* normalized to *Actb*. (A-F) Pooled data from three (A-C,F) or two (D,E) experiments with n=3-5 mice/group. Individual experiments are indicated with different shapes (i.e. circles, squares, triangles). (A-F) Averages ± S.E.M. (A-F) Unpaired two-tailed t-Student's test. Statistically significant differences were detected in 3 out of 3 (B,C), 2 out of 3 (A, for D^b/GP_{33-41}), 2 out of 2 (D) or 1 out of 2 (E) independent experiments. Even when not reaching statistical significance, individual experiments showed a consistent trend that, in all cases, reached significance after pooling data from independent repeats. For A ($D^b/NP_{396-404}$) and F, differences only reached statistical significance after pooling independent experimental repeats; *p-val<0.05, **<0.01, ***<0.001, ****<0.0001.

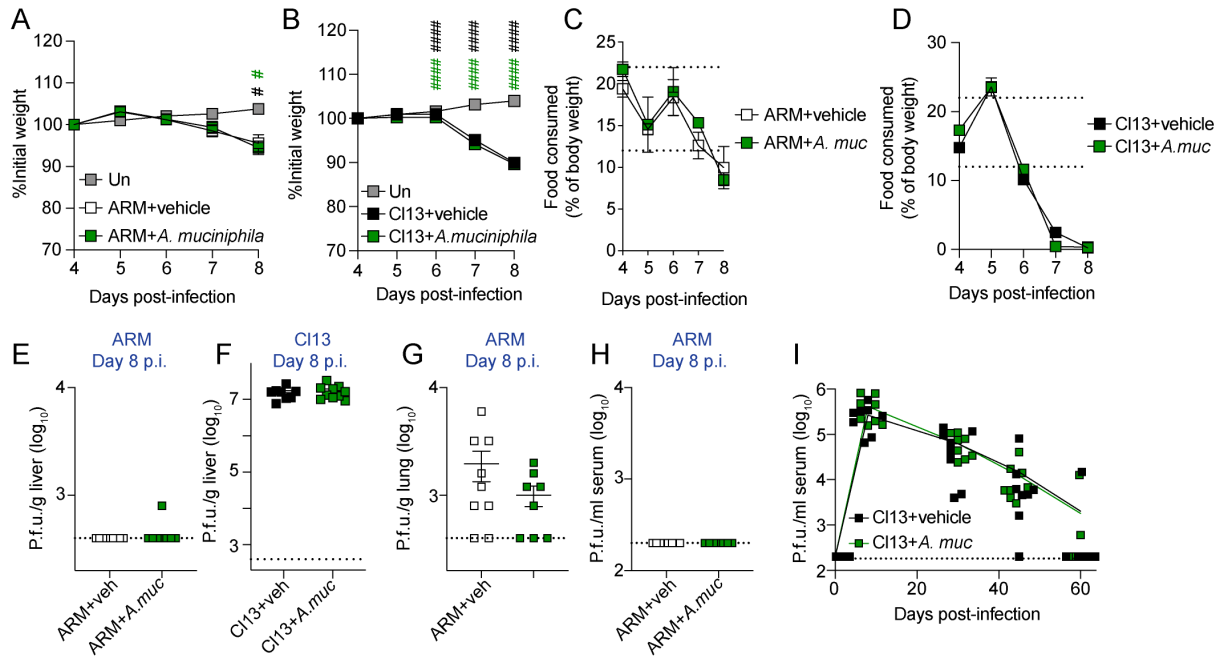

Figure 2-11. *A. muciniphila* inoculation into LCMV ARM- or Cl13-infected mice did not alter weight loss, eating behavior or titers of infectious viral particles at the time points assessed. Related to Figure 4. C57BL/6 mice were left uninfected (Un) (A-B), infected with ARM (A,C,E-G) or with Cl13 (B,D,H,I) and administered vehicle (veh) or ~$1.2x10^8$ cfu of live *A. muciniphila* (A.muc.) i.o. once daily on days 3.5 through 7.5 p.i. (A,B) Percentage of initial weight over-time. (C,D) Grams (g) of food consumed per g of body weight (bw) over-time in indicated groups. Dotted lines mark the healthy range of food consumption determined in uninfected mice as described in the methods section. (E-I) Infectious viral particles were quantified by plaque assay in liver (E,F), lung (G) and serum (H,I) at time points indicated. (A-I) Average ± S.E.M. Data are pooled from three (A,C) or two (B,D,E-I) independent experiments with n=4-8 mice/group. (A,B) One-way ANOVA with Tukey's multiple comparisons correction with vehicle vs. Un (black #) and *A. muciniphila* vs. Un (green #). (C-I) Unpaired two-tailed Student's t-test; # p-val <0.05, ### p-val <0.001.

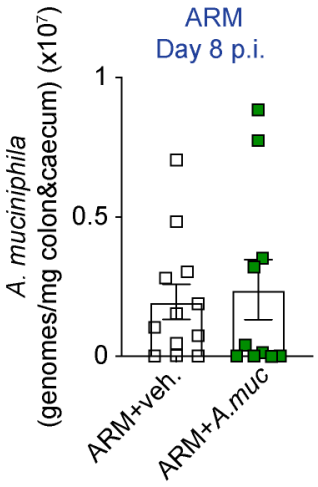

Figure 2-12. Intestinal *A. muciniphila* levels were not significantly increased after oral inoculation of live cultures of this commensal into LCMV ARM-infected mice. Related to Figure 4. C57BL/6 mice were infected with ARM and administered vehicle (veh) or ~$1.2x10^8$ cfu of live *A. muciniphila* (A.muc.) i.o. once daily on days 3.5 through 7.5 p.i. Absolute *A. muciniphila* genomes in colonic and caecal contents were quantified by qPCR at day 8 p.i. Average ± S.E.M. Data are pooled from three independent experiments with n=3-5 mice/group. Unpaired two-tailed Student's t-test.

2.4 Discussion

Host adaptations to fast spreading and/or persistent pathogen replication are often required to ensure host survival in various host species and include mechanisms such as the attenuation of both innate and adaptive arms of the immune system (1, 6, 170). Here, we found that infection with a fast-spreading persistent virus induced profound microbiome alterations, which were different from the ones induced by a closely-related acute virus that spreads at a slower rate. Interestingly, most microbiome alterations induced by the fast-spreading persistent virus were restricted to the early phase of infection and did not associate with continuous viral replication into the chronic phase. Instead, such microbiome dysbiosis was driven by CD8 T cell responses and partially associated with CD8 T-cell-induced anorexia. Remarkably, among the most enriched taxa detected early after infection with the fast-spreading persistent virus, we identified the fasting-associated commensal *A. muciniphila*, which bloomed in a CD8 T-cell-dependent manner and was able to suppress selected aspects of distal CD8 T cell responses. Our results are the first demonstrating that the endogenous intestinal microbiome of an infected host differentially changes after infection with closely-related viruses that exhibit distinct capacity to spread and persist, and suggest that infection-induced changes in eating behavior and microbiome could act as both regulators and targets of CD8 T cell responses.

It is remarkable that the intestinal microbiome was more profoundly and transiently altered during the early vs. late phase of persistent LCMV infection, despite comparable viral replication at both time-periods. Furthermore, our data demonstrated that such early dysbiosis was caused, in great part, by CD8 T cell responses. Importantly, while the intestinal microbiome has been previously shown to modulate CD8 T cell responses (205-208) a role for CD8 T cells in modulating gut microbiome composition has never been reported. In this regard, the transitory

Verrucomicrobia and *Akkermansia* overrepresentation that we observed on day 8 (but not day 20) p.i. and its connection to fasting across several species (191) led us to identify a profound anorexic behavior that was restricted to the early phase of LCMV Cl13 infection. This result is in agreement with an independent study that showed anorexia in the same LCMV model system (209). Here we validated these findings and expanded them by demonstrating that the aforementioned anorexia observed early after infection with the fast-spreading LCMV isolate is dependent on CD8 T cells. Given that anorexia has been observed at time points when strong CD8 T cell responses are detected after other chronic and acute infections (210-214), it is tempting to speculate that CD8-T-cell-induced anorexia may represent a conserved response to tissue damage or excessive inflammation upon infection with pathogens that overwhelmingly replicate in vital organs and/or are still present at high titers when CD8 T cell responses peak.

Consistent with the aforementioned anorexic behavior in LCMV infection, we observed that a significant fraction of the microbiome changes were commonly detected in other inflammatory and/or non-inflammatory fasting conditions. Among them, we demonstrated that the species *A. muciniphila* naturally bloomed in the caecum and colon during the early phase of infection with the LCMV Cl13 isolate, it was rapidly boosted in response to lack of food consumption and was significantly reduced when anorexia was reverted by CD8 T cell depletion. Given that fiber-deprived diets promote blooms of *A. muciniphila* (149), it is possible that the lack of dietary fiber intake early after LCMV Cl13 infection may have provided a niche for the outgrowth of *A. muciniphila*. Regardless, our observations linked *A. muciniphila* blooming with CD8-T-cell driven anorexia and supported the conclusion that anorexia is one means via which CD8 T cells induce intestinal dysbiosis after chronic infection. It should be noted, however, that not all taxa modulated by CD8 T cells during LCMV Cl13 infection were commonly altered in the

non-infectious fasting conditions that we analyzed here, suggesting the existence of alternative, anorexia-independent mechanisms employed by CD8 T cells to modulate gut microbial composition. On the other hand, the phylum Verrucomicrobia is also augmented after infection with influenza virus (215), which induces anorexia with a similar kinetic as LCMV Cl13 (216), suggesting that *A. muciniphila* and possibly other fasting associated commensals may bloom, perhaps also in a CD8-T-cell dependent manner, during some acute respiratory infections.

While it was previously demonstrated that the intestinal microbiome as a whole promotes pre-infection, tonic, expression of genes related to antiviral immunity in macrophages and enhances resistance to a subsequent chronic infection (147), the potential impact of the changes in specific commensal species that are induced after a chronic infection has been initiated remained unknown. In this regard, we found that enrichment of *A. muciniphila* via oral administration into specific pathogen free (SPF) LCMV-infected mice (that had unmanipulated microbial communities) suppressed selected effector features (i.e. GrzB, T-BET and/or H3K27me3) in virus-specific CD8 T cells and appeared to delay viral control in the liver. These observations were particularly unexpected given the beneficial effects that *A. muciniphila* has been ascribed during checkpoint blockade therapy (217). We speculate that the differential microbial communities into which *A. muciniphila* is introduced may account for some of these discrepancies, as individual bacterial species are heavily influenced by the complex microbial environments surrounding them (218). Alternatively, given that different CD8 T cell subsets are present at early vs. late timepoints after chronic infections (35, 36) and in tumors (34, 41), it is possible that the effect of *A. muciniphila* on CD8 T cell responses may vary depending on the time of administration. In spite of that, the effects we observed in virus-specific CD8 T cells upon early inoculation of *A. mucinipihila*, were consistent in the context of LCMV infections with any of the two isolates

studied, and were particularly impressive in the light of a previous report where modulation of CD8 T cell responses was only achieved after combined administration of 11 different taxa (207). Thus, our data support the possibility that the natural enrichment of *A. muciniphila* that we uncovered in the early phase after chronic viral infection may contribute to the attenuation of the initial virus-specific CD8 T cell responses, most likely in conjunction, and possibly in a redundant fashion, with other fasting-associated commensals and with previously described T-cell-inhibitory mechanisms (1, 6).

Interestingly, we observed that *A. muciniphila* attenuated distal CD8 T cells in the spleen but did not seem to have an effect on IEL CD8 T cells from the small intestine, despite their closer proximity to intestinal bacteria. Even though we cannot rule out effects in the large intestine, this is particularly unexpected since *A. muciniphila* has been recently shown to induce bacteria-specific immune responses in the small intestine (219). Given that *A. muciniphila* is known to strongly influence whole-body metabolism (204, 220, 221), it is possible that it suppresses CD8 T cell effector features by changing the nutrients available to fuel ensuing immune responses, which in turn can affect functional capacity and epigenetics in a cell-type or tissue- specific manner (222). Indeed, nutrient requirements may vary among tissues, providing a possible explanation for the differential effects of *A. muciniphila* in spleen vs. small intestinal IEL CD8 T cells. Regardless of the mechanism underlying *A. muciniphila* effects in distal vs. local tissues, our findings describe a commensal regulating distal, virus-specific CD8 T cell responses, without causing similar phenotypes in the small intestine IEL, broadening our current understanding of microbiome-mediated immune system regulation.

In conclusion, by revealing CD8-T-cell-dependent anorexia, CD8-T-cell-mediated blooming of *A. muciniphila* and CD8-T-cell attenuation by this commensal, our study suggests a

potential new way of CD8-T cell autoregulation that involves changes in host behavior and microbiome. In this context, we propose a model in which the blooming of *A. muciniphila* that we described here may be part of a whole-organism negative feedback loop initiated by CD8-T-cell-driven changes in eating behavior, that can lead to microbiome alterations, which may, in turn, contribute to the attenuation of CD8 T cell responses. Suppression of CD8 T cell responses through previously described inhibitory mechanisms (6, 19) along with the contribution of the aforementioned negative feedback loop may explain the recovery from the CD8-T-cell-dependent anorexic behavior alongside with the mostly transient nature of the CD8-T-cell-dependent dysbiosis, as the host transitions from the acute into the chronic phase of a persistent infection. Last but not least, it is important to emphasize that there is great interest in *A. muciniphila* as a potential probiotic (223-225), that is reflected by recently finalized (220) and ongoing clinical trials (NCT02086110; NCT03547440; NCT03749291; NCT04038619; NCT04058392). Our work unveils additional effects of this potential new-generation probiotic in regard to its capacity to attenuate ensuing CD8 T cell responses. As non-FDA regulated probiotics are being consumed by 3.9 million individuals in the US alone (226) increased understanding of context-dependent consequences of probiotic administration is needed to maximize their beneficial properties while preventing undesired side effects.

2.5 Author contributions

L.L.-B. designed, performed, analyzed, interpreted and conceptualized all experiments, and wrote the manuscript. A. G.-S. helped perform experiments in Fig. 3A&D, Fig. S3A, Fig. S5&6 and Fig. 4. R.R.G. performed all FISH analyses in Fig. 3E and Fig. S4. K.R.K. helped perform day 20 microbiome experiments in Fig. 1 and Fig. S1. G.H., T.S. and K.S. performed all pre-processing and 16S/shotgun metagenomics sequencing. A.S. assisted with experimental design of microbiome studies and provided guidance in -omics data analysis. R.K. supervised microbiome analysis and provided advice. M.R. supervised FISH studies and provided advice. E.I.Z. conceived and supervised the project, designed, interpreted and conceptualized experiments, and wrote the manuscript. All listed authors revised the manuscript.

2.6 Acknowledgements

We thank members of the Zuniga laboratory for discussions and critical reading of the manuscript. We thank Dr Julia M. Gauglitz for initial multinomial regression analyses, Dr Clarisse A. Marotz and Dr Pedro Belda-Ferre for key assistance with anaerobic cultures, Dr Gail Ackermann for data upload and metadata curation on Qiita, Dr Tomasz Kosciolek for guidance with Qiita/QIIME, 'Qiita help' personnel for assistance with Qiita as well as personnel at the Animal Facility and the IGM Genomics center sequencing core at UCSD.

Chapter 2, in full, will be submitted for publication as it appears. Lara Labarta-Bajo was the primary investigator and author of this paper. I would like to thank co-authors Anna Gramalla-Schmitz, Dr. Romana R. Gerner, Dr. Gregory Humphrey, Dr. Tara Schwartz, Dr. Karenina Sanders, Dr. Austin Swafford, Dr. Rob Knight, Dr. Manuela Raffatellu and Dr. Elina I Zúñiga for their contributions.

2.7 Materials and Methods

Mice, infections and antibody treatments

All of our studies were performed with six to ten-week-old female C57BL/6 mice bred at the Jackson Laboratories. For microbiome studies, purchased mice were randomly distributed in cages containing 5 mice each and housed in that way for 3 weeks before the day of infection per guidelines of the Earth Microbiome Project (227). Mice were infected intravenously (i.v.) with $2x10^6$ plaque forming units (PFU) of LCMV ARM or Cl13. Viral stocks were grown, identified and quantified as reported previously (14). Viral loads were determined by standard plaque assay (14) of serum or tissue homogenates. For CD8 T cell depletion studies, mice were intraperitoneally (i.p.) injected with anti-CD8α (53-6.72, BioXcell) or IgG2a (2A3, BioXcell) antibodies on day -2, -1, and 5 p.i. (250 μg/mouse) as well as on the day of infection (200 μg/mouse). For CD4 T cell depletion studies we used anti-CD4 (GK1.5, BioXcell) or IgG2b (LTF-2, BioXcell) antibodies at the same doses and times as described for CD8 T cell depletion. For IFNAR *in vivo* blockade, mice were i.p. injected with IFNAR neutralizing antibody (MAR1-5A3; BioXCell) or mouse IgG1 isotype control (MOPC-21; BioXcell) on days -1 and 0 p.i. (500 μg/mouse) as well as on days 2, 4 and 6 p.i. (250 μg/mouse) with Cl13 (89, 90).

For food consumption measurements, food pellets from cages containing four or five mice were weighed every 24 hrs. Grams of food consumed in each cage were then divided by the number of mice housed within the cage, normalized to the body weight of each mouse and multiplied by 100. In this way, we obtained the amount of food consumed per gram of body weight in the form of a percentage. Note that we chose to normalize by body weight to account for the differences in body weight among uninfected, ARM-infected and Cl13-infected mice (Fig. S3A). To establish a 'healthy range' of daily food consumption, food consumption measurements were taken every 24

hrs, for 30 consecutive days and from 10 uninfected female mice that were housed in two different cages containing 5 mice each. To estimate the healthy range, we computed the average daily food consumption ± one standard deviation from all measurements taken during the 30 days (i.e. 17 g of food/g of body weight ± 5). For acute starvation experiments, food pellets were removed from cages containing three uninfected mice for a total of 24 hrs. Mice were maintained in a closed breeding facility located at the Biomedical Sciences Building or Pacific Hall at UCSD, where mice were housed in ventilated cages containing HEPA filters. Mouse handling conformed to the requirements of the National Institutes of Health and the Institutional Animal Care and Use Guidelines of UCSD.

Lymphocyte isolation from spleen and small intestinal IEL

Spleens were harvested, digested for 20 min at 37 ^{o}C in 1mg/ml collagenase D (Roche) and mashed through a 100 μm filter. Cells were then centrifuged at 1500 rpm at 4^{0}C for 5 min. Red blood cells (RBC) were lysed by incubating pellets in 1ml of RBC-lysis buffer (150mM NH_4Cl, 10mM $KHCO_3$, 0.1mM Na_2EDTA in deionized water, at pH 7.4) for 4 min at room temperature (RT). After RBC lysis, 10ml of FACS buffer (PBS1x + 3%FBS) were added followed by centrifugation as stated above. Pellets were resuspended in 5ml of complete Roswell Park Memorial Institute (RPMI, Gibco), which consisted of RPMI supplemented with 10% heat-inactivated Fetal Bovine Serum (FBS, Atlanta Biologicals), 2% Penicillin/Streptavidin (P/S, BioWhittaker), 1 mM Sodium Pyruvate (Na-pyr, Thermo Scientific), 1mM L-Glutamine (L-Gln, BioWhittaker), 20 mM HEPES (Thermo Scientific) and 55 mM beta-mercaptoethanol (Life Technologies). Absolute leukocyte numbers were determined via FSC/SSC gating in a Guava Easycyte automated cell counter (MilliporeSigma, MA).

Small intestines were harvested, cleaned from adipose tissue, flushed and macroscopically visible Peyer's Patches were excised. To isolate the epithelial layer, intestines were longitudinally and transversely cut into 1-2 cm pieces, placed in Pyrex conical flask containing a stirring magnet and 30 mL of 'IEL buffer', and stirred on a stirring plate (Scilogex) set at 37 ^{o}C for a total of 15 min. IEL buffer consisted of 1xPBS supplemented with 3% FBS, 2% P/S, 1mM Na-pyr, 20 mM HEPES and 10 mM Ethylenediaminetriacetic Acid (EDTA, Thermo Fisher Scientific). The soluble fraction was then collected, diluted in RPMI supplemented with 3% FBS and pelleted by centrifugation at 1500 rpm for 5min at 4^{0}C. Epithelial pellets were resuspended in 5 ml of '44% Percoll solution' and 2.5 ml of '67% Percoll solution' were added underneath with a Pasteur pipette. Tubes were then spun down at 2000 rpm (with no brake set) at RT for 20 min. Percoll solution was prepared by adding 1 part of 10X PBS (Gibco) to 9 parts of Percoll (GE Healthcare Biosciences) and further mixed with IEL buffer to obtain a 44% or a 67% solution. The interphase layer containing IEL was collected after centrifugation, resuspended in 1ml of complete RPMI and leukocyte counts were determined with a Guava Easycyte (MilliporeSigma, MA) as indicated above.

Quantitative PCR

To quantify *A. muciniphila* genomes, previously frozen colonic and caecal contents were thawed, weighed, and DNA was extracted with DNeasy PowerSoil Kit (Qiagen) by following the manufacturer's protocol. Quantitative PCR (qPCR) was performed using Fast SYBR Green Master Mix (Thermo Fisher Scientific) and the following *A. muciniphila*-specific primers: F 5'-CAGCACGTGAAGGTGGGGAC-3', R 5'-CTTGCGGTTGGCTTCAGAT-3' with 10 ng of input DNA in triplicate. The qPCR reaction was ran following this protocol: 95 °C for 15 min, 40

cycles of 95 °C for 15 s, 66°C for 40 s, and 72°C for 30 s, as in (195), followed by melt curve analysis on a CFX96 Touch Detection System (Bio-Rad). DNA extracted from a food pellet was used as a negative control. To obtain an *A. muciniphila* qPCR standard, we extracted DNA from colonic and caecal contents from an uninfected mouse, as described above, and performed a regular PCR on a Veriti Thermal Cycler (Thermo Fischer Scientific) with the same *A. muciniphila*-specific primers as the ones used for qPCR and following this protocol: 95 °C for 15 min, 25 cycles of 95 °C for 15 s, 66°C for 40 s, and 72°C for 30 s. The resulting PCR reaction was ran on a 1% agarose gel and the 328 base pair (bp)-long PCR product was purified with a QIAquick Gel Extraction kit (Qiagen). The DNA concentration of the purified PCR product was determined with a NanoDrop One (Thermo Fisher Scientific) and serial dilutions of the standard were ran in parallel to all qPCR reactions described above and resulting Cq were used to create a standard curve. To estimate the amount of *A. muciniphila* genomes we applied the following formula: number of molecules (genomes) = [DNA weight (ng) * 6.022×10^{23} (molecules/mole)] / [328bp * 650 (g/mol/bp) * 1×10^{9} (ng/g)], where 6.022×10^{23} corresponds to Avogadro's Number and 650 corresponds to the average mass of 1 bp double-stranded DNA.

For quantification of transcripts in liver, tissues were collected from sacrificed mice, snap frozen and stored at -80 °C. Later, tissues were thawed, bead homogenized in RLT buffer (Qiagen) and centrifuged for 10 min 10,000 rpm to pellet debris. Supernatants were used for total RNA extraction using RNeasy kits (Qiagen), digested with DNase I (RNase-free DNase set; Qiagen) and reverse-transcribed into cDNA using M-MLV RT (Promega). The expression of LCMV nucleoprotein was quantified, in triplicates, using Fast SYBR Green Master Mix (Thermo Fisher Scientific) followed by CFX96 Touch Real-Time PCR Detection System (Bio-Rad). Relative transcript levels were normalized against murine *Actb*. Graphs depicting qRT-PCR analysis of

murine genes represent biological replicates of individual mice from one representative experiment or pooled experiments as indicated in figure legend. Q-PCR primer sequences are the following: LCMV nucleoprotein F 5′-GCATTGTCTGGCTGTAGCTTA-3′, R 5′-CAATGACGTTGTACAAGCGC-3′; *Actb* F 5'-AGGGAAATCGTGCGTGACAT-3', 5'-GAACCGCTCGTTGCCAATAG-3'.

Flow cytometry

Cells were stained at a maximal concentration of $2x10^8$ cells/ml in FACS buffer or as indicated below. For surface staining of splenocytes and IEL cells were first stained with a fixable viability dye (Ghost dye, Tonbo) in 1xPBS for 10 min at 4 °C followed by staining with MHC-I tetramers H2-D^b/$GP_{33–41}$-BV421 and H2-D^b/$NP_{396-404}$-PE provided by NIH Tetramer Core Facility (Atlanta, GA) in FACS buffer for 1h at RT followed by staining for 20min at 4°C with remaining surface antibodies. For intracellular staining after *ex vivo* peptide restimulation, cells were fixed in 1% paraformaldehyde (PFA) for 10min at RT and stained with antibodies in 1x perm/wash buffer (Thermo Scientific) for 30 min at 4 °C. Alternatively, for intranuclear staining, cells were fixed with the Foxp3 Transcription Factor Staining Buffer Set Kit (Thermo Scientific) per vendor's recommendation and stained with antibodies in 1x perm/wash buffer for 1h at RT. Antibodies used in this study were purchased from Thermo Fisher Scientific (Waltham, MA), BD Biosciences or Biolegend (San Diego, CA): GrzB PE-TR (GB11), T-BET PE (4B10), CD103 FITC (2E7), CD44 BV570 (IM7), CD127 Alexa Fluor 488 (A7R34), Foxp3 FITC (FJK-16s), CD8a BV786 or APC efluor 780 (53-6.7), CD4 BV650 or BV711 (RM4-5), IFNγ APC (XMG1.2), TNFα FITC (MP6-XT22), IL-2 PE (JES6-5H4), KLRG1 PeCy7 or PE-TR (2F1). Anti-H3K27me3 conjugated to Alexa Fluor 488 (C36B11) and anti-TCF1 (C63D9) conjugated to Alexa Fluor 647 were purchased

from Cell Signaling Technologies (Danvers, MA). Cells were acquired using a Digital LSR II flow cytometer (Becton Dickinson, San Jose, CA) or a ZE5 Cell Analyzer (Bio-Rad, Hercules, CA). Flow cytometric data were analyzed with FlowJo software v9.9.6 and v10.

Ex vivo T cell stimulation

Splenocytes were cultured at $1x10^7$ cells/ml in round-bottom 96-well plates for 5 h in complete RPMI supplemented with Brefeldin A (1 μg/mL; Sigma) and 1 μg/mL of the MHC class-I-restricted LCMV $NP_{396–404}$ or $GP_{33–41}$ peptides (all >99% pure; Synpep). Cells were then stained with a fixable viability dye (Tonbo Ghost Dye) and surface staining with the anti- CD8 mAbs described above, fixed in 1% PFA, permeabilized and stained with the aforementioned antibodies against IFNγ, TNFα and IL-2 in 1x perm/wash buffer for 30 min at 4^0C. Unstimulated controls in which cells were cultured without peptide were performed in parallel and showed background levels of cytokine staining.

Culture and inoculation of *Akkermansia muciniphila*

Akkermansia muciniphila (ATTC BAA-835) was purchased from ATCC. To make glycerol stocks, lyophilized *A. muciniphila* was re-suspended in liquid medium composed of Brain Heart Infusion (BHI) (Sigma) supplemented with 0.25% v/v type III mucin from porcine stomach (Sigma) and 100μM L-Cysteine (BHI+mucin media) that was previously sterilized and removed of oxygen, as in (195), and cultured in an anaerobic chamber (H_2 7.5%, CO_2 10%, O_2 < 10 ppm and N_2 as balance, Coy Lab) for 7 days, after which cultures were mixed with sterile glycerol at a final concentration of 25% w/v. To prepare mucin stocks, lyophilized mucin was solubilized in 0.1 M acetate buffer at pH 5 to make a 5% w/v mucin solution, autoclaved, aliquoted and kept at -

80°C until further use. To sterilize and to remove oxygen from the liquid medium, we injected CO_2 at 35 psi and N_2 at 50 psi for 35 min into the liquid medium while it was being stirred at 1500 rpm with a magnet. After that, we injected CO_2 at 50 psi and N_2 at 60 psi into the air space between the medium and the top of the media bottle for 5 min, after which the bottle was tightly sealed with a rubber stopper (DWK Life Sciences) and autoclaved for 15 min.

To initiate *A. muciniphila* cultures for oral inoculation, glycerol stocks were brought into the anaerobic chamber on dry ice, scraped with a sterile tip that was then placed in 3-5 mL of BHI+mucin media in 15 ml stopper cap falcon tubes and cultured at 37 ^{0}C in the anaerobic chamber for three to four days. Control tips with no *A. muciniphila* and media alone were cultured in parallel as a control for contamination and to be inoculated as vehicle control, respectively. Initially, it was determined that after three to four days of *A. muciniphila* glycerol stock culture in these conditions, the optical density at 600nm was 0.5-0.6, which after plating at serial dilutions corresponded to 5.5-6 x 10^8 colony forming units (cfu)/ml. 200µl of these cultures (i.e. ~1.2x10^8 cfu) or vehicle control were inoculated per mouse at indicated time-points. Note that very similar amounts of bacteria per dose have been used previously (204). *A. muciniphila* cultures were routinely plated in BHI+mucin media and 1% agar to confirm the homogeneity of the culture and to rule out potential contamination.

Bacterial Fluorescence in Situ Hybridization (FISH)

Caecal and colonic tissue samples from respective experimental groups were harvested and fixed in Carnoy's fixative (60% ethanol, 30% chloroform, 10% glacial acetic acid) and processed further as previously described (228). Tissue sections (5µM) were deparaffinized followed by hybridization for 4 hours at 46°C in the presence of 20% formamide utilizing the following probes

as reported earlier (229): pan-bacterial EUB338 (5′-GCTGCCTCCCGTAGGAGT-3′), non-EUB (5′-ACATCCTACGGGAGGC-3′) and species-specific A.MUC-1437 (5′-CCTTGCGGTTGGCTTCAGAT-3′). Probes were labeled at the 5′ and 3′ ends with fluorescein isothiocyanate (FITC), Cy5 or Cy3 Berlin (BioTez, Berlin, Germany). After washing, slides were counterstained and cover-slipped using ProLong® Gold Antifade Reagent including 4',6-diamidino-2-phenylindole (DAPI, Life Technologies, Grand Island, NY). Samples were viewed and imaged on an Olympus IX81 inverted microscope in combination with a FV1000 confocal laser scanning system.

Sample collection for microbiome studies

Mice were sacrificed, and peritoneal cavity opened with one set of tools. A new sterile set of tools was then used to retrieve colonic and caecal contents, which were placed in sterile tubes, frozen on dry ice and stored at -80°C. Both sets of tools were submerged in 70% ethanol between animals belonging to the same group and a new set of sterile tools was used when changing experimental groups.

DNA extraction for 16S rRNA V4 amplicon sequencing and shotgun metagenomic sequencing

We followed the protocol described in (157). Briefly, to extract DNA from colonic and caecal contents, frozen samples were thawed and transferred into 96-well plates containing garnet beads. DNA was extracted using Qiagen PowerSoil DNA kit adapted for magnetic bead purification and eluted in 100 µL of Qiagen elution buffer. DNA quantification was performed via Quant-iT PicoGreen Assay (Invitrogen).

Library generation and sequencing

Sequencing was done following standard protocols from the Earth Microbiome Project (158, 159). Extracted DNA was amplified by using barcoded primers. Each sample was PCR-amplified in triplicate and V4 pair-end sequencing or whole-genome sequencing using a miniaturized version of the KAPA HyperPlus kit was performed using Illumina MiSeq or HiSeq (La Jolla, CA).

16S rRNA gene amplicon data analysis

All 16S rRNA gene amplicon data are publicly available on Qiita (https://qiita.ucsd.edu/)(160) under study ID 11043. Processing of our 16S rRNA raw data involved splitting of FASTQ libraries, demultiplexing, trimming of sequences to 150bp of length (161) followed by deblur 1.1.0 (162) with Qiita default parameters as follows: indel probability of 0.01, mean per nucleotide error rate of 0.005, minimum per- sample read threshold of 2, Greengenes_13.8 as reference phylogeny for SEPP and 1 thread per sample). Features with a minimum frequency of 10 were retained and reference hit table obtained was rarefied to 10,000 counts, which was in the plateau region of alpha-rarefaction curves (163). To assign taxonomy, we used the pre-fitted sklearn-based taxonomy classifier ('classify_sklearn') with the Green Genes classifier (gg-13-8-99-515-806-nb-classifier) (164, 165). Raw 16S rRNA sequencing data from the stools of mice fed a calorie-restricted diet for 3 weeks (193) was obtained from NCBI Short Read Archive (SRA: PRJNA480387), uploaded to Qiita and processed as described above. Beta-diversity was computed with the 'beta_phylogenetic'module using Unweighted UniFrac or the 'beta' module using Jaccard and Bray-Curtis metrics. This was followed by principal coordinates analysis ('pcoa' module) and significance and differential dispersion were calculated for

'infection' with the 'beta_group_significance' module using PERMANOVA and PERMDISP tests, respectively, with 999 permutations. Alpha diversity was computed using the 'alpha' module for Shannon Diversity Index. All the aforementioned analyses were done with Qiita platform version 052020 5f09f46. To identify differentially abundant genera among groups in our 16S rRNA sequencing data as well as in caloric-restriction data (193), we collapsed our rarefied .biom tables to the genus level and used Songbird multinomial regression analysis (106) with default parameters (epochs of 10000, differential prior of 0.5) (https://github.com/biocore/songbird). We applied cut-off rank values of 1 and -1 to focus our analysis on highly perturbed genera. Validation of the model was performed for all analyses with tensor board.

Shotgun metagenomic data analysis

All shotgun metagenomics data are publicly available on Qiita (https://qiita.ucsd.edu/)(160) under study ID 11043. To pre-process these data we performed adapter trimming with Atropos v1.1.15 (166), followed by quality control filtering (QC_Filter) to bowtie2/Mus_musculus, followed by genome alignment of adapter-trimmed files with bowtie2 (with Rep94 database) (167) by running SHOGUN 0.1.5.(168) on Qiita (160). A table in .biom format with taxonomic predictions at the species level was then rarefied to a depth of 200,000 or 450,000. Alpha diversity was computed using the Shannon Diversity Index and beta-diversity was computed with the 'beta' module using Jaccard distance metric. PCoA representation and PERMANOVA were calculated as described above for the 16S rRNA gene amplicon data. To identify differentially abundant species between groups, we collapsed our rarefied .biom tables to the species level and used Songbird multinomial regression analysis (Morton et al., 2019) with parameters described above for 16S rRNA gene amplicon data analysis. In this case, we applied

cut-off rank values of 0.5 and -0.5 to include moderately and highly perturbed genera. Validation of the model was performed for all analyses with tensor board.

Statistical analysis

Unpaired two-tailed t-Student test was used to compare two groups. If variances were not equal by F-test, data were tested using the non-parametric Mann Whitney-U test. Significant differences among more than two groups were determined based on one-way ANOVA with Tukey's multiple comparison correction or, in the case of unequal variances, non-parametric Kruskal-Wallis test with Dunn's multiple comparison correction. Statistical tests were performed using GraphPad Prism v8.

References

1. Virgin, H. W., E. J. Wherry, and R. Ahmed. 2009. Redefining chronic viral infection. *Cell* 138: 30-50.

2. Organization, W. H. https://www.who.int/news-room/fact-sheets/detail/hepatitis-b

3. Organization, W. H. https://www.who.int/news-room/fact-sheets/detail/hepatitis-c.

4. Organization, W. H. https://www.who.int/gho/hiv/en/.

5. Stelekati, E., and E. J. Wherry. 2012. Chronic bystander infections and immunity to unrelated antigens. *Cell Host Microbe* 12: 458-469.

6. Zuniga, E. I., M. Macal, G. M. Lewis, and J. A. Harker. 2015. Innate and Adaptive Immune Regulation During Chronic Viral Infections. *Annu Rev Virol* 2: 573-597.

7. Charrel, R. N., B. Coutard, C. Baronti, B. Canard, A. Nougairede, A. Frangeul, B. Morin, S. Jamal, C. L. Schmidt, R. Hilgenfeld, B. Klempa, and X. de Lamballerie. 2011. Arenaviruses and hantaviruses: from epidemiology and genomics to antivirals. *Antiviral Res* 90: 102-114.

8. Kang, S. S., and D. B. McGavern. 2008. Lymphocytic choriomeningitis infection of the central nervous system. *Front Biosci* 13: 4529-4543.

9. Riviere, Y., R. Ahmed, P. J. Southern, M. J. Buchmeier, F. J. Dutko, and M. B. Oldstone. 1985. The S RNA segment of lymphocytic choriomeningitis virus codes for the nucleoprotein and glycoproteins 1 and 2. *J Virol* 53: 966-968.

10. Salvato, M., E. Shimomaye, and M. B. Oldstone. 1989. The primary structure of the lymphocytic choriomeningitis virus L gene encodes a putative RNA polymerase. *Virology* 169: 377-384.

11. Salvato, M. S., and E. M. Shimomaye. 1989. The completed sequence of lymphocytic choriomeningitis virus reveals a unique RNA structure and a gene for a zinc finger protein. *Virology* 173: 1-10.

12. Wright, K. E., R. C. Spiro, J. W. Burns, and M. J. Buchmeier. 1990. Post-translational processing of the glycoproteins of lymphocytic choriomeningitis virus. *Virology* 177: 175-183.

13. Kunz, S. 2009. Receptor binding and cell entry of Old World arenaviruses reveal novel aspects of virus-host interaction. *Virology* 387: 245-249.

14. Ahmed, R., A. Salmi, L. D. Butler, J. M. Chiller, and M. B. Oldstone. 1984. Selection of genetic variants of lymphocytic choriomeningitis virus in spleens of persistently infected

mice. Role in suppression of cytotoxic T lymphocyte response and viral persistence. *J Exp Med* 160: 521-540.

15. Ahmed, R., and M. B. Oldstone. 1988. Organ-specific selection of viral variants during chronic infection. *J Exp Med* 167: 1719-1724.

16. Wherry, E. J., J. N. Blattman, K. Murali-Krishna, R. van der Most, and R. Ahmed. 2003. Viral persistence alters CD8 T-cell immunodominance and tissue distribution and results in distinct stages of functional impairment. *J Virol* 77: 4911-4927.

17. Lauterbach, H., P. Truong, and D. B. McGavern. 2007. Clearance of an immunosuppressive virus from the CNS coincides with immune reanimation and diversification. *Virol J* 4: 53.

18. Oldstone, M. B. 2002. Arenaviruses. II. The molecular pathogenesis of arenavirus infections. Introduction. *Curr Top Microbiol Immunol* 263: V-XII.

19. Hashimoto, M., A. O. Kamphorst, S. J. Im, H. T. Kissick, R. N. Pillai, S. S. Ramalingam, K. Araki, and R. Ahmed. 2018. CD8 T Cell Exhaustion in Chronic Infection and Cancer: Opportunities for Interventions. *Annu Rev Med* 69: 301-318.

20. Reizis, B. 2019. Plasmacytoid Dendritic Cells: Development, Regulation, and Function. *Immunity* 50: 37-50.

21. Zajac, A. J., J. N. Blattman, K. Murali-Krishna, D. J. Sourdive, M. Suresh, J. D. Altman, and R. Ahmed. 1998. Viral immune evasion due to persistence of activated T cells without effector function. *J Exp Med* 188: 2205-2213.

22. Utzschneider, D. T., F. Alfei, P. Roelli, D. Barras, V. Chennupati, S. Darbre, M. Delorenzi, D. D. Pinschewer, and D. Zehn. 2016. High antigen levels induce an exhausted phenotype in a chronic infection without impairing T cell expansion and survival. *J Exp Med* 213: 1819-1834.

23. Bengsch, B., A. L. Johnson, M. Kurachi, P. M. Odorizzi, K. E. Pauken, J. Attanasio, E. Stelekati, L. M. McLane, M. A. Paley, G. M. Delgoffe, and E. J. Wherry. 2016. Bioenergetic Insufficiencies Due to Metabolic Alterations Regulated by the Inhibitory Receptor PD-1 Are an Early Driver of CD8(+) T Cell Exhaustion. *Immunity* 45: 358-373.

24. Staron, M. M., S. M. Gray, H. D. Marshall, I. A. Parish, J. H. Chen, C. J. Perry, G. Cui, M. O. Li, and S. M. Kaech. 2014. The transcription factor FoxO1 sustains expression of the inhibitory receptor PD-1 and survival of antiviral CD8(+) T cells during chronic infection. *Immunity* 41: 802-814.

25. Wherry, E. J., S. J. Ha, S. M. Kaech, W. N. Haining, S. Sarkar, V. Kalia, S. Subramaniam, J. N. Blattman, D. L. Barber, and R. Ahmed. 2007. Molecular signature of CD8+ T cell exhaustion during chronic viral infection. *Immunity* 27: 670-684.

26. Barber, D. L., E. J. Wherry, D. Masopust, B. Zhu, J. P. Allison, A. H. Sharpe, G. J. Freeman, and R. Ahmed. 2006. Restoring function in exhausted CD8 T cells during chronic viral infection. *Nature* 439: 682-687.

27. Tinoco, R., V. Alcalde, Y. Yang, K. Sauer, and E. I. Zuniga. 2009. Cell-intrinsic transforming growth factor-beta signaling mediates virus-specific CD8+ T cell deletion and viral persistence in vivo. *Immunity* 31: 145-157.

28. Tinoco, R., F. Carrette, M. L. Barraza, D. C. Otero, J. Magaña, M. W. Bosenberg, S. L. Swain, and L. M. Bradley. 2016. PSGL-1 Is an Immune Checkpoint Regulator that Promotes T Cell Exhaustion. *Immunity* 44: 1190-1203.

29. Doedens, A. L., A. T. Phan, M. H. Stradner, J. K. Fujimoto, J. V. Nguyen, E. Yang, R. S. Johnson, and A. W. Goldrath. 2013. Hypoxia-inducible factors enhance the effector responses of CD8(+) T cells to persistent antigen. *Nat Immunol* 14: 1173-1182.

30. Odorizzi, P. M., K. E. Pauken, M. A. Paley, A. Sharpe, and E. J. Wherry. 2015. Genetic absence of PD-1 promotes accumulation of terminally differentiated exhausted CD8+ T cells. *J Exp Med* 212: 1125-1137.

31. Doering, T. A., A. Crawford, J. M. Angelosanto, M. A. Paley, C. G. Ziegler, and E. J. Wherry. 2012. Network analysis reveals centrally connected genes and pathways involved in CD8+ T cell exhaustion versus memory. *Immunity* 37: 1130-1144.

32. Pauken, K. E., M. A. Sammons, P. M. Odorizzi, S. Manne, J. Godec, O. Khan, A. M. Drake, Z. Chen, D. R. Sen, M. Kurachi, R. A. Barnitz, C. Bartman, B. Bengsch, A. C. Huang, J. M. Schenkel, G. Vahedi, W. N. Haining, S. L. Berger, and E. J. Wherry. 2016. Epigenetic stability of exhausted T cells limits durability of reinvigoration by PD-1 blockade. *Science* 354: 1160-1165.

33. Sen, D. R., J. Kaminski, R. A. Barnitz, M. Kurachi, U. Gerdemann, K. B. Yates, H. W. Tsao, J. Godec, M. W. LaFleur, F. D. Brown, P. Tonnerre, R. T. Chung, D. C. Tully, T. M. Allen, N. Frahm, G. M. Lauer, E. J. Wherry, N. Yosef, and W. N. Haining. 2016. The epigenetic landscape of T cell exhaustion. *Science* 354: 1165-1169.

34. Zander, R., D. Schauder, G. Xin, C. Nguyen, X. Wu, A. Zajac, and W. Cui. 2019. CD4. *Immunity* 51: 1028-1042.e1024.

35. Hudson, W. H., J. Gensheimer, M. Hashimoto, A. Wieland, R. M. Valanparambil, P. Li, J. X. Lin, B. T. Konieczny, S. J. Im, G. J. Freeman, W. J. Leonard, H. T. Kissick, and R. Ahmed. 2019. Proliferating Transitory T Cells with an Effector-like Transcriptional Signature Emerge from PD-1. *Immunity* 51: 1043-1058.e1044.

36. Chen, Z., Z. Ji, S. F. Ngiow, S. Manne, Z. Cai, A. C. Huang, J. Johnson, R. P. Staupe, B. Bengsch, C. Xu, S. Yu, M. Kurachi, R. S. Herati, L. A. Vella, A. E. Baxter, J. E. Wu, O.

Khan, J. C. Beltra, J. R. Giles, E. Stelekati, L. M. McLane, C. W. Lau, X. Yang, S. L. Berger, G. Vahedi, H. Ji, and E. J. Wherry. 2019. TCF-1-Centered Transcriptional Network Drives an Effector versus Exhausted CD8 T Cell-Fate Decision. *Immunity* 51: 840-855.e845.

37. Utzschneider, D. T., M. Charmoy, V. Chennupati, L. Pousse, D. P. Ferreira, S. Calderon-Copete, M. Danilo, F. Alfei, M. Hofmann, D. Wieland, S. Pradervand, R. Thimme, D. Zehn, and W. Held. 2016. T Cell Factor 1-Expressing Memory-like CD8(+) T Cells Sustain the Immune Response to Chronic Viral Infections. *Immunity* 45: 415-427.

38. Im, S. J., M. Hashimoto, M. Y. Gerner, J. Lee, H. T. Kissick, M. C. Burger, Q. Shan, J. S. Hale, T. H. Nasti, A. H. Sharpe, G. J. Freeman, R. N. Germain, H. I. Nakaya, H. H. Xue, and R. Ahmed. 2016. Defining CD8+ T cells that provide the proliferative burst after PD-1 therapy. *Nature* 537: 417-421.

39. Wu, T., Y. Ji, E. A. Moseman, H. C. Xu, M. Manglani, M. Kirby, S. M. Anderson, R. Handon, E. Kenyon, A. Elkahloun, W. Wu, P. A. Lang, L. Gattinoni, D. B. McGavern, and P. L. Schwartzberg. 2016. The TCF1-Bcl6 axis counteracts type I interferon to repress exhaustion and maintain T cell stemness. *Sci Immunol* 1.

40. Yao, C., H. W. Sun, N. E. Lacey, Y. Ji, E. A. Moseman, H. Y. Shih, E. F. Heuston, M. Kirby, S. Anderson, J. Cheng, O. Khan, R. Handon, J. Reilley, J. Fioravanti, J. Hu, S. Gossa, E. J. Wherry, L. Gattinoni, D. B. McGavern, J. J. O'Shea, P. L. Schwartzberg, and T. Wu. 2019. Single-cell RNA-seq reveals TOX as a key regulator of CD8. *Nat Immunol* 20: 890-901.

41. Beltra, J. C., S. Manne, M. S. Abdel-Hakeem, M. Kurachi, J. R. Giles, Z. Chen, V. Casella, S. F. Ngiow, O. Khan, Y. J. Huang, P. Yan, K. Nzingha, W. Xu, R. K. Amaravadi, X. Xu, G. C. Karakousis, T. C. Mitchell, L. M. Schuchter, A. C. Huang, and E. J. Wherry. 2020. Developmental Relationships of Four Exhausted CD8. *Immunity* 52: 825-841.e828.

42. Walton, S., S. Mandaric, and A. Oxenius. 2013. CD4 T cell responses in latent and chronic viral infections. *Front Immunol* 4: 105.

43. Penaloza-MacMaster, P., D. L. Barber, E. J. Wherry, N. M. Provine, J. E. Teigler, L. Parenteau, S. Blackmore, E. N. Borducchi, R. A. Larocca, K. B. Yates, H. Shen, W. N. Haining, R. Sommerstein, D. D. Pinschewer, R. Ahmed, and D. H. Barouch. 2015. Vaccine-elicited CD4 T cells induce immunopathology after chronic LCMV infection. *Science* 347: 278-282.

44. Oxenius, A., R. M. Zinkernagel, and H. Hengartner. 1998. Comparison of activation versus induction of unresponsiveness of virus-specific CD4+ and CD8+ T cells upon acute versus persistent viral infection. *Immunity* 9: 449-457.

45. Doherty, P. C., S. Hou, and P. J. Southern. 1993. Lymphocytic choriomeningitis virus induces a chronic wasting disease in mice lacking class I major histocompatibility complex glycoproteins. *J Neuroimmunol* 46: 11-17.

46. Stamm, A., L. Valentine, R. Potts, and M. Premenko-Lanier. 2012. An intermediate dose of LCMV clone 13 causes prolonged morbidity that is maintained by CD4+ T cells. *Virology* 425: 122-132.

47. Crawford, A., J. M. Angelosanto, C. Kao, T. A. Doering, P. M. Odorizzi, B. E. Barnett, and E. J. Wherry. 2014. Molecular and transcriptional basis of $CD4^+$ T cell dysfunction during chronic infection. *Immunity* 40: 289-302.

48. Elsaesser, H., K. Sauer, and D. G. Brooks. 2009. IL-21 is required to control chronic viral infection. *Science* 324: 1569-1572.

49. Johnston, R. J., A. C. Poholek, D. DiToro, I. Yusuf, D. Eto, B. Barnett, A. L. Dent, J. Craft, and S. Crotty. 2009. Bcl6 and Blimp-1 are reciprocal and antagonistic regulators of T follicular helper cell differentiation. *Science* 325: 1006-1010.

50. Getnet, D., J. F. Grosso, M. V. Goldberg, T. J. Harris, H. R. Yen, T. C. Bruno, N. M. Durham, E. L. Hipkiss, K. J. Pyle, S. Wada, F. Pan, D. M. Pardoll, and C. G. Drake. 2010. A role for the transcription factor Helios in human CD4(+)CD25(+) regulatory T cells. *Mol Immunol* 47: 1595-1600.

51. Lewis, G. M., E. J. Wehrens, L. Labarta-Bajo, H. Streeck, and E. I. Zuniga. 2016. TGF-β receptor maintains CD4 T helper cell identity during chronic viral infections. *J Clin Invest* 126: 3799-3813.

52. Wehrens, E. J., K. A. Wong, A. Gupta, A. Khan, C. A. Benedict, and E. I. Zuniga. 2018. IL-27 regulates the number, function and cytotoxic program of antiviral CD4 T cells and promotes cytomegalovirus persistence. *PLoS One* 13: e0201249.

53. Curran, M. A., T. L. Geiger, W. Montalvo, M. Kim, S. L. Reiner, A. Al-Shamkhani, J. C. Sun, and J. P. Allison. 2013. Systemic 4-1BB activation induces a novel T cell phenotype driven by high expression of Eomesodermin. *J Exp Med* 210: 743-755.

54. Harker, J. A., G. M. Lewis, L. Mack, and E. I. Zuniga. 2011. Late interleukin-6 escalates T follicular helper cell responses and controls a chronic viral infection. *Science* 334: 825-829.

55. Greczmiel, U., N. J. Kräutler, A. Pedrioli, I. Bartsch, P. Agnellini, G. Bedenikovic, J. Harker, K. Richter, and A. Oxenius. 2017. Sustained T follicular helper cell response is essential for control of chronic viral infection. *Sci Immunol* 2.

56. Belkaid, Y., and O. J. Harrison. 2017. Homeostatic Immunity and the Microbiota. *Immunity* 46: 562-576.

57. Rooks, M. G., and W. S. Garrett. 2016. Gut microbiota, metabolites and host immunity. *Nat Rev Immunol* 16: 341-352.

58. Odenwald, M. A., and J. R. Turner. 2017. The intestinal epithelial barrier: a therapeutic target? *Nat Rev Gastroenterol Hepatol* 14: 9-21.

59. Peterson, L. W., and D. Artis. 2014. Intestinal epithelial cells: regulators of barrier function and immune homeostasis. *Nat Rev Immunol* 14: 141-153.

60. Buckley, A., and J. R. Turner. 2018. Cell Biology of Tight Junction Barrier Regulation and Mucosal Disease. *Cold Spring Harb Perspect Biol* 10.

61. Graham, W. V., W. He, A. M. Marchiando, J. Zha, G. Singh, H. S. Li, A. Biswas, M. L. D. M. Ong, Z. H. Jiang, W. Choi, H. Zuccola, Y. Wang, J. Griffith, J. Wu, H. J. Rosenberg, S. B. Snapper, D. Ostrov, S. C. Meredith, L. W. Miller, and J. R. Turner. 2019. Intracellular MLCK1 diversion reverses barrier loss to restore mucosal homeostasis. *Nat Med* 25: 690-700.

62. Su, L., S. C. Nalle, L. Shen, E. S. Turner, G. Singh, L. A. Breskin, E. A. Khramtsova, G. Khramtsova, P. Y. Tsai, Y. X. Fu, C. Abraham, and J. R. Turner. 2013. TNFR2 activates MLCK-dependent tight junction dysregulation to cause apoptosis-mediated barrier loss and experimental colitis. *Gastroenterology* 145: 407-415.

63. Weber, C. R., D. R. Raleigh, L. Su, L. Shen, E. A. Sullivan, Y. Wang, and J. R. Turner. 2010. Epithelial myosin light chain kinase activation induces mucosal interleukin-13 expression to alter tight junction ion selectivity. *J Biol Chem* 285: 12037-12046.

64. Turner, J. R. 2009. Intestinal mucosal barrier function in health and disease. *Nat Rev Immunol* 9: 799-809.

65. Shen, L., C. R. Weber, D. R. Raleigh, D. Yu, and J. R. Turner. 2011. Tight junction pore and leak pathways: a dynamic duo. *Annu Rev Physiol* 73: 283-309.

66. Wilairatana, P., J. B. Meddings, M. Ho, S. Vannaphan, and S. Looareesuwan. 1997. Increased gastrointestinal permeability in patients with Plasmodium falciparum malaria. *Clin Infect Dis* 24: 430-435.

67. Ponte, R., V. Mehraj, P. Ghali, A. Couëdel-Courteille, R. Cheynier, and J. P. Routy. 2016. Reversing Gut Damage in HIV Infection: Using Non-Human Primate Models to Instruct Clinical Research. *EBioMedicine* 4: 40-49.

68. Tincati, C., D. C. Douek, and G. Marchetti. 2016. Gut barrier structure, mucosal immunity and intestinal microbiota in the pathogenesis and treatment of HIV infection. *AIDS Res Ther* 13: 19.

69. Brenchley, J. M., D. A. Price, T. W. Schacker, T. E. Asher, G. Silvestri, S. Rao, Z. Kazzaz, E. Bornstein, O. Lambotte, D. Altmann, B. R. Blazar, B. Rodriguez, L. Teixeira-Johnson, A. Landay, J. N. Martin, F. M. Hecht, L. J. Picker, M. M. Lederman, S. G. Deeks, and D. C. Douek. 2006. Microbial translocation is a cause of systemic immune activation in chronic HIV infection. *Nat. Med.* 12: 1365-1371.

70. Estes, J. D., L. D. Harris, N. R. Klatt, B. Tabb, S. Pittaluga, M. Paiardini, G. R. Barclay, J. Smedley, R. Pung, K. M. Oliveira, V. M. Hirsch, G. Silvestri, D. C. Douek, C. J. Miller, A. T. Haase, J. Lifson, and J. M. Brenchley. 2010. Damaged intestinal epithelial integrity linked to microbial translocation in pathogenic simian immunodeficiency virus infections. *PLoS Pathog* 6: e1001052.

71. Groom, J. R., and A. D. Luster. 2011. CXCR3 in T cell function. *Exp Cell Res* 317: 620-631.

72. Beura, L. K., K. G. Anderson, J. M. Schenkel, J. J. Locquiao, K. A. Fraser, V. Vezys, M. Pepper, and D. Masopust. 2015. Lymphocytic choriomeningitis virus persistence promotes effector-like memory differentiation and enhances mucosal T cell distribution. *J Leukoc Biol* 97: 217-225.

73. Coulombe, P. A., and P. Wong. 2004. Cytoplasmic intermediate filaments revealed as dynamic and multipurpose scaffolds. *Nat Cell Biol* 6: 699-706.

74. Trzpis, M., P. M. McLaughlin, L. M. de Leij, and M. C. Harmsen. 2007. Epithelial cell adhesion molecule: more than a carcinoma marker and adhesion molecule. *Am J Pathol* 171: 386-395.

75. Volynets, V., A. Reichold, G. Bardos, A. Rings, A. Bleich, and S. C. Bischoff. 2016. Assessment of the Intestinal Barrier with Five Different Permeability Tests in Healthy C57BL/6J and BALB/cJ Mice. *Dig. Dis. Sci.* 61: 737-746.

76. Subramanian, A., P. Tamayo, V. K. Mootha, S. Mukherjee, B. L. Ebert, M. A. Gillette, A. Paulovich, S. L. Pomeroy, T. R. Golub, E. S. Lander, and J. P. Mesirov. 2005. Gene set enrichment analysis: a knowledge-based approach for interpreting genome-wide expression profiles. *Proc Natl Acad Sci U S A* 102: 15545-15550.

77. Tsai, P. Y., B. Zhang, W. Q. He, J. M. Zha, M. A. Odenwald, G. Singh, A. Tamura, L. Shen, A. Sailer, S. Yeruva, W. T. Kuo, Y. X. Fu, S. Tsukita, and J. R. Turner. 2017. IL-22 Upregulates Epithelial Claudin-2 to Drive Diarrhea and Enteric Pathogen Clearance. *Cell Host Microbe* 21: 671-681.e674.

78. Liberzon, A., A. Subramanian, R. Pinchback, H. Thorvaldsdóttir, P. Tamayo, and J. P. Mesirov. 2011. Molecular signatures database (MSigDB) 3.0. *Bioinformatics* 27: 1739-1740.

79. Kanehisa, M., and S. Goto. 2000. KEGG: kyoto encyclopedia of genes and genomes. *Nucleic Acids Res* 28: 27-30.

80. Fabregat, A., S. Jupe, L. Matthews, K. Sidiropoulos, M. Gillespie, P. Garapati, R. Haw, B. Jassal, F. Korninger, B. May, M. Milacic, C. D. Roca, K. Rothfels, C. Sevilla, V. Shamovsky, S. Shorser, T. Varusai, G. Viteri, J. Weiser, G. Wu, L. Stein, H. Hermjakob, and P. D'Eustachio. 2018. The Reactome Pathway Knowledgebase. *Nucleic Acids Res* 46: D649-D655.

81. Sagné, C., C. Agulhon, P. Ravassard, M. Darmon, M. Hamon, S. El Mestikawy, B. Gasnier, and B. Giros. 2001. Identification and characterization of a lysosomal transporter for small neutral amino acids. *Proc Natl Acad Sci U S A* 98: 7206-7211.

82. Wheeler, T. J., and P. C. Hinkle. 1985. The glucose transporter of mammalian cells. *Annu Rev Physiol* 47: 503-517.

83. Pathak, B. G., G. E. Shull, N. A. Jenkins, and N. G. Copeland. 1996. Mouse chromosomal location of four Na/H exchanger isoform genes. *Genomics* 31: 261-263.

84. Qiu, A., S. H. Min, M. Jansen, U. Malhotra, E. Tsai, D. C. Cabelof, L. H. Matherly, R. Zhao, M. H. Akabas, and I. D. Goldman. 2007. Rodent intestinal folate transporters (SLC46A1): secondary structure, functional properties, and response to dietary folate restriction. *Am J Physiol Cell Physiol* 293: C1669-1678.

85. Liang, R., Y. J. Fei, P. D. Prasad, S. Ramamoorthy, H. Han, T. L. Yang-Feng, M. A. Hediger, V. Ganapathy, and F. H. Leibach. 1995. Human intestinal H+/peptide cotransporter. Cloning, functional expression, and chromosomal localization. *J Biol Chem* 270: 6456-6463.

86. Mukherjee, S., H. Zheng, M. G. Derebe, K. M. Callenberg, C. L. Partch, D. Rollins, D. C. Propheter, J. Rizo, M. Grabe, Q. X. Jiang, and L. V. Hooper. 2014. Antibacterial membrane attack by a pore-forming intestinal C-type lectin. *Nature* 505: 103-107.

87. Miki, T., O. Holst, and W. D. Hardt. 2012. The bactericidal activity of the C-type lectin RegIIIβ against Gram-negative bacteria involves binding to lipid A. *J Biol Chem* 287: 34844-34855.

88. Molofsky, A. B., A. K. Savage, and R. M. Locksley. 2015. Interleukin-33 in Tissue Homeostasis, Injury, and Inflammation. *Immunity* 42: 1005-1019.

89. Wilson, E. B., D. H. Yamada, H. Elsaesser, J. Herskovitz, J. Deng, G. Cheng, B. J. Aronow, C. L. Karp, and D. G. Brooks. 2013. Blockade of chronic type I interferon signaling to control persistent LCMV infection. *Science* 340: 202-207.

90. Teijaro, J. R., C. Ng, A. M. Lee, B. M. Sullivan, K. C. Sheehan, M. Welch, R. D. Schreiber, J. C. de la Torre, and M. B. Oldstone. 2013. Persistent LCMV infection is controlled by blockade of type I interferon signaling. *Science* 340: 207-211.

91. Sumagin, R., A. Z. Robin, A. Nusrat, and C. A. Parkos. 2014. Transmigrated neutrophils in the intestinal lumen engage ICAM-1 to regulate the epithelial barrier and neutrophil recruitment. *Mucosal Immunol* 7: 905-915.

92. Stanley, E. R., D. M. Chen, and H. S. Lin. 1978. Induction of macrophage production and proliferation by a purified colony stimulating factor. *Nature* 274: 168-170.

93. Swiecki, M., and M. Colonna. 2011. Type I interferons: diversity of sources, production pathways and effects on immune responses. *Curr Opin Virol* 1: 463-475.

94. Dorhoi, A., V. Yeremeev, G. Nouailles, J. Weiner, S. Jörg, E. Heinemann, D. Oberbeck-Müller, J. K. Knaul, A. Vogelzang, S. T. Reece, K. Hahnke, H. J. Mollenkopf, V. Brinkmann, and S. H. Kaufmann. 2014. Type I IFN signaling triggers immunopathology in tuberculosis-susceptible mice by modulating lung phagocyte dynamics. *Eur J Immunol* 44: 2380-2393.

95. Shahangian, A., E. K. Chow, X. Tian, J. R. Kang, A. Ghaffari, S. Y. Liu, J. A. Belperio, G. Cheng, and J. C. Deng. 2009. Type I IFNs mediate development of postinfluenza bacterial pneumonia in mice. *J Clin Invest* 119: 1910-1920.

96. Abe, K., K. P. Nguyen, S. D. Fine, J. H. Mo, C. Shen, S. Shenouda, M. Corr, S. Jung, J. Lee, L. Eckmann, and E. Raz. 2007. Conventional dendritic cells regulate the outcome of colonic inflammation independently of T cells. *Proc. Natl. Acad. Sci. U.S.A.* 104: 17022-17027.

97. Neil, J. A., Y. Matsuzawa-Ishimoto, E. Kernbauer-Hölzl, S. L. Schuster, S. Sota, M. Venzon, S. Dallari, A. Galvao Neto, A. Hine, D. Hudesman, P. Loke, T. J. Nice, and K. Cadwell. 2019. IFN-I and IL-22 mediate protective effects of intestinal viral infection. *Nat Microbiol* 4: 1737-1749.

98. Oxenius, A., M. F. Bachmann, P. G. Ashton-Rickardt, S. Tonegawa, R. M. Zinkernagel, and H. Hengartner. 1995. Presentation of endogenous viral proteins in association with major histocompatibility complex class II: on the role of intracellular compartmentalization, invariant chain and the TAP transporter system. *Eur J Immunol* 25: 3402-3411.

99. Homann, D., H. Lewicki, D. Brooks, J. Eberlein, V. Mallet-Designé, L. Teyton, and M. B. Oldstone. 2007. Mapping and restriction of a dominant viral CD4+ T cell core epitope by both MHC class I and MHC class II. *Virology* 363: 113-123.

100. Angelosanto, J. M., S. D. Blackburn, A. Crawford, and E. J. Wherry. 2012. Progressive loss of memory T cell potential and commitment to exhaustion during chronic viral infection. *J Virol* 86: 8161-8170.

101. Thaiss, C. A., M. Levy, I. Grosheva, D. Zheng, E. Soffer, E. Blacher, S. Braverman, A. C. Tengeler, O. Barak, M. Elazar, R. Ben-Zeev, D. Lehavi-Regev, M. N. Katz, M. Pevsner-Fischer, A. Gertler, Z. Halpern, A. Harmelin, S. Aamar, P. Serradas, A. Grosfeld, H. Shapiro, B. Geiger, and E. Elinav. 2018. Hyperglycemia drives intestinal barrier dysfunction and risk for enteric infection. *Science* 359: 1376-1383.

102. Martinez-Medina, M., J. Denizot, N. Dreux, F. Robin, E. Billard, R. Bonnet, A. Darfeuille-Michaud, and N. Barnich. 2014. Western diet induces dysbiosis with increased E coli in CEABAC10 mice, alters host barrier function favouring AIEC colonisation. *Gut* 63: 116-124.

103. Harbison, J. E., A. J. Roth-Schulze, L. C. Giles, C. D. Tran, K. M. Ngui, M. A. Penno, R. L. Thomson, J. M. Wentworth, P. G. Colman, M. E. Craig, G. Morahan, A. T. Papenfuss, S. C. Barry, L. C. Harrison, and J. J. Couper. 2019. Gut microbiome dysbiosis and increased intestinal permeability in children with islet autoimmunity and type 1 diabetes: A prospective cohort study. *Pediatr Diabetes* 20: 574-583.

104. Tanca, A., V. Manghina, C. Fraumene, A. Palomba, M. Abbondio, M. Deligios, M. Silverman, and S. Uzzau. 2017. Metaproteogenomics Reveals Taxonomic and Functional Changes between Cecal and Fecal Microbiota in Mouse. *Front Microbiol* 8: 391.

105. Shannon, C. E. 1997. The mathematical theory of communication. 1963. *MD Comput* 14: 306-317.

106. Morton, J. T., C. Marotz, A. Washburne, J. Silverman, L. S. Zaramela, A. Edlund, K. Zengler, and R. Knight. 2019. Establishing microbial composition measurement standards with reference frames. *Nat Commun* 10: 2719.

107. Wyatt, J., H. Vogelsang, W. Hübl, T. Waldhöer, and H. Lochs. 1993. Intestinal permeability and the prediction of relapse in Crohn's disease. *Lancet* 341: 1437-1439.

108. D'Incà, R., V. Di Leo, G. Corrao, D. Martines, A. D'Odorico, C. Mestriner, C. Venturi, G. Longo, and G. C. Sturniolo. 1999. Intestinal permeability test as a predictor of clinical course in Crohn's disease. *Am J Gastroenterol* 94: 2956-2960.

109. Tibble, J. A., G. Sigthorsson, S. Bridger, M. K. Fagerhol, and I. Bjarnason. 2000. Surrogate markers of intestinal inflammation are predictive of relapse in patients with inflammatory bowel disease. *Gastroenterology* 119: 15-22.

110. Sturgeon, C., J. Lan, and A. Fasano. 2017. Zonulin transgenic mice show altered gut permeability and increased morbidity/mortality in the DSS colitis model. *Ann N Y Acad Sci* 1397: 130-142.

111. Conlin, V. S., X. Wu, C. Nguyen, C. Dai, B. A. Vallance, A. M. Buchan, L. Boyer, and K. Jacobson. 2009. Vasoactive intestinal peptide ameliorates intestinal barrier disruption associated with Citrobacter rodentium-induced colitis. *Am J Physiol Gastrointest Liver Physiol* 297: G735-750.

112. Machiels, K., M. Joossens, J. Sabino, V. De Preter, I. Arijs, V. Eeckhaut, V. Ballet, K. Claes, F. Van Immerseel, K. Verbeke, M. Ferrante, J. Verhaegen, P. Rutgeerts, and S. Vermeire. 2014. A decrease of the butyrate-producing species Roseburia hominis and

Faecalibacterium prausnitzii defines dysbiosis in patients with ulcerative colitis. *Gut* 63: 1275-1283.

113. Hedin, C. R., N. E. McCarthy, P. Louis, F. M. Farquharson, S. McCartney, K. Taylor, N. J. Prescott, T. Murrells, A. J. Stagg, K. Whelan, and J. O. Lindsay. 2014. Altered intestinal microbiota and blood T cell phenotype are shared by patients with Crohn's disease and their unaffected siblings. *Gut* 63: 1578-1586.

114. Mancabelli, L., C. Milani, G. A. Lugli, F. Turroni, D. Cocconi, D. van Sinderen, and M. Ventura. 2017. Identification of universal gut microbial biomarkers of common human intestinal diseases by meta-analysis. *FEMS Microbiol Ecol* 93.

115. Okayasu, I., S. Hatakeyama, M. Yamada, T. Ohkusa, Y. Inagaki, and R. Nakaya. 1990. A novel method in the induction of reliable experimental acute and chronic ulcerative colitis in mice. *Gastroenterology* 98: 694-702.

116. Eichele, D. D., and K. K. Kharbanda. 2017. Dextran sodium sulfate colitis murine model: An indispensable tool for advancing our understanding of inflammatory bowel diseases pathogenesis. *World J Gastroenterol* 23: 6016-6029.

117. Schauer, D. B., B. A. Zabel, I. F. Pedraza, C. M. O'Hara, A. G. Steigerwalt, and D. J. Brenner. 1995. Genetic and biochemical characterization of Citrobacter rodentium sp. nov. *J Clin Microbiol* 33: 2064-2068.

118. Bouladoux, N., O. J. Harrison, and Y. Belkaid. 2017. The Mouse Model of Infection with Citrobacter rodentium. *Curr Protoc Immunol* 119: 19.15.11-19.15.25.

119. Matloubian, M., S. R. Kolhekar, T. Somasundaram, and R. Ahmed. 1993. Molecular determinants of macrophage tropism and viral persistence: importance of single amino acid changes in the polymerase and glycoprotein of lymphocytic choriomeningitis virus. *J Virol* 67: 7340-7349.

120. Sevilla, N., S. Kunz, A. Holz, H. Lewicki, D. Homann, H. Yamada, K. P. Campbell, J. C. de La Torre, and M. B. Oldstone. 2000. Immunosuppression and resultant viral persistence by specific viral targeting of dendritic cells. *J Exp Med* 192: 1249-1260.

121. Macal, M., G. M. Lewis, S. Kunz, R. Flavell, J. A. Harker, and E. I. Zuniga. 2012. Plasmacytoid dendritic cells are productively infected and activated through TLR-7 early after arenavirus infection. *Cell Host Microbe* 11: 617-630.

122. Mahanty, S., K. Hutchinson, S. Agarwal, M. McRae, P. E. Rollin, and B. Pulendran. 2003. Cutting edge: impairment of dendritic cells and adaptive immunity by Ebola and Lassa viruses. *J Immunol* 170: 2797-2801.

123. Pinchuk, I. V., R. C. Mifflin, J. I. Saada, and D. W. Powell. 2010. Intestinal mesenchymal cells. *Curr Gastroenterol Rep* 12: 310-318.

124. Mueller, S. N., M. Matloubian, D. M. Clemens, A. H. Sharpe, G. J. Freeman, S. Gangappa, C. P. Larsen, and R. Ahmed. 2007. Viral targeting of fibroblastic reticular cells contributes to immunosuppression and persistence during chronic infection. *Proc Natl Acad Sci U S A* 104: 15430-15435.

125. Warner, N. L., J. D. Jokinen, J. I. Beier, K. J. Sokoloski, and I. S. Lukashevich. 2018. Mammarenaviral Infection Is Dependent on Directional Exposure to and Release from Polarized Intestinal Epithelia. *Viruses* 10.

126. Marchetti, G., G. M. Bellistrì, E. Borghi, C. Tincati, S. Ferramosca, M. La Francesca, G. Morace, A. Gori, and A. D. Monforte. 2008. Microbial translocation is associated with sustained failure in CD4+ T-cell reconstitution in HIV-infected patients on long-term highly active antiretroviral therapy. *AIDS* 22: 2035-2038.

127. Shin, K., S. Straight, and B. Margolis. 2005. PATJ regulates tight junction formation and polarity in mammalian epithelial cells. *J Cell Biol* 168: 705-711.

128. Cherradi, S., P. Martineau, C. Gongora, and M. Del Rio. 2019. Claudin gene expression profiles and clinical value in colorectal tumors classified according to their molecular subtype. *Cancer Manag Res* 11: 1337-1348.

129. Soler, A. P., R. D. Miller, K. V. Laughlin, N. Z. Carp, D. M. Klurfeld, and J. M. Mullin. 1999. Increased tight junctional permeability is associated with the development of colon cancer. *Carcinogenesis* 20: 1425-1431.

130. Lei, Z., T. Maeda, A. Tamura, T. Nakamura, Y. Yamazaki, H. Shiratori, K. Yashiro, S. Tsukita, and H. Hamada. 2012. EpCAM contributes to formation of functional tight junction in the intestinal epithelium by recruiting claudin proteins. *Dev Biol* 371: 136-145.

131. Patel, R. M., L. S. Myers, A. R. Kurundkar, A. Maheshwari, A. Nusrat, and P. W. Lin. 2012. Probiotic bacteria induce maturation of intestinal claudin 3 expression and barrier function. *Am J Pathol* 180: 626-635.

132. Yu, A. S., A. H. Enck, W. I. Lencer, and E. E. Schneeberger. 2003. Claudin-8 expression in Madin-Darby canine kidney cells augments the paracellular barrier to cation permeation. *J Biol Chem* 278: 17350-17359.

133. Venkatesh, M., S. Mukherjee, H. Wang, H. Li, K. Sun, A. P. Benechet, Z. Qiu, L. Maher, M. R. Redinbo, R. S. Phillips, J. C. Fleet, S. Kortagere, P. Mukherjee, A. Fasano, J. Le Ven, J. K. Nicholson, M. E. Dumas, K. M. Khanna, and S. Mani. 2014. Symbiotic bacterial metabolites regulate gastrointestinal barrier function via the xenobiotic sensor PXR and Toll-like receptor 4. *Immunity* 41: 296-310.

134. Sun, L., H. Miyoshi, S. Origanti, T. J. Nice, A. C. Barger, N. A. Manieri, L. A. Fogel, A. R. French, D. Piwnica-Worms, H. Piwnica-Worms, H. W. Virgin, D. J. Lenschow, and T.

S. Stappenbeck. 2015. Type I interferons link viral infection to enhanced epithelial turnover and repair. *Cell Host Microbe* 17: 85-97.

135. Lunt, S. Y., and M. G. Vander Heiden. 2011. Aerobic glycolysis: meeting the metabolic requirements of cell proliferation. *Annu Rev Cell Dev Biol* 27: 441-464.

136. Harris, L. D., B. Tabb, D. L. Sodora, M. Paiardini, N. R. Klatt, D. C. Douek, G. Silvestri, M. Müller-Trutwin, I. Vasile-Pandrea, C. Apetrei, V. Hirsch, J. Lifson, J. M. Brenchley, and J. D. Estes. 2010. Downregulation of robust acute type I interferon responses distinguishes nonpathogenic simian immunodeficiency virus (SIV) infection of natural hosts from pathogenic SIV infection of rhesus macaques. *J Virol* 84: 7886-7891.

137. Bosinger, S. E., Q. Li, S. N. Gordon, N. R. Klatt, L. Duan, L. Xu, N. Francella, A. Sidahmed, A. J. Smith, E. M. Cramer, M. Zeng, D. Masopust, J. V. Carlis, L. Ran, T. H. Vanderford, M. Paiardini, R. B. Isett, D. A. Baldwin, J. G. Else, S. I. Staprans, G. Silvestri, A. T. Haase, and D. J. Kelvin. 2009. Global genomic analysis reveals rapid control of a robust innate response in SIV-infected sooty mangabeys. *J Clin Invest* 119: 3556-3572.

138. Canesso, M. C. C., L. Lemos, T. C. Neves, F. M. Marim, T. B. R. Castro, É. Veloso, C. P. Queiroz, J. Ahn, H. C. Santiago, F. S. Martins, J. Alves-Silva, E. Ferreira, D. C. Cara, A. T. Vieira, G. N. Barber, S. C. Oliveira, and A. M. C. Faria. 2018. The cytosolic sensor STING is required for intestinal homeostasis and control of inflammation. *Mucosal Immunol* 11: 820-834.

139. Jostins, L., S. Ripke, R. K. Weersma, R. H. Duerr, D. P. McGovern, K. Y. Hui, J. C. Lee, L. P. Schumm, Y. Sharma, C. A. Anderson, J. Essers, M. Mitrovic, K. Ning, I. Cleynen, E. Theatre, S. L. Spain, S. Raychaudhuri, P. Goyette, Z. Wei, C. Abraham, J. P. Achkar, T. Ahmad, L. Amininejad, A. N. Ananthakrishnan, V. Andersen, J. M. Andrews, L. Baidoo, T. Balschun, P. A. Bampton, A. Bitton, G. Boucher, S. Brand, C. Büning, A. Cohain, S. Cichon, M. D'Amato, D. De Jong, K. L. Devaney, M. Dubinsky, C. Edwards, D. Ellinghaus, L. R. Ferguson, D. Franchimont, K. Fransen, R. Gearry, M. Georges, C. Gieger, J. Glas, T. Haritunians, A. Hart, C. Hawkey, M. Hedl, X. Hu, T. H. Karlsen, L. Kupcinskas, S. Kugathasan, A. Latiano, D. Laukens, I. C. Lawrance, C. W. Lees, E. Louis, G. Mahy, J. Mansfield, A. R. Morgan, C. Mowat, W. Newman, O. Palmieri, C. Y. Ponsioen, U. Potocnik, N. J. Prescott, M. Regueiro, J. I. Rotter, R. K. Russell, J. D. Sanderson, M. Sans, J. Satsangi, S. Schreiber, L. A. Simms, J. Sventoraityte, S. R. Targan, K. D. Taylor, M. Tremelling, H. W. Verspaget, M. De Vos, C. Wijmenga, D. C. Wilson, J. Winkelmann, R. J. Xavier, S. Zeissig, B. Zhang, C. K. Zhang, H. Zhao, M. S. Silverberg, V. Annese, H. Hakonarson, S. R. Brant, G. Radford-Smith, C. G. Mathew, J. D. Rioux, E. E. Schadt, M. J. Daly, A. Franke, M. Parkes, S. Vermeire, J. C. Barrett, J. H. Cho, and I. I. G. C. (IIBDGC). 2012. Host-microbe interactions have shaped the genetic architecture of inflammatory bowel disease. *Nature* 491: 119-124.

140. Kolumam, G. A., S. Thomas, L. J. Thompson, J. Sprent, and K. Murali-Krishna. 2005. Type I interferons act directly on CD8 T cells to allow clonal expansion and memory formation in response to viral infection. *J Exp Med* 202: 637-650.

141. Nguyen, K. B., W. T. Watford, R. Salomon, S. R. Hofmann, G. C. Pien, A. Morinobu, M. Gadina, J. J. O'Shea, and C. A. Biron. 2002. Critical role for STAT4 activation by type 1 interferons in the interferon-gamma response to viral infection. *Science* 297: 2063-2066.

142. Veazey, R. S., M. DeMaria, L. V. Chalifoux, D. E. Shvetz, D. R. Pauley, H. L. Knight, M. Rosenzweig, R. P. Johnson, R. C. Desrosiers, and A. A. Lackner. 1998. Gastrointestinal tract as a major site of CD4+ T cell depletion and viral replication in SIV infection. *Science* 280: 427-431.

143. Schmitz, J. E., R. S. Veazey, M. J. Kuroda, D. B. Levy, A. Seth, K. G. Mansfield, C. E. Nickerson, M. A. Lifton, X. Alvarez, A. A. Lackner, and N. L. Letvin. 2001. Simian immunodeficiency virus (SIV)-specific cytotoxic T lymphocytes in gastrointestinal tissues of chronically SIV-infected rhesus monkeys. *Blood* 98: 3757-3761.

144. Allers, K., A. Puyskens, H. J. Epple, D. Schürmann, J. Hofmann, V. Moos, and T. Schneider. 2016. The effect of timing of antiretroviral therapy on CD4+ T-cell reconstitution in the intestine of HIV-infected patients. *Mucosal Immunol* 9: 265-274.

145. Shacklett, B. L., C. A. Cox, J. K. Sandberg, N. H. Stollman, M. A. Jacobson, and D. F. Nixon. 2003. Trafficking of human immunodeficiency virus type 1-specific CD8+ T cells to gut-associated lymphoid tissue during chronic infection. *J Virol* 77: 5621-5631.

146. Allers, K., A. Puyskens, H. J. Epple, D. Schürmann, J. Hofmann, V. Moos, and T. Schneider. 2017. Distribution and Activation of CD8+ T Cells in the Duodenal Mucosa before and after HIV Seroconversion. *J Immunol* 198: 481-491.

147. Abt, M. C., L. C. Osborne, L. A. Monticelli, T. A. Doering, T. Alenghat, G. F. Sonnenberg, M. A. Paley, M. Antenus, K. L. Williams, J. Erikson, E. J. Wherry, and D. Artis. 2012. Commensal bacteria calibrate the activation threshold of innate antiviral immunity. *Immunity* 37: 158-170.

148. Mullineaux-Sanders, C., J. Sanchez-Garrido, E. G. D. Hopkins, A. R. Shenoy, R. Barry, and G. Frankel. 2019. Citrobacter rodentium-host-microbiota interactions: immunity, bioenergetics and metabolism. *Nat Rev Microbiol* 17: 701-715.

149. Desai, M. S., A. M. Seekatz, N. M. Koropatkin, N. Kamada, C. A. Hickey, M. Wolter, N. A. Pudlo, S. Kitamoto, N. Terrapon, A. Muller, V. B. Young, B. Henrissat, P. Wilmes, T. S. Stappenbeck, G. Núñez, and E. C. Martens. 2016. A Dietary Fiber-Deprived Gut Microbiota Degrades the Colonic Mucus Barrier and Enhances Pathogen Susceptibility. *Cell* 167: 1339-1353.e1321.

150. Odenwald, M. A., and J. R. Turner. 2013. Intestinal permeability defects: is it time to treat? *Clin Gastroenterol Hepatol* 11: 1075-1083.

151. Bindels, L. B., A. M. Neyrinck, A. Loumaye, E. Catry, H. Walgrave, C. Cherbuy, S. Leclercq, M. Van Hul, H. Plovier, B. Pachikian, L. G. Bermúdez-Humarán, P. Langella, P. D. Cani, J. P. Thissen, and N. M. Delzenne. 2018. Increased gut permeability in cancer cachexia: mechanisms and clinical relevance. *Oncotarget* 9: 18224-18238.

152. Puppa, M. J., J. P. White, S. Sato, M. Cairns, J. W. Baynes, and J. A. Carson. 2011. Gut barrier dysfunction in the Apc(Min/+) mouse model of colon cancer cachexia. *Biochim Biophys Acta* 1812: 1601-1606.

153. Sundstrom, G. M., A. Wahlin, I. Nordin-Andersson, and O. B. Suhr. 1998. Intestinal permeability in patients with acute myeloid leukemia. *Eur. J. Haematol.* 61: 250-254.

154. Dobin, A., C. A. Davis, F. Schlesinger, J. Drenkow, C. Zaleski, S. Jha, P. Batut, M. Chaisson, and T. R. Gingeras. 2013. STAR: ultrafast universal RNA-seq aligner. *Bioinformatics* 29: 15-21.

155. Pertea, M., G. M. Pertea, C. M. Antonescu, T. C. Chang, J. T. Mendell, and S. L. Salzberg. 2015. StringTie enables improved reconstruction of a transcriptome from RNA-seq reads. *Nat Biotechnol* 33: 290-295.

156. Love, M. I., W. Huber, and S. Anders. 2014. Moderated estimation of fold change and dispersion for RNA-seq data with DESeq2. *Genome Biol* 15: 550.

157. Marotz, C., A. Amir, G. Humphrey, J. Gaffney, G. Gogul, and R. Knight. 2017. DNA extraction for streamlined metagenomics of diverse environmental samples. *Biotechniques* 62: 290-293.

158. Caporaso, J. G., C. L. Lauber, W. A. Walters, D. Berg-Lyons, J. Huntley, N. Fierer, S. M. Owens, J. Betley, L. Fraser, M. Bauer, N. Gormley, J. A. Gilbert, G. Smith, and R. Knight. 2012. Ultra-high-throughput microbial community analysis on the Illumina HiSeq and MiSeq platforms. *ISME J* 6: 1621-1624.

159. Gilbert, J. A., J. K. Jansson, and R. Knight. 2014. The Earth Microbiome project: successes and aspirations. *BMC Biol* 12: 69.

160. Gonzalez, A., J. A. Navas-Molina, T. Kosciolek, D. McDonald, Y. Vázquez-Baeza, G. Ackermann, J. DeReus, S. Janssen, A. D. Swafford, S. B. Orchanian, J. G. Sanders, J. Shorenstein, H. Holste, S. Petrus, A. Robbins-Pianka, C. J. Brislawn, M. Wang, J. R. Rideout, E. Bolyen, M. Dillon, J. G. Caporaso, P. C. Dorrestein, and R. Knight. 2018. Qiita: rapid, web-enabled microbiome meta-analysis. *Nat Methods* 15: 796-798.

161. Caporaso, J. G., J. Kuczynski, J. Stombaugh, K. Bittinger, F. D. Bushman, E. K. Costello, N. Fierer, A. G. Peña, J. K. Goodrich, J. I. Gordon, G. A. Huttley, S. T. Kelley, D. Knights, J. E. Koenig, R. E. Ley, C. A. Lozupone, D. McDonald, B. D. Muegge, M. Pirrung, J. Reeder, J. R. Sevinsky, P. J. Turnbaugh, W. A. Walters, J. Widmann, T. Yatsunenko, J.

Zaneveld, and R. Knight. 2010. QIIME allows analysis of high-throughput community sequencing data. *Nat Methods* 7: 335-336.

162. Amir, A., D. McDonald, J. A. Navas-Molina, E. Kopylova, J. T. Morton, Z. Zech Xu, E. P. Kightley, L. R. Thompson, E. R. Hyde, A. Gonzalez, and R. Knight. 2017. Deblur Rapidly Resolves Single-Nucleotide Community Sequence Patterns. *mSystems* 2.

163. Gotelli, N. J., and R. K. Colwell. 2001. Quantifying biodiversity: procedures and pitfalls in the measurement and comparison of species richness. *Ecology Letters* 4: 379-391.

164. Bokulich, N. A., B. D. Kaehler, J. R. Rideout, M. Dillon, E. Bolyen, R. Knight, G. A. Huttley, and J. Gregory Caporaso. 2018. Optimizing taxonomic classification of marker-gene amplicon sequences with QIIME 2's q2-feature-classifier plugin. *Microbiome* 6: 90.

165. DeSantis, T. Z., P. Hugenholtz, N. Larsen, M. Rojas, E. L. Brodie, K. Keller, T. Huber, D. Dalevi, P. Hu, and G. L. Andersen. 2006. Greengenes, a chimera-checked 16S rRNA gene database and workbench compatible with ARB. *Appl Environ Microbiol* 72: 5069-5072.

166. Didion, J. P., M. Martin, and F. S. Collins. 2017. Atropos: specific, sensitive, and speedy trimming of sequencing reads. *PeerJ* 5: e3720.

167. Langmead, B., and S. L. Salzberg. 2012. Fast gapped-read alignment with Bowtie 2. *Nat Methods* 9: 357-359.

168. Hillmann, B., G. A. Al-Ghalith, R. R. Shields-Cutler, Q. Zhu, D. M. Gohl, K. B. Beckman, R. Knight, and D. Knights. 2018. Evaluating the Information Content of Shallow Shotgun Metagenomics. *mSystems* 3.

169. Yona, A. H., I. Frumkin, and Y. Pilpel. 2015. A relay race on the evolutionary adaptation spectrum. *Cell* 163: 549-559.

170. Medzhitov, R., D. S. Schneider, and M. P. Soares. 2012. Disease tolerance as a defense strategy. *Science* 335: 936-941.

171. Oldstone, M. B. A., B. C. Ware, L. E. Horton, M. J. Welch, R. Aiolfi, A. Zarpellon, Z. M. Ruggeri, and B. M. Sullivan. 2018. Lymphocytic choriomeningitis virus Clone 13 infection causes either persistence or acute death dependent on IFN-1, cytotoxic T lymphocytes (CTLs), and host genetics. *Proc Natl Acad Sci U S A* 115: E7814-E7823.

172. Li, Q., P. J. Skinner, S. J. Ha, L. Duan, T. L. Mattila, A. Hage, C. White, D. L. Barber, L. O'Mara, P. J. Southern, C. S. Reilly, J. V. Carlis, C. J. Miller, R. Ahmed, and A. T. Haase. 2009. Visualizing antigen-specific and infected cells in situ predicts outcomes in early viral infection. *Science* 323: 1726-1729.

173. Belkaid, Y., and T. W. Hand. 2014. Role of the microbiota in immunity and inflammation. *Cell* 157: 121-141.

174. Villarino, N. F., G. R. LeCleir, J. E. Denny, S. P. Dearth, C. L. Harding, S. S. Sloan, J. L. Gribble, S. R. Campagna, S. W. Wilhelm, and N. W. Schmidt. 2016. Composition of the gut microbiota modulates the severity of malaria. *Proc Natl Acad Sci U S A* 113: 2235-2240.

175. Khan, N., A. Vidyarthi, S. Nadeem, S. Negi, G. Nair, and J. N. Agrewala. 2016. Alteration in the Gut Microbiota Provokes Susceptibility to Tuberculosis. *Front Immunol* 7: 529.

176. Majlessi, L., F. Sayes, J. F. Bureau, A. Pawlik, V. Michel, G. Jouvion, M. Huerre, M. Severgnini, C. Consolandi, C. Peano, R. Brosch, E. Touati, and C. Leclerc. 2017. Colonization with Helicobacter is concomitant with modified gut microbiota and drastic failure of the immune control of Mycobacterium tuberculosis. *Mucosal Immunol* 10: 1178-1189.

177. Dillon, S. M., D. N. Frank, and C. C. Wilson. 2016. The gut microbiome and HIV-1 pathogenesis: a two-way street. *AIDS* 30: 2737-2751.

178. Inoue, T., J. Nakayama, K. Moriya, H. Kawaratani, R. Momoda, K. Ito, E. Iio, S. Nojiri, K. Fujiwara, M. Yoneda, H. Yoshiji, and Y. Tanaka. 2018. Gut Dysbiosis Associated With Hepatitis C Virus Infection. *Clin Infect Dis* 67: 869-877.

179. Yang, R., Y. Xu, Z. Dai, X. Lin, and H. Wang. 2018. The Immunologic Role of Gut Microbiota in Patients with Chronic HBV Infection. *J Immunol Res* 2018: 2361963.

180. Vujkovic-Cvijin, I., L. A. Swainson, S. N. Chu, A. M. Ortiz, C. A. Santee, A. Petriello, R. M. Dunham, D. W. Fadrosh, D. L. Lin, A. A. Faruqi, Y. Huang, C. Apetrei, I. Pandrea, F. M. Hecht, C. D. Pilcher, N. R. Klatt, J. M. Brenchley, S. V. Lynch, and J. M. McCune. 2015. Gut-Resident Lactobacillus Abundance Associates with IDO1 Inhibition and Th17 Dynamics in SIV-Infected Macaques. *Cell Rep* 13: 1589-1597.

181. Mooney, J. P., K. L. Lokken, M. X. Byndloss, M. D. George, E. M. Velazquez, F. Faber, B. P. Butler, G. T. Walker, M. M. Ali, R. Potts, C. Tiffany, B. M. Ahmer, S. Luckhart, and R. M. Tsolis. 2015. Inflammation-associated alterations to the intestinal microbiota reduce colonization resistance against non-typhoidal Salmonella during concurrent malaria parasite infection. *Sci Rep* 5: 14603.

182. Taniguchi, T., E. Miyauchi, S. Nakamura, M. Hirai, K. Suzue, T. Imai, T. Nomura, T. Handa, H. Okada, C. Shimokawa, R. Onishi, A. Olia, J. Hirata, H. Tomita, H. Ohno, T. Horii, and H. Hisaeda. 2015. Plasmodium berghei ANKA causes intestinal malaria associated with dysbiosis. *Sci Rep* 5: 15699.

183. Wang, J., F. Li, H. Wei, Z. X. Lian, R. Sun, and Z. Tian. 2014. Respiratory influenza virus infection induces intestinal immune injury via microbiota-mediated Th17 cell-dependent inflammation. *J Exp Med* 211: 2397-2410.

184. Groves, H. T., L. Cuthbertson, P. James, M. F. Moffatt, M. J. Cox, and J. S. Tregoning. 2018. Respiratory Disease following Viral Lung Infection Alters the Murine Gut Microbiota. *Front Immunol* 9: 182.

185. Deriu, E., G. M. Boxx, X. He, C. Pan, S. D. Benavidez, L. Cen, N. Rozengurt, W. Shi, and G. Cheng. 2016. Influenza Virus Affects Intestinal Microbiota and Secondary Salmonella Infection in the Gut through Type I Interferons. *PLoS Pathog* 12: e1005572.

186. Lupp, C., M. L. Robertson, M. E. Wickham, I. Sekirov, O. L. Champion, E. C. Gaynor, and B. B. Finlay. 2007. Host-mediated inflammation disrupts the intestinal microbiota and promotes the overgrowth of Enterobacteriaceae. *Cell Host Microbe* 2: 119-129.

187. Gillis, C. C., E. R. Hughes, L. Spiga, M. G. Winter, W. Zhu, T. Furtado de Carvalho, R. B. Chanin, C. L. Behrendt, L. V. Hooper, R. L. Santos, and S. E. Winter. 2018. Dysbiosis-Associated Change in Host Metabolism Generates Lactate to Support Salmonella Growth. *Cell Host Microbe* 23: 54-64.e56.

188. Gu, S., D. Chen, J. N. Zhang, X. Lv, K. Wang, L. P. Duan, Y. Nie, and X. L. Wu. 2013. Bacterial community mapping of the mouse gastrointestinal tract. *PLoS One* 8: e74957.

189. Gallimore, A., A. Glithero, A. Godkin, A. C. Tissot, A. Pluckthun, T. Elliott, H. Hengartner, and R. Zinkernagel. 1998. Induction and exhaustion of lymphocytic choriomeningitis virus-specific cytotoxic T lymphocytes visualized using soluble tetrameric major histocompatibility complex class I-peptide complexes. *J Exp Med* 187: 1383-1393.

190. Mack, I., U. Cuntz, C. Gramer, S. Niedermaier, C. Pohl, A. Schwiertz, K. Zimmermann, S. Zipfel, P. Enck, and J. Penders. 2016. Weight gain in anorexia nervosa does not ameliorate the faecal microbiota, branched chain fatty acid profiles, and gastrointestinal complaints. *Sci Rep* 6: 26752.

191. Mack, I., J. Penders, J. Cook, J. Dugmore, N. Mazurak, and P. Enck. 2018. Is the Impact of Starvation on the Gut Microbiota Specific or Unspecific to Anorexia Nervosa? A Narrative Review Based on a Systematic Literature Search. *Curr Neuropharmacol* 16: 1131-1149.

192. Bindels, L. B., A. M. Neyrinck, S. P. Claus, C. I. Le Roy, C. Grangette, B. Pot, I. Martinez, J. Walter, P. D. Cani, and N. M. Delzenne. 2016. Synbiotic approach restores intestinal homeostasis and prolongs survival in leukaemic mice with cachexia. *ISME J* 10: 1456-1470.

193. Fabbiano, S., N. Suarez-Zamorano, C. Chevalier, V. Lazarevic, S. Kieser, D. Rigo, S. Leo, C. Veyrat-Durebex, N. Gaia, M. Maresca, D. Merkler, M. Gomez de Aguero, A. Macpherson, J. Schrenzel, and M. Trajkovski. 2018. Functional Gut Microbiota Remodeling Contributes to the Caloric Restriction-Induced Metabolic Improvements. *Cell Metab* 28: 907-921 e907.

194. Segata, N., J. Izard, L. Waldron, D. Gevers, L. Miropolsky, W. S. Garrett, and C. Huttenhower. 2011. Metagenomic biomarker discovery and explanation. *Genome Biol* 12: R60.

195. Derrien, M., E. E. Vaughan, C. M. Plugge, and W. M. de Vos. 2004. Akkermansia muciniphila gen. nov., sp. nov., a human intestinal mucin-degrading bacterium. *Int J Syst Evol Microbiol* 54: 1469-1476.

196. Masopust, D., V. Vezys, E. J. Wherry, D. L. Barber, and R. Ahmed. 2006. Cutting edge: gut microenvironment promotes differentiation of a unique memory CD8 T cell population. *J Immunol* 176: 2079-2083.

197. Sheridan, B. S., Q. M. Pham, Y. T. Lee, L. S. Cauley, L. Puddington, and L. Lefrancois. 2014. Oral infection drives a distinct population of intestinal resident memory CD8(+) T cells with enhanced protective function. *Immunity* 40: 747-757.

198. Joshi, N. S., W. Cui, A. Chandele, H. K. Lee, D. R. Urso, J. Hagman, L. Gapin, and S. M. Kaech. 2007. Inflammation directs memory precursor and short-lived effector CD8(+) T cell fates via the graded expression of T-bet transcription factor. *Immunity* 27: 281-295.

199. Plumlee, C. R., J. J. Obar, S. L. Colpitts, E. R. Jellison, W. N. Haining, L. Lefrancois, and K. M. Khanna. 2015. Early Effector CD8 T Cells Display Plasticity in Populating the Short-Lived Effector and Memory-Precursor Pools Following Bacterial or Viral Infection. *Sci Rep* 5: 12264.

200. Kaech, S. M., J. T. Tan, E. J. Wherry, B. T. Konieczny, C. D. Surh, and R. Ahmed. 2003. Selective expression of the interleukin 7 receptor identifies effector CD8 T cells that give rise to long-lived memory cells. *Nat Immunol* 4: 1191-1198.

201. Cruz-Guilloty, F., M. E. Pipkin, I. M. Djuretic, D. Levanon, J. Lotem, M. G. Lichtenheld, Y. Groner, and A. Rao. 2009. Runx3 and T-box proteins cooperate to establish the transcriptional program of effector CTLs. *J Exp Med* 206: 51-59.

202. Gray, S. M., R. A. Amezquita, T. Guan, S. H. Kleinstein, and S. M. Kaech. 2017. Polycomb Repressive Complex 2-Mediated Chromatin Repression Guides Effector CD8(+) T Cell Terminal Differentiation and Loss of Multipotency. *Immunity* 46: 596-608.

203. Kakaradov, B., J. Arsenio, C. E. Widjaja, Z. He, S. Aigner, P. J. Metz, B. Yu, E. J. Wehrens, J. Lopez, S. H. Kim, E. I. Zuniga, A. W. Goldrath, J. T. Chang, and G. W. Yeo. 2017. Early transcriptional and epigenetic regulation of CD8(+) T cell differentiation revealed by single-cell RNA sequencing. *Nat Immunol* 18: 422-432.

204. Everard, A., C. Belzer, L. Geurts, J. P. Ouwerkerk, C. Druart, L. B. Bindels, Y. Guiot, M. Derrien, G. G. Muccioli, N. M. Delzenne, W. M. de Vos, and P. D. Cani. 2013. Cross-talk

between Akkermansia muciniphila and intestinal epithelium controls diet-induced obesity. *Proc Natl Acad Sci U S A* 110: 9066-9071.

205. Bachem, A., C. Makhlouf, K. J. Binger, D. P. de Souza, D. Tull, K. Hochheiser, P. G. Whitney, D. Fernandez-Ruiz, S. Dähling, W. Kastenmüller, J. Jönsson, E. Gressier, A. M. Lew, C. Perdomo, A. Kupz, W. Figgett, F. Mackay, M. Oleshansky, B. E. Russ, I. A. Parish, A. Kallies, M. J. McConville, S. J. Turner, T. Gebhardt, and S. Bedoui. 2019. Microbiota-Derived Short-Chain Fatty Acids Promote the Memory Potential of Antigen-Activated CD8. *Immunity* 51: 285-297.e285.

206. Pearson, J. A., D. Kakabadse, J. Davies, J. Peng, J. Warden-Smith, S. Cuff, M. Lewis, L. C. da Rosa, L. Wen, and F. S. Wong. 2019. Altered Gut Microbiota Activate and Expand Insulin B15-23-Reactive CD8+ T Cells. *Diabetes* 68: 1002-1013.

207. Tanoue, T., S. Morita, D. R. Plichta, A. N. Skelly, W. Suda, Y. Sugiura, S. Narushima, H. Vlamakis, I. Motoo, K. Sugita, A. Shiota, K. Takeshita, K. Yasuma-Mitobe, D. Riethmacher, T. Kaisho, J. M. Norman, D. Mucida, M. Suematsu, T. Yaguchi, V. Bucci, T. Inoue, Y. Kawakami, B. Olle, B. Roberts, M. Hattori, R. J. Xavier, K. Atarashi, and K. Honda. 2019. A defined commensal consortium elicits CD8 T cells and anti-cancer immunity. *Nature* 565: 600-605.

208. Gonzalez-Perez, G., A. L. Hicks, T. M. Tekieli, C. M. Radens, B. L. Williams, and E. S. Lamousé-Smith. 2016. Maternal Antibiotic Treatment Impacts Development of the Neonatal Intestinal Microbiome and Antiviral Immunity. *J Immunol* 196: 3768-3779.

209. Baazim, H., M. Schweiger, M. Moschinger, H. Xu, T. Scherer, A. Popa, S. Gallage, A. Ali, K. Khamina, L. Kosack, B. Vilagos, M. Smyth, A. Lercher, J. Friske, D. Merkler, A. Aderem, T. H. Helbich, M. Heikenwalder, P. A. Lang, R. Zechner, and A. Bergthaler. 2019. CD8(+) T cells induce cachexia during chronic viral infection. *Nat Immunol* 20: 701-710.

210. Hatter, J. A., Y. M. Kouche, S. J. Melchor, K. Ng, D. M. Bouley, J. C. Boothroyd, and S. E. Ewald. 2018. Toxoplasma gondii infection triggers chronic cachexia and sustained commensal dysbiosis in mice. *PLoS One* 13: e0204895.

211. Cumnock, K., A. S. Gupta, M. Lissner, V. Chevee, N. M. Davis, and D. S. Schneider. 2018. Host Energy Source Is Important for Disease Tolerance to Malaria. *Curr Biol* 28: 1635-1642 e1633.

212. Horne-Debets, J. M., R. Faleiro, D. S. Karunarathne, X. Q. Liu, K. E. Lineburg, C. M. Poh, G. M. Grotenbreg, G. R. Hill, K. P. MacDonald, M. F. Good, L. Renia, R. Ahmed, A. H. Sharpe, and M. N. Wykes. 2013. PD-1 dependent exhaustion of CD8+ T cells drives chronic malaria. *Cell Rep* 5: 1204-1213.

213. John, B., T. H. Harris, E. D. Tait, E. H. Wilson, B. Gregg, L. G. Ng, P. Mrass, D. S. Roos, F. Dzierszinski, W. Weninger, and C. A. Hunter. 2009. Dynamic Imaging of CD8(+) T

cells and dendritic cells during infection with Toxoplasma gondii. *PLoS Pathog* 5: e1000505.

214. Ruibal, P., L. Oestereich, A. Lüdtke, B. Becker-Ziaja, D. M. Wozniak, R. Kerber, M. Korva, M. Cabeza-Cabrerizo, J. A. Bore, F. R. Koundouno, S. Duraffour, R. Weller, A. Thorenz, E. Cimini, D. Viola, C. Agrati, J. Repits, B. Afrough, L. A. Cowley, D. Ngabo, J. Hinzmann, M. Mertens, I. Vitoriano, C. H. Logue, J. P. Boettcher, E. Pallasch, A. Sachse, A. Bah, K. Nitzsche, E. Kuisma, J. Michel, T. Holm, E. G. Zekeng, I. García-Dorival, R. Wölfel, K. Stoecker, E. Fleischmann, T. Strecker, A. Di Caro, T. Avšič-Županc, A. Kurth, S. Meschi, S. Mély, E. Newman, A. Bocquin, Z. Kis, A. Kelterbaum, P. Molkenthin, F. Carletti, J. Portmann, S. Wolff, C. Castilletti, G. Schudt, A. Fizet, L. J. Ottowell, E. Herker, T. Jacobs, B. Kretschmer, E. Severi, N. Ouedraogo, M. Lago, A. Negredo, L. Franco, P. Anda, S. Schmiedel, B. Kreuels, D. Wichmann, M. M. Addo, A. W. Lohse, H. De Clerck, C. Nanclares, S. Jonckheere, M. Van Herp, A. Sprecher, G. Xiaojiang, M. Carrington, O. Miranda, C. M. Castro, M. Gabriel, P. Drury, P. Formenty, B. Diallo, L. Koivogui, N. Magassouba, M. W. Carroll, S. Günther, and C. Muñoz-Fontela. 2016. Unique human immune signature of Ebola virus disease in Guinea. *Nature* 533: 100-104.

215. Bartley, J. M., X. Zhou, G. A. Kuchel, G. M. Weinstock, and L. Haynes. 2017. Impact of Age, Caloric Restriction, and Influenza Infection on Mouse Gut Microbiome: An Exploratory Study of the Role of Age-Related Microbiome Changes on Influenza Responses. *Front Immunol* 8: 1164.

216. Wang, A., S. C. Huen, H. H. Luan, S. Yu, C. Zhang, J. D. Gallezot, C. J. Booth, and R. Medzhitov. 2016. Opposing Effects of Fasting Metabolism on Tissue Tolerance in Bacterial and Viral Inflammation. *Cell* 166: 1512-1525.e1512.

217. Routy, B., E. Le Chatelier, L. Derosa, C. P. M. Duong, M. T. Alou, R. Daillère, A. Fluckiger, M. Messaoudene, C. Rauber, M. P. Roberti, M. Fidelle, C. Flament, V. Poirier-Colame, P. Opolon, C. Klein, K. Iribarren, L. Mondragón, N. Jacquelot, B. Qu, G. Ferrere, C. Clémenson, L. Mezquita, J. R. Masip, C. Naltet, S. Brosseau, C. Kaderbhai, C. Richard, H. Rizvi, F. Levenez, N. Galleron, B. Quinquis, N. Pons, B. Ryffel, V. Minard-Colin, P. Gonin, J. C. Soria, E. Deutsch, Y. Loriot, F. Ghiringhelli, G. Zalcman, F. Goldwasser, B. Escudier, M. D. Hellmann, A. Eggermont, D. Raoult, L. Albiges, G. Kroemer, and L. Zitvogel. 2018. Gut microbiome influences efficacy of PD-1-based immunotherapy against epithelial tumors. *Science* 359: 91-97.

218. Morin, M., E. C. Pierce, and R. J. Dutton. 2018. Changes in the genetic requirements for microbial interactions with increasing community complexity. *Elife* 7.

219. Ansaldo, E., L. C. Slayden, K. L. Ching, M. A. Koch, N. K. Wolf, D. R. Plichta, E. M. Brown, D. B. Graham, R. J. Xavier, J. J. Moon, and G. M. Barton. 2019. Akkermansia muciniphila induces intestinal adaptive immune responses during homeostasis. *Science* 364: 1179-1184.

220. Depommier, C., A. Everard, C. Druart, H. Plovier, M. Van Hul, S. Vieira-Silva, G. Falony, J. Raes, D. Maiter, N. M. Delzenne, M. de Barsy, A. Loumaye, M. P. Hermans, J. P. Thissen, W. M. de Vos, and P. D. Cani. 2019. Supplementation with Akkermansia muciniphila in overweight and obese human volunteers: a proof-of-concept exploratory study. *Nat Med*.

221. Greer, R. L., X. Dong, A. C. Moraes, R. A. Zielke, G. R. Fernandes, E. Peremyslova, S. Vasquez-Perez, A. A. Schoenborn, E. P. Gomes, A. C. Pereira, S. R. Ferreira, M. Yao, I. J. Fuss, W. Strober, A. E. Sikora, G. A. Taylor, A. S. Gulati, A. Morgun, and N. Shulzhenko. 2016. Akkermansia muciniphila mediates negative effects of IFNγ on glucose metabolism. *Nat Commun* 7: 13329.

222. Krautkramer, K. A., J. H. Kreznar, K. A. Romano, E. I. Vivas, G. A. Barrett-Wilt, M. E. Rabaglia, M. P. Keller, A. D. Attie, F. E. Rey, and J. M. Denu. 2016. Diet-Microbiota Interactions Mediate Global Epigenetic Programming in Multiple Host Tissues. *Mol Cell* 64: 982-992.

223. Li, J., S. Lin, P. M. Vanhoutte, C. W. Woo, and A. Xu. 2016. Akkermansia Muciniphila Protects Against Atherosclerosis by Preventing Metabolic Endotoxemia-Induced Inflammation in Apoe-/- Mice. *Circulation* 133: 2434-2446.

224. Wu, W., L. Lv, D. Shi, J. Ye, D. Fang, F. Guo, Y. Li, X. He, and L. Li. 2017. Protective Effect of Akkermansia muciniphila against Immune-Mediated Liver Injury in a Mouse Model. *Front Microbiol* 8: 1804.

225. Blacher, E., S. Bashiardes, H. Shapiro, D. Rothschild, U. Mor, M. Dori-Bachash, C. Kleimeyer, C. Moresi, Y. Harnik, M. Zur, M. Zabari, R. B. Brik, D. Kviatcovsky, N. Zmora, Y. Cohen, N. Bar, I. Levi, N. Amar, T. Mehlman, A. Brandis, I. Biton, Y. Kuperman, M. Tsoory, L. Alfahel, A. Harmelin, M. Schwartz, A. Israelson, L. Arike, M. E. V. Johansson, G. C. Hansson, M. Gotkine, E. Segal, and E. Elinav. 2019. Potential roles of gut microbiome and metabolites in modulating ALS in mice. *Nature* 572: 474-480.

226. The Lancet Gastroenterology, H. 2019. Probiotics: elixir or empty promise? *Lancet Gastroenterol Hepatol* 4: 81.

227. Thompson, L. R., J. G. Sanders, D. McDonald, A. Amir, J. Ladau, K. J. Locey, R. J. Prill, A. Tripathi, S. M. Gibbons, G. Ackermann, J. A. Navas-Molina, S. Janssen, E. Kopylova, Y. Vázquez-Baeza, A. González, J. T. Morton, S. Mirarab, Z. Zech Xu, L. Jiang, M. F. Haroon, J. Kanbar, Q. Zhu, S. Jin Song, T. Kosciolek, N. A. Bokulich, J. Lefler, C. J. Brislawn, G. Humphrey, S. M. Owens, J. Hampton-Marcell, D. Berg-Lyons, V. McKenzie, N. Fierer, J. A. Fuhrman, A. Clauset, R. L. Stevens, A. Shade, K. S. Pollard, K. D. Goodwin, J. K. Jansson, J. A. Gilbert, R. Knight, and E. M. P. Consortium. 2017. A communal catalogue reveals Earth's multiscale microbial diversity. *Nature* 551: 457-463.

228. Swidsinski, A., B. C. Sydora, Y. Doerffel, V. Loening-Baucke, M. Vaneechoutte, M. Lupicki, J. Scholze, H. Lochs, and L. A. Dieleman. 2007. Viscosity gradient within the

mucus layer determines the mucosal barrier function and the spatial organization of the intestinal microbiota. *Inflamm Bowel Dis* 13: 963-970.

229. Derrien, M., M. C. Collado, K. Ben-Amor, S. Salminen, and W. M. de Vos. 2008. The Mucin degrader Akkermansia muciniphila is an abundant resident of the human intestinal tract. *Appl Environ Microbiol* 74: 1646-1648.